UMinho | 2021

Bruna Ferreira Gonçalves **Novel printable photovoltaic systems based on Cu(In,Ga)Se_2 chalcopyrite**

Universidade do Minho
Escola de Engenharia

Bruna Ferreira Gonçalves

Novel printable photovoltaic systems based on Cu(In,Ga)Se_2 chalcopyrite

julho de 2021

Universidade do Minho
Escola de Engenharia

Bruna Ferreira Gonçalves

Novel printable photovoltaic systems based on Cu(In,Ga)Se_2 chalcopyrite

Tese de Doutoramento
Programa Doutoral em Engenharia de Materiais

Trabalho efetuado sob a orientação do
Professor Senentxu Lanceros-Mendez
do
Doutor Yury Kolen'ko
e da
Professora Gabriela Botelho

julho de 2021

DIREITOS DE AUTOR E CONDIÇÕES DE UTILIZAÇÃO DO TRABALHO POR TERCEIROS

Licença concedida aos utilizadores deste trabalho

ACKNOWLEDGEMENTS

This thesis becomes a reality with the kind support and help of many individuals to whom I would like to extend my deep gratitude.

I would also like to thank the Portuguese Foundation of Science and Technology for turning this project possible with the financial support given, grant no. SFRHBD/121780/2016.

It is a genuine pleasure to express my deepest thanks and sincere appreciation to my supervisors Senentxu Lanceros-Méndez, Yury Kolen'ko, and Gabriela Botelho for the wisdom, strength, sympathy, empathy, and motivation provided over the years, essential to complete this journey.

To all my colleagues from Nanochemistry and Electroactive Smart Materials research groups for the great team spirit, companionship, and encouragement to always keep pushing. A special acknowledgement to Juliana Sousa, Orlando Oliveira, Miguel Franco, Yasmine Ziouani, Tiago Marinho, Daniela Correia, Catarina Lima and Sylvie Ribeiro for the help, effort, and support on the lab, and the friendship they devoted to me during the work.

I would also like to thank all my friends and volleyball teammates for their encouragement and moral support. The deepest sense of gratitude to my dear Hugo Salazar for all the love, joy, and support, and for always believing and pushing me to move forward.

Finally, and more importantly, I am extremely grateful to my brother for the pep talks, encouragement, guidance, and support gave and to my parents for their love, prayers, caring, and sacrifices made for educating and preparing me for the future.

Thank you all for being part of this journey!

STATEMENT OF INTEGRITY

I hereby declare having conducted this academic work with integrity. I confirm that I have not used plagiarism or any form of undue use of information or falsification of results along the process leading to its elaboration.

I further declare that I have fully acknowledged the Code of Ethical Conduct of the University of Minho.

Novos sistemas fotovoltaicos impressos com base na calcopirita $Cu(In,Ga)Se_2$

Nas últimas décadas temos assistido a uma intensa procura de fontes de energia eficientes, limpas e renováveis para responder ao crescente consumo energético e aos objetivos de descarbonização. No âmbito da energia solar, as células solares de filme fino inorgânico com base em $CuIn_xGa_{1-x}Se_2$ (CIGSe), merecem especial atenção. No entanto, os sistemas fotovoltaicos (FV) com maior eficiência utilizam processos de deposição a vácuo que requerem equipamentos sofisticados e elevadas quantidades de energia. A deposição sem vácuo, por outro lado, permite a produção industrial de dispositivos FVs de baixo custo, leves e flexíveis, e com um menor impacto ambiental. Assim, este trabalho utiliza processos de produção de sistemas FV CIGSe através da impressão de filmes finos de CIGSe por serigrafia, utilizando tintas contendo precursores/nanopartículas (NPs) bem dispersos. Para este fim, duas metodologias foram utilizadas: uma convencional e uma alternativa ecológica à anterior, com base na utilização de água como solvente. Em relação à origem dos precursores, duas rotas foram utilizadas: filmes impressos contendo óxidos comerciais de Cu, In e Ga, seguidos de selenização para converter os percursores em CIGSe e filmes contendo NPs de CIGSe que não requerem selenização.

Notavelmente, a síntese conduzida com metodologias convencionais originou uma grande quantidade de NPs CIGSe de fase pura de wurzita com estrutura hexagonal. A resultante camada fotoabsorvente impressa exibiu uma espessura homogénea de 4,5 μm com fase calcopirita. Em relação aos percursores comerciais, foi produzida uma célula FV CIGSe através da impressão de tintas contento óxidos de Cu, In e Ga dispersos em terpineol, seguida de selenização. A deposição das camadas superiores de CdS, através de banho químico, e i-ZnO/ZnO:Al através de pulverização catódica, resultou num dispositivo FV com 6,1% de eficiência. Por outro lado, o uso de metodologias ecológicas resultou na primeira síntese aquosa de grande quantidade de NPs CIGSe de fase pura de calcopirita com estrutura tetragonal. Além disso, a formulação de tintas aquosas com óxidos bem dispersos e posterior selenização foi realizada para produzir células FV mais sustentáveis. Seguindo os processos acima descritos foi produzida uma célula FV CIGSe com recorde de eficiência de 7.9%. Finalmente, a deposição por spray de tintas condutoras aquosas resultou numa célula FV CIGSe totalmente produzida sem vácuo com eficiência de 2,2%, um recorde para tais sistemas sustentáveis.

Assim, o presente trabalho fornece alternativas sustentáveis para a fabricação de células FV CIGSe com base em deposições sem vácuo que são compatíveis com a produção industrial de sistemas FV, permitindo assim uma produção com maior relação custo-eficiência.

Palavras-chave: CIGSe, impressão funcional, serigrafia, sistemas fotovoltaicos, sustentabilidade.

Novel printable photovoltaic systems based on $Cu(In,Ga)Se_2$ chalcopyrite

Over the last decades, strong efforts are being carried out looking for efficient, clean and renewable energy sources to fulfill the ever-growing energy consumption and meet the decarbonization goals. With respect to solar energy, inorganic thin film solar cells based on $\mathrm{CuIn_xGa_{1-x}Se_2}$ (CIGSe) deserve special attention. However, most efficient CIGSe photovoltaic (PV) systems reported to date comprise complex equipment and high energy-demanding vacuum deposition processes. Non-vacuum deposition processes, on the other hand, allows for a low cost industrial roll-to-roll production of light weight and flexible CIGSe PVs with low environmental impact. Thus, the herein presented work addresses the processing of CIGSe PV systems by screen printing photoabsorber CIGSe thin films, using inks comprising well-dispersed CIGSe precursors/nanoparticles (NPs). To this end, two different methodologies were used: a conventional one and an environmentally friendly alternative, based on the use of water as solvent. Regarding the nature of the inks' precursors, two distinct routes were followed: Cu, In and Ga commercial oxides printed films followed by selenization to convert the precursors into the desired CIGSe phase; and films with synthesized CIGSe NPs, which does not requires a selenization treatment.

Notably, the synthesis conducted with conventional methodologies gave rise to large amount of phase-pure CIGSe NPs with hexagonal wurtzite structure. Then, the resultant screen-printed photoabsorber displayed a homogeneous thickness of ≈4.5 μm with chalcopyrite phase. Concerning the commercial precursors, a CIGSe PV cell was produced by screen printing Cu, In and Ga oxides ink in terpineol solvent followed by selenization. The consecutive chemical bath deposition of CdS buffer layer and sputtering of top i-ZnO and ZnO:Al layers, resulted in a PV device with 6.1% of efficiency. The use of environmentally friendly methodologies, on the other hand, delivered for the first time a large amount of aqueously synthesized phase-pure CIGSe NPs with tetragonal chalcopyrite structure. Moreover, the formulation of water-based inks with well-dispersed oxides and further selenization was conducted to produce more sustainable PV cells. Following the same processes to complete the device, a record-breaking CIGSe PV cell with 7.9% of efficiency was produced. Finally, the replacement of sputtering of top conductive layers by spray coating of water-based conductive inks resulted in a sustainable all-non-vacuum processed CIGSe PV cell with 2.2% of efficiency, a record breaking for such sustainable systems.

Thus, the present work provides sustainable alternatives to vacuum-based fabrication of CIGSe PV cells which are compatible with roll-to-roll production of PV systems, allowing for more cost-efficient production in future.

Keywords: CIGSe, functional printing, photovoltaic systems, screen printing, sustainability.

Table of contents

List of figures

List of tables

List of symbols

€	Euro
Ch	α-CIGSe phase
$E_{bulk/slab}$	Total energy of a periodic unit of a bulk system or a surface slab
E_C	Conduction band energy
E_F	Fermi energy
E_g	Band gap
E_V	Valence band energy
FF	Fill factor
I_{MP}	Current at maximum power
I_{SC}	Short-circuit current
I-V	Current-voltage
J_{sc}	Short-circuit current density
J–V	Current density-voltage
P1	β-CIGSe phase
P_{in}	Input power
P_{max}	Maximum output power
P_{out}	Output power
R_S	Series resistance
R_{SH}	Shunt resistance
T	Temperature
T_{550nm}	Transmittance at 550 nm
V_{MP}	Voltage at maximum power
V_{OC}	Open-circuit voltage
Zb	δ-CIGSe phase
α-CISe	CISe with tetragonal chalcopyrite structure
β-CISe	CISe with tetragonal stannite structure
γ-CISe	CISe with hexagonal layered structure
δ-CISe	CISe with cubic sphalerite structure
ΔE_{passiv}	Passivation energy
ΔE_{seg}	Segregation energy

Φ_B	Barrier height

List of abbreviations

A

ACN	Acetonitrile
AM1.5G	Air mass 1.5 global
AZO	ZnO:Al

B

BYK180	Disperbyk-180
BYK199	Disperbyk-199
BYK2013	Disperbyk-2013
BYK7420 ES	Rheobyk-7420 ES

C

CBD	Chemical bath deposition
CIGSe	Copper indium gallium diselenide
CISe	Copper indium diselenide
CTAB	Hexadecyltrimethylammonium bromide

D

DCM	Dichloromethane
DFT	Density functional theory
DPM	Di(propylene glycol) methyl ether
DSA–CA	Drop-shape analysis–contact angle

E

EC	Ethyl cellulose
EDA	Ethylenediamine
EDX	Energy-dispersive X-ray

F

FIB	Focused ion beam
FFT	Fast Fourier transformer
FTO	Fluorine-doped tin oxide
FTO/SLG	FTO coated SLG substrate
FWHM	Full width at half maximum

G

GSH	L-glutathione reduced

H

HAADF	High-angle annular dark-field
HDA	Hexadecylamine
HPMC	Hydroxypropyl methyl cellulose
HRTEM	High-resolution transmission electron microcopy

I

ICDD	International Centre for Diffraction Data
IPA	Isopropanol
ITO	Tin-doped indium oxide

M

MEMS	Microelectromechanical systems
Mo/SLG	Mo-coated SLG
MQ	Milli-Q water

N

NP	Nanoparticle
NREL	National Renewable Energy Laboratory
NW	Nanowire

O

OA	Oleic acid
OM	Optical microscopy

P

PCE	Power conversion efficiency
PV	Photovoltaic
PVA	Polyvinyl alcohol polymer

Q

QNR	Quasi-neutral region

R

RT	Room temperature
RTA	Rapid thermal annealing

S

SAED	Selected area electron diffraction
SCR	Space charge region
SEM	Scanning electron microscopy

SLG	Soda-lime glass
STEM	Scanning transmission electron microscopy

T

TACT	Tetrakis(acetonitrile)copper(I) tetrafluoroborate
TCO	Transparent conductive oxide
TEM	Transmission electron microscopy
TGA	Thermogravimetric analysis
Tiron	4,5-dihydroxy-1,3-benzenedisulfonic acid disodium salt monohydrate
Tween 60	Polyethylene glycol sorbitan monostearate

W

WBM	Wet ball milling

X

XRD	X-ray diffraction

“*Science is not only a discipline of reason but also one of romance and passion.*”

Stephen Hawking

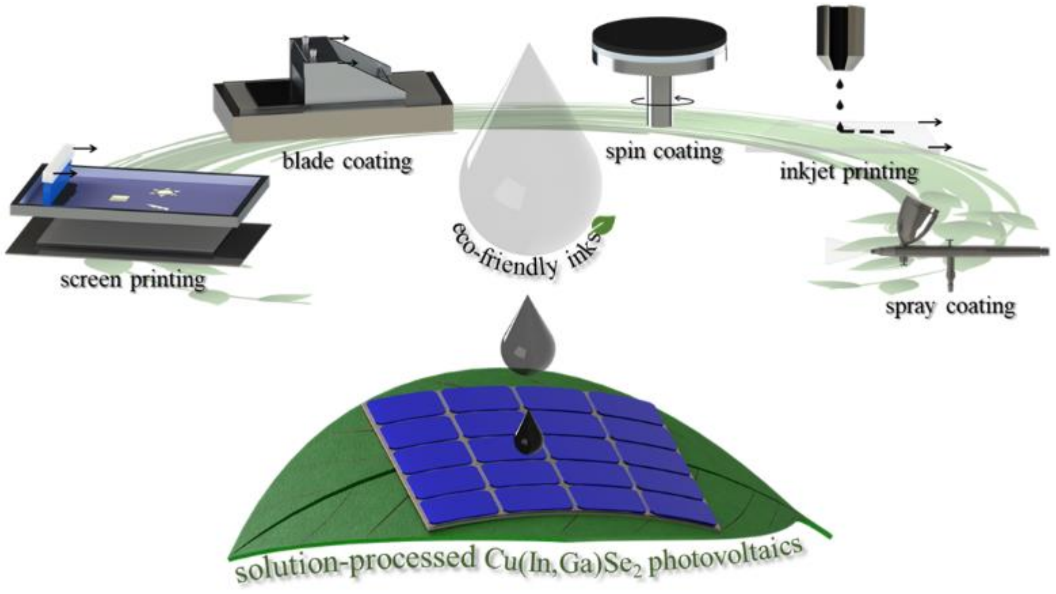

Chapter 1. Introduction

The targeted global decarbonization demands the urgent replacement of conventional fossil fuel based process for low carbon technologies. For instance, the energy from the sun is abundant, inexhaustible, non-polluting, and low-priced, however, to produce energy in large scale with reliable, cost-efficient and environmentally friendly methods, is a challenge. The outstanding optical properties of $\mathrm{Cu(In,Ga)Se_2}$ thin film photovoltaics and intrinsic compatibility with industrial-scale production are paving a way towards this technology. This chapter reviews printing/coating cost-efficient and sustainable fabrication methodologies for the replacement of current high energy-demanding vacuum-based fabrication of $\mathrm{Cu(In,Ga)Se_2}$ photovoltaics. As final goal, all-printed/solution-processed $\mathrm{Cu(In,Ga)Se_2}$ photovoltaics are addressed, towards an environmental friendlier, higher throughput and low-cost production of photovoltaics.

This chapter is based on the following publication: **B. F. Gonçalves**, S. Sadewasser, S. Lanceros-Méndez and Y. V. Kolen'ko, *Merging Solution Processing and Printing for Sustainable Fabrication of Cu(In,Ga)Se$_2$ Photovoltaics*; Submitted 2021.

1.1 Solar energy

Over the last decades, climate change has become one of the major societal concerns. This problem is somehow related to human behavior and is already affecting many regions around the world, mostly by the presence of air pollution, extreme weather conditions, and rising sea levels. Scientists have been studying this phenomenon and CO_2 emissions are reported as one of the major contributors [1]. Interestingly, the technological growth has increased the energy consumption at a rate never seen before and by 2050 is predicted that the energy consumption will more than double the nowadays needs [2].

The Paris agreement established a limit of the global temperature rise to ideally 1.5 ^{o}C. To accomplish it, the world needs a reduction of CO_2 emissions until 2050 by 3.5% per year. More recently, the European Commission set out the “European Green Deal”, establishing a new growth strategy, to turn Europe a climate-neutral continent, with 50% less greenhouse gases emissions in 2030 and no net emission in 2050 [3]. To meet these targets, the deployment of low carbon technologies to replace conventional fossil fuel usage is urgent [1]. Notably, the energy from the sun has great potential to support this transition as in just one hour it supplies an amount of energy almost equivalent to the annual energy consumption on our planet [4]. Furthermore, is abundant, inexhaustible, non-polluting, and free, however, to produce energy in the TW scale with reliable and cost-efficient methods, is a challenge (Figure 1.1).

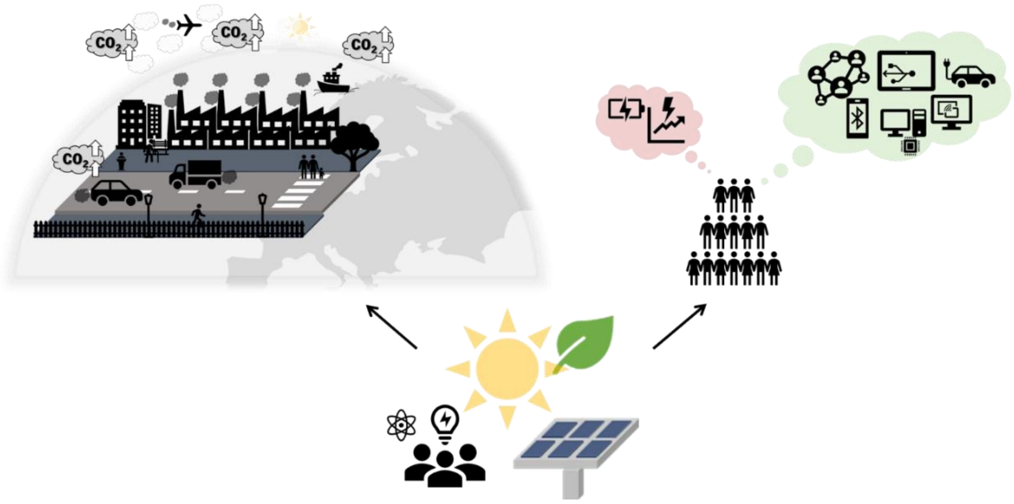

Figure 1.1. Solar energy as a solution to decrease CO_2 emissions and to contribute to a higher energetic demand.

From all the radiation emitted by the sun, less than 50% reaches the surface of our planet, the rest is absorbed, filtered, reflected and scattered by the atmosphere [5]. With only some radiation reaching the earth's surface and without a permanent presence of the sun, researchers are working to improve the devices, reaching some important milestones and bringing solar energy to a leading path.

Importantly, in 2018 (Figure 1.2a), from all of the electricity produced in the world, 25% was generated by renewable sources with solar energy representing only 2% [6]. The projections for 2050 (Figure 1.2b) consider that the contribution of this energy into the global electricity production will increase from 2 to 25% and the non-renewables will decrease to 14% [2]. Moreover, the investment on solar energy is highly increasing and therefore contributing to lower its costs. In 2010 (Figure 1.2c) it costed 325 € per MWh and in 2019 reduced 87% to 46 € per MWh. By 2030 the estimated cost is between 30 and 35 € per MWh [7]. Regarding the 2018 ranking of global electricity production from photovoltaic (PV) systems (Figure 1.2d), China is leading it with 178 TWh. Germany, on the other hand, is the leading country in Europe with 46 TWh and Portugal occupies the 15th place in Europe and 34th in the world, with ≈1 TWh of electricity production [6].

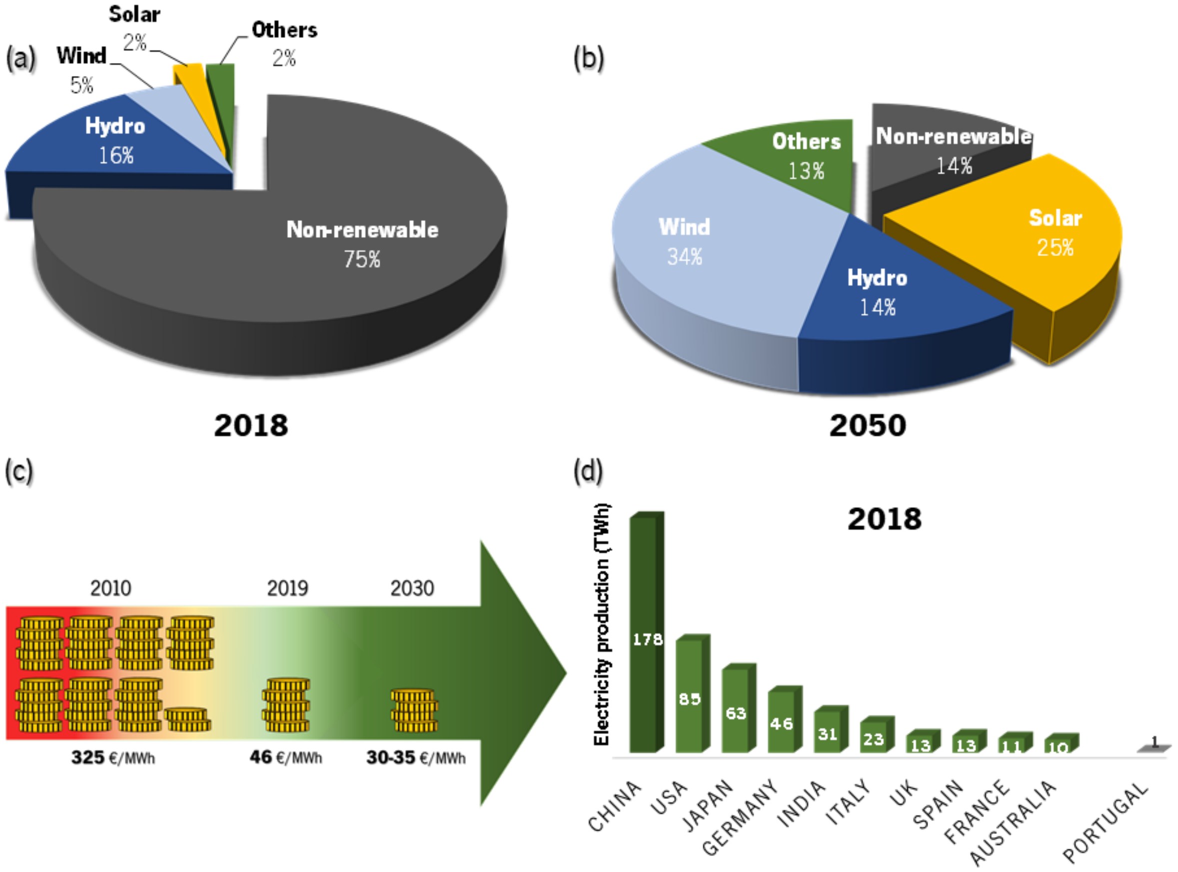

Figure 1.2. Global electricity production from different sources in 2018 (a) and predictions for 2050 (b); Cost of solar PV systems per MWh from 2010 to 2019 and predictions for 2030 (c); 2018 top 10 countries with higher electricity production from PV systems and Portugal position (d). Data source: [2, 6, 7].

1.2 Photovoltaic systems

Solar energy can be directly harvested using small PV cells which in the presence of sunlight convert part of the sun energy into electrical energy, without creating any kind of pollution. A PV cell is a non-linear system that can produce a specific amount of electric power, depending not only on the efficiency of the device but also on the solar irradiation and ambient temperature, among other factors [8]. In order to produce more energy, PV cells can be connected in series and in parallel combinations to form modules. When connecting modules, PV arrays arise providing power in the range of MW [8].

1.2.1 Photovoltaic effect

The conversion of sunlight into electrical power occurs due to a physical principle first observed in 1839 by Alexandre-Edmond Becquerel, namely the photovoltaic effect, which is similar to photoelectric effect, explained by Einstein in 1905. Once PV effect was acknowledged, materials were studied and developed to optimize the electrical response. The first commercial PV cell was built in 1954 by Bell Laboratories, showing 6% of efficiency and using Silicon semiconductor material [9].

This principle is described by the generation of a potential difference at the junction of at least two different semiconductor materials in response to electromagnetic radiation [8]. To observe it, two semiconductors with extra opposite charges must be in contact, one negatively charged (*n*–type) where it is favored the movement of electrons and one positively charged (*p*–type) where it is favored the movement of holes. Once in contact, a *p*–*n* junction is created and due to the presence of a gradient of charges, these will diffuse between the two materials to recombine to each other and reach an equilibrium (Figure 1.3a). In equilibrium, an electric field will separate both materials, namely depletion zone, working as barrier, and no charges from either side crosses. When electrodes are connected on both semiconductors, the charges will be collected (Figure 1.3b) [5].

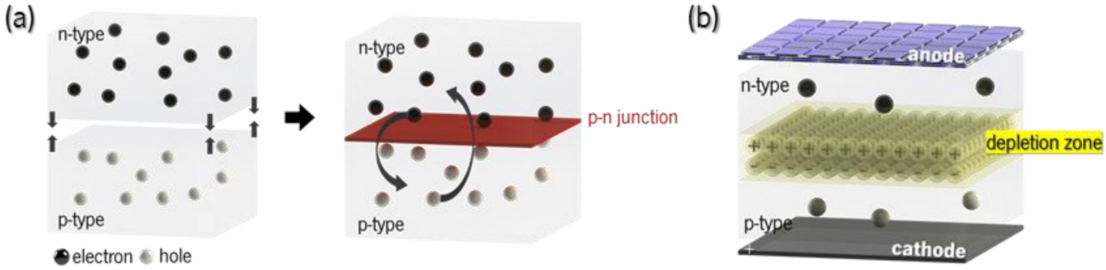

Figure 1.3. Photovoltaic effect: *p*–*n* junction (a) and depletion zone (b).

Once a photon is absorbed by the PV cell, if it has an energy equal or higher than the band gap (E_g) energy of the semiconductor, an electron will be excited from its valence band to the conduction band, leaving a hole on the first, and creating an electron-hole pair (Figure 1.4a) [5]. Due to the presence of a depletion zone, the electron-hole pairs are conducted to their respective semiconductor and electrodes (Figure 1.4b). Once the electrodes are connected to an external circuit, the electrons will move through this circuit (Figure 1.4c) to further recombine with the holes and finally generating electrical power (Figure 1.4d) [5].

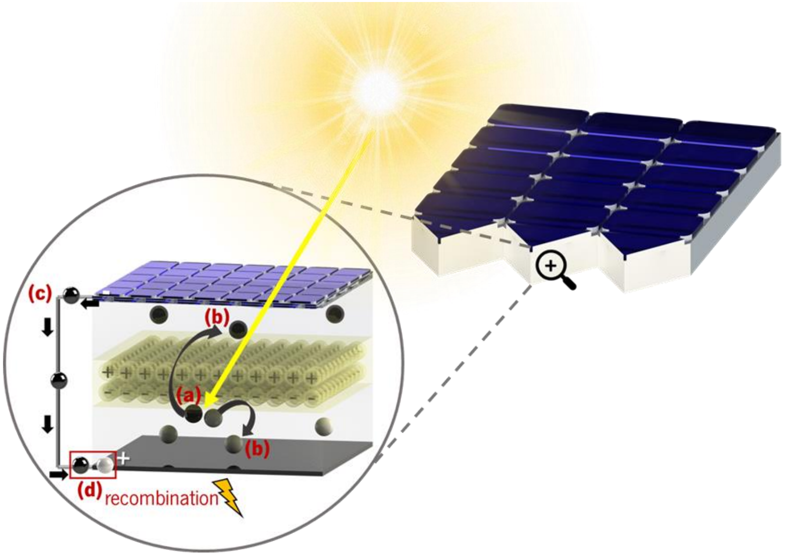

Figure 1.4. PV system when exposed to sunlight: generation of an electron-hole pair (a); separation of the electron-hole pairs to their respective electrodes (b); electron movement trough the external circuit from anode to cathode (c); recombination of electron with holes and generation of energy (d).

1.2.2 Photovoltaic evaluation parameters

A PV cell performance is evaluated by how well it operates under sunlight. In industry, a standard, AM1.5G (air mass 1.5 global), is used to evaluate the performance, meaning the average global solar spectrum after passing through 1.5 atmospheres, which is more representative of the average solar irradiation at earth's mid-latitudes [10]. The conversion of photons into electric power is the key ability of a PV cell and is quantifiable by a parameter known as power conversion efficiency (PCE) where the ratio of incident light to electrical power output is measured. To evaluate this parameter, current-voltage (*I-V*) measurements are conducted, where a series of voltages are applied to the PV cell while is under illumination [10]. At each voltage step, the output current is measured resulting in an *I-V* curve with the following characteristic behavior (Figure 1.5).

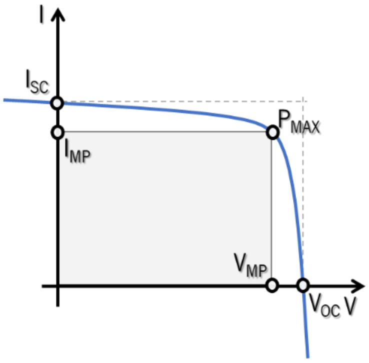

Figure 1.5. Typical *I-V* curve of a PV cell with evaluation parameters identified.

Importantly, different parameters can be acquired by this curve [10]:

- **Maximum output power (P_{max}):** where PV cell should operate to give the maximum power output.
- **Current at maximum power (I_{MP}):** current at maximum power.
- **Voltage at maximum power (V_{MP}):** voltage at maximum power.
- **Short-circuit current (I_{SC}):** maximum current through the PV cell when the voltage across the device is zero. It depends on the cell's area, the absorption capacity of the photoabsorber layer and the separation, transportation and extraction of the generated charges.
- **Open-circuit voltage (V_{OC}):** maximum voltage of a PV cell when the applied electric field cancels the built-in electric field and therefore the current through the device is zero. It depends on the energy levels of the photoabsorber material, the work functions of the electrode materials and the charge carrier recombination rate.

From the above-mentioned parameters, the PV cell's fill factor (FF) and PCE are determined. FF is the ratio of the actual power of the cell to the ideal power if there were no series resistance (R_S) and infinite shunt resistance (R_{SH}). It evaluates the recombination losses within the PV cell and is determined by the following (Equation 1.1) [10, 11]. Importantly, the closest to 1 the better is the performance of the device.

$$FF = \frac{I_{MP} \times V_{MP}}{I_{SC} \times V_{OC}} \tag{1.1}$$

R_S and R_{SH} are parasitic elements, which represents losses in the PV cell. Both degrades the PV cell's FF and PCE however do not produce impact on the I_{SC} or V_{OC} [10, 11]. The element R_S is related to resistances that arise from energetic barriers at layer's interfaces and bulk resistances within layers. This comprises the current movement through the PV cell's semiconductors, the contact resistance between the electrodes and the semiconductors, and the resistance of top and back electrodes. To avoid this element, there should exist a correct energy level alignment of the materials used on the device [11]. On the other hand, R_{SH} is related to the existence of alternate current pathways through the PV cell. Low R_{SH} causes power losses in PV cells by providing an alternative current path for the photogenerated current. In opposition to R_S, this element is desirable to be as high as possible to prevent current leakage trough these alternative paths. Usually this element is associated to manufacturing defects [11]. The PCE of a PV cell is the ratio of output power (P_{out}) to input power (P_{in}), (Equation 1.2) [10, 11].

$$PCE = \frac{P_{out}}{P_{in}} = \frac{I_{SC} \times V_{OC}}{P_{in}} \tag{1.2}$$

Where, P_{in} is determined by the product of the light intensity input and the PV cell's surface area [11].

1.2.3 Photovoltaic systems development history

Over the past decades, PVs have been widely studied, leading to improvements on photoabsorber materials and PV engineering, which have been resulting in devices with higher efficiency (Figure 1.6).

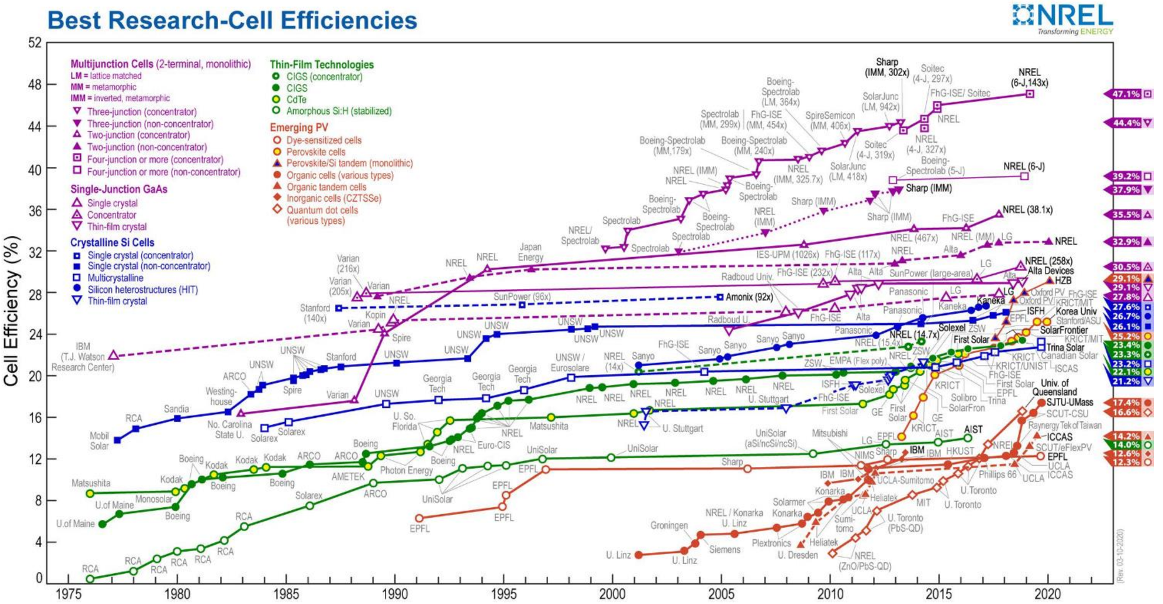

Figure 1.6. PV cell's efficiencies trough time using different technologies [12].

PV cells are classified as single-junction, when it uses a single *p–n* junction, or as multi-junction, when it uses multiple physical configurations to take advantage of several mechanisms of absorption and charge separation. The junction can be either, built with the same semiconductor material but with different doping (homo-junction) or by different materials with different band gaps (hetero-junction).

Currently, PV cells are classified into four generations, depending on time and materials used for their fabrication [13, 14]. First-generation PVs are based on silicon, and it is the most mature and commercialized technology. Second-generation comprises direct band gap photoabsorbers with a few micrometers of thickness. Third-generation uses organic semiconductors relying on several energy levels and multiple charge carrier generation. Finally, the emerging fourth-generation combines flexible polymeric thin films with nanoparticle structures to produce thin multi-spectrum layers (tandem PVs) [15]. Next, the top five PV cell technologies with the highest efficiencies to date with their respective advantages and limitations are addressed (Table 1.1).

Table 1.1. Five most efficient PV cells and their respective advantages and limitations.

PV technology	Advantages	Limitations	ECE (%)	Ref.
Multi-junction 3rd generation	- Most efficient technology.	- Very complex production process. - Most expensive technology.	47.1	[16, 17]
GaAs 1st generation	- High absorptivity. - Direct band gap. - Design versatility. - High thermal stability.	- High cost. - Complex production process.	29.3	[17]
Mono-crystalline Si 1st generation	- Long lifetime.	- Complex and high-cost production process. - High weight, rigid and large size.	27.6	[18]
Perovskite 3rd generation	- Low production cost. - Ultra-thin. - Flexibility. - High absorption coefficient. - Low cost and abundant materials.	- Short lifetime. - Low stability to environmental conditions. - Mechanical fragility.	25.2	[17, 19]
$\mathbf{Cu(In,Ga)Se_2}$ 2nd generation	- Low production cost. - Flexibility. - High absorption coefficient. - Tunable and direct band gap. - Long lifetime. - High thermal resistance.	- Indium scarcity.	23.4	[20]

The material to be used as a semiconductor should absorb the maximum of the sun's spectrum, meaning that a low band gap material is desirable, however, is necessary to produce high potential, which implies a high band gap. Nevertheless, if the band gap is too high, the photons with less energy will dissipate in the form of heat. Over the years, it has been stablished that a photoabsorber material should present the following characteristics to deliver ideal PV cells [21]:

- Semiconductor with a direct band gap structure.
- Semiconductor with a band gap between 1.1-1.7 eV.
- Nontoxic and readily available materials.
- Facile, inexpensive and reproducible deposition processes adequate for roll-to-roll industry.
- Great ECE.
- Long-term stability.

1.3 CIGSe photovoltaic systems

Since seminal reports of solar cells with $\mathrm{Cu(In,Ga)Se_2}$ (CIGSe) photoabsorber [22], extensive investigations of the material, PV cell design, and optimization studies have resulted in an interesting class of second-generation thin film PVs [23]. Importantly, CIGSe is a semiconductor with a high absorption coefficient ($\approx 10^5\ \mathrm{cm^{-1}}$) and a direct band gap that can be tuned from 1.0 to 1.7 eV by changing the chemical composition. For instance, $\mathrm{Cu(In_{1-x}Ga_x)Se_2}$ with $\mathrm{x} = 0$ exhibits a band gap of 1.0 eV, while when $\mathrm{x} = 1$, the band gap increases to 1.7 eV. The optoelectronic characteristics give access to CIGSe PVs with photoabsorber layers as thin as 1–2 μm, rendering the resultant thin film CIGSe PVs an appealing alternative to traditional first-generation silicon solar cells, which typically feature thicknesses of about 100 μm [24]. Notably, already 1% (1284 MW) of entire solar energy is produced by CIGSe PV technology [25].

1.3.1 CIGSe crystal

CIGSe is a chalcopyrite material composed by elements from groups I (Cu) and III (In, Ga) in equal parts and two parts of group VI element (Se). This crystal is classified as an alloy and a quaternary compound [26]. Since In and Ga are chemically very similar, the replacement of In by Ga does not produce drastic effects on the material chemistry. Therefore, the basis for CIGSe system is the $\mathrm{CuInSe_2}$ (CISe) system, which crystallizes in five different phases [27, 28]:

- $\mathrm{CuInSe_2}$ with tetragonal chalcopyrite structure **(α-CISe phase)**;
- $\mathrm{CuIn_2Se_{3.5}}$ and $\mathrm{CuIn_3Se_5}$ with tetragonal stannite structure **(β-CISe phase)**;
- $\mathrm{CuIn_5Se_8}$ with hexagonal layered structure **(γ-CISe phase)**;
- $\mathrm{CuInSe_2}$ with cubic sphalerite structure **(δ-CISe phase);**
- $\mathrm{CuInSe_2}$ with hexagonal wurtzite structure (recently discovered phase).

Interestingly, the unit cell of α-CISe chalcopyrite crystal structure can be deduced by doubling the unit cell of cubic sphalerite (zincblende), where each atom of Zn is bonded to four atoms of Se (Figure 1.7a). In contrast to zincblende, the bonds between Cu and Se in α-CISe, result from a p-d hybridization of the orbitals, which results in a different bond length within the structure, causing the tetragonal distortion of the α-CISe crystal structure (Figure 1.7b) [27]. A partial replacement of In by Ga in the α-CISe chalcopyrite unit cell, results in CIGSe chalcopyrite alloy unit cell (Figure 1.7c). CIGSe predominant phase fields can be deduced by the pseudo-ternary composition diagram of $\mathrm{Cu_2Se}$, $\mathrm{In_2Se_3}$, and $\mathrm{Ga_2Se_3}$ compounds, at room temperature (RT) (Figure 1.7d). From the predominance diagram, it is clear the presence of a α-CIGSe single phase, which broadens by increasing the [Ga]/[In] ratio towards Cu-poor compositions. It is also detectable a dominant phase on the diagram, namely "Ch + P1 + Zb", which means α-CIGSe + β-CIGSe + δ-CIGSe phases. Importantly, on this region there is a narrowest portion for [Ga]/[In+Ga] = 0.25 nominal ratio and Cu-poor stoichiometry, which is where CIGSe PV cells present higher efficiencies [26].

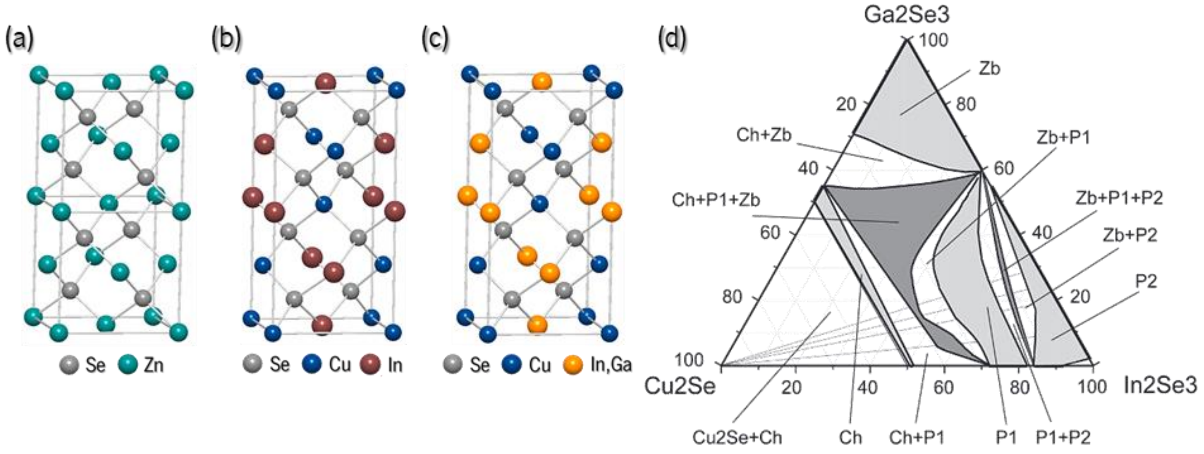

Figure 1.7. Unit cells of chalcogenide compounds: zincblende ZnSe (a), chalcopyrite CISe (b) and chalcopyrite CIGSe alloy (c). Predominance diagram of CIGSe alloy pseudo-ternary composition at RT (d). $Ch = \alpha - CIGSe\ phase,\ P1 = \beta - CIGSe\ phase,\ P2 = \gamma - CIGSe\ phase$ and $Zb = \delta - CIGSe\ phase$ [26].

1.3.2 Theoretical efficiency

A PV cell cannot convert 100 % of the light coming from the sun. Theoretically, for a non-concentrated system under AM1.5G illumination, the Shockley and Queisser limit determines that the maximum solar conversion efficiency for a single *p–n* junction CIGSe PV cell is ≈33.7%, which happens at a band gap of 1.34 eV [29]. This theoretical limit considers (i) non-absorbed photons below the photoabsorber band gap, (ii) thermalized energy of photons above the photoabsorber band gap, (iii) voltage loss from thermal radiation, and (iv) absence of ohmic-losses of the PV cells [30]. At the same time, the champion CIGSe PVs have experimentally reached efficiencies of 23.35% [20] and 18.6% [31] on the cell and module levels, respectively.

The inevitable recombination of charge carriers within a PV cell is critical for its performance. The recombination happens when an electron meets a hole, which decreases the amount of charge carriers and therefore produces a direct impact on the electrical transport mechanisms of the PV cell. Recombination effects can happen on the entire cell structure, from each individual layer to their interfaces. As CIGSe layer has a much lower band gap than the upper ones, most of the current contribution comes from it, therefore most of the recombination effects happens at it. Importantly, these recombination mechanisms depend on the place they are happening within the photoabsorber, and each one can be mathematically evaluated. Interestingly, the presence of crystallographic imperfections or chemical impurities, as secondary phases of CIGSe crystal, is what triggers more recombination effects [32, 33].

1.3.3 Photovoltaic structure

CIGSe PV systems can have substrate or superstrate cell configurations. In the first case, light passes through a transparent front contact layer, whereas in the superstrate configuration light passes through a transparent substrate and reaches the active layer. Substrate configuration is the most common one, since it provides the most efficient PV cells due to favorable processing conditions [34, 35]. The common structure of a CIGSe PV (a, b), together with the respective band alignment (c) are depicted in Figure 1.8. The PV device has a complex layered structure consisting of soda-lime glass (SLG)/Mo/CIGSe/CdS/i ZnO/ZnO:Al (AZO), wherein (i) SLG is the PV substrate; (ii) Mo is the back contact coated on SLG; (iii) CIGSe is the *p*–type photoabsorber thin film of copper indium gallium diselenide; (iv) CdS is the buffer layer of *n*–type cadmium sulfide; (v) *i*–ZnO is the resistive layer of intrinsic zinc oxide; and finally (vi) AZO is a transparent conducting window layer of aluminum-doped zinc oxide.

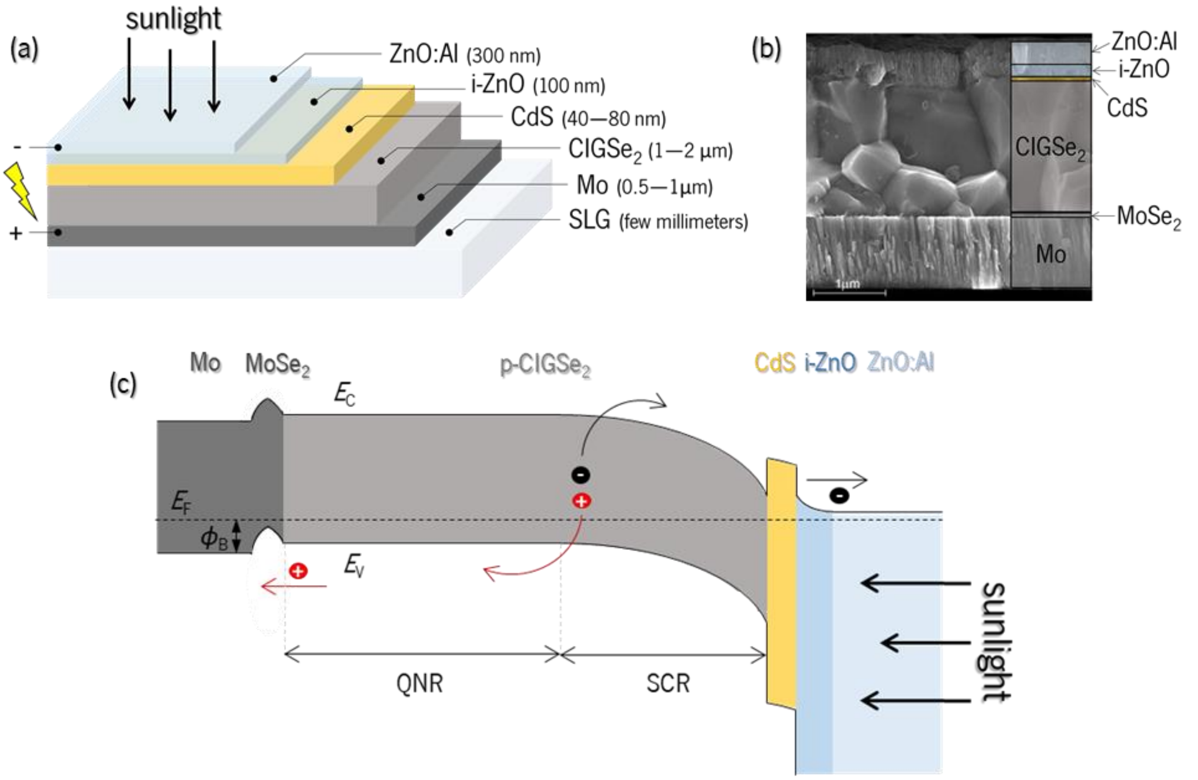

Figure 1.8. Common layered structure of a CIGSe PV device (a), together with the respective cross-section scanning electron microscopy (SEM) image adapted from [36] (b) and a band diagram under equilibrium (c). E_C = conduction band energy, E_V = valence band energy, E_F = Fermi energy, SCR = space charge region, QNR = quasi-neutral region, ϕ_B = barrier height.

As substrate, rigid SLG is very commonly used in CIGSe PVs (Figure 1.8a, b), mostly due to its high thermal stability and capability of supplying sodium to the CIGSe layer during fabrication, which increases the PV cell efficiency. Equally interesting stainless-steel foil [37] and polyimide [38] are employed as well, which provide lightweight flexible PV cells with reduced cost and easy reorientation to sunlight. Importantly, such flexible substrates are also suitable for roll-to-roll large scale fabrication processes.

With regard to current collection, the most commonly used back contact is Mo (Figure 1.8a, b). This is mainly due to its low electrical resistivity (5×10^{-6} Ω cm) and good corrosion resistance. Additionally, Mo forms a very thin layer of MoSe$_2$ at the interface with the CIGSe photoabsorber (Figure 1.8b), thus providing a quasi-ohmic contact between the Mo back contact and the photoabsorber [34, 39]. Transparent conductive oxide (TCO) substrates, e.g., tin–doped indium oxide (ITO) [40] and fluorine-doped tin oxide (FTO) [41], have also been successfully employed in CIGSe PV cells. TCOs are useful for applications that require transparency [42], and in some cases, when combined with metallic reflectors, the substrate reflectivity is improved as compared to Mo–coated SLG [43].

The stoichiometry [Cu] / [In + Ga] $= 0.8–0.9$ and [Ga] / [In + Ga] $= 0.3$ is essential to obtain highly efficient PV cells with a proper CIGSe photoabsorber [34, 39, 44]. The presence of a Ga gradient in the photoabsorber thin film is very commonly observed, as it works as a passivation layer for the Mo back contact, protecting it from recombination of charge carriers. Notably, the recently explored ultrathin CIGSe photoabsorbers (< 1 µm) exhibit a lower absorption of photons and a higher recombination at the back contact. In this particular case, a Ga gradient is not sufficient to prevent charge recombination, and therefore passivation layers, such as $\mathrm{Al_2O_3}$ [45], $\mathrm{MgF_2}$ [46], $\mathrm{SiO_2}$ [47], and $\mathrm{TiO_2}$ [48], have been developed to be placed between the Mo back contact and the CIGSe photoabsorber. Importantly, ultrathin CIGSe photoabsorber layers significantly reduce the use of rare and expensive In and Ga elements and consequently the PV production costs, rendering them very attractive for industrial scale production. PV cells with over 10% efficiency have already been developed using only 450 nm thick CIGSe thin films [49].

To create a *p–n* junction in high-efficiency CIGSe PVs, CdS, with a band gap of 2.4 eV, is most commonly used as a buffer layer (Figure 1.8a, b) [34, 39]. Alternatives, such as $\mathrm{In_2Se_3}$ [50], ZnTiO [51], $\mathrm{Zn_{1-x}Mg_xO}$ [52], and Zn(O,S) [53], have also been successfully used. The latter materials have higher band gaps, thus reducing optical losses inside the buffer layer, but more importantly, they circumvent the use of the toxic Cd metal [54].

TCOs are commonly used as front contacts owing to their high optical transparency (> 85%) and low electrical resistivity ($\leq 10^{-3}$ Ω cm). High-performing CIGSe PV cells employ bilayered TCO consisting of a thin film of *i*–ZnO and a thicker film of AZO (Figure 1.8a, b) [34, 39]. Alternatively to *i*–ZnO/AZO assembly, materials with large band gaps, such as ITO [55], $\mathrm{ZnO_{1-x}S_x{:}\,Al}$ [56], $\mathrm{Zn_{1-x}Mg_xO{:}\,Al}$ [57], $\mathrm{ZnO{:}\,B}$, $\mathrm{In_2O_3{:}\,Mo}$ [58], and $\mathrm{In_2O_3{:}\,H}$ [59], have been employed as front contacts, thus increasing the transmission of ultraviolet photons to the CIGSe photoabsorber.

The different band gap energies and electron affinities of the individual layers affect the band alignment and shape the discontinuity of the conduction band at the interfaces, producing a band diagram (Figure 1.8c). At the interface between CIGSe and CdS, a positive discontinuity of the conduction band, a spike, occurs. When the spike is too high, the flow of the charges from CIGSe to CdS layers is inhibited, reducing the short-circuit current density (J_{sc}). When the spike is small, the electrons are thermally emitted across the spike, and the spike does not work as a barrier [60, 61].

1.3.4 Reliability and recycling

Prior to commercialization, PV modules are subjected to qualification tests to ensure that its installation and usage is safe outdoors. Advantageously, CIGSe PV modules are very reliable, showing degradation of only ≈0.5% per year. The degradation of CIGSe PV modules can be attributed to (*i*) metastabilities, (*ii*) partial shading and hotspots, (*iii*) potential-induced degradation, and (*iv*) back contact issues [62, 63]. Among environmental factors, humidity has been established to lead to the highest degradation rate of CIGSe PVs. To overcome this, encapsulation of the PV modules is performed [64].

CIGSe PV modules evolution highly contributes to the environmentally friendly energy production. However, when the life cycle of these panels comes to an end, they become a hazardous waste if not recovered or disposed properly. To guarantee the sustainability of the PV modules, is very important to establish end of life management strategies [65] with low cost recycling technologies. On the contrary of Silicon PVs, CIGSe technology have only few recycling attempts implemented. As an example, the Japanese government after removal of the frame and backsheet, performs the pyrolysis of polymers in a furnace and the chalcopyrite layer is grated. Loser Chemie company, on the other hand, owns a patent where after crushing and separating the materials, a chemical treatment is performed to recover the semiconductor materials. More important, large-scale chalcopyrite PV systems are currently recycled using a combination of mechanical and chemical treatments [65, 66].

1.3.5 Current fabrication methods

From the fabrication point of view, the most efficient CIGSe PV cells are developed using vacuum-based deposition processes, which allow a fine control of the deposition parameters, thus affording for reproducible fabrication of high-quality thin films (i.e., crystalline, phase pure, semiconducting, compact, smooth, etc.) [67]. For example, the most extensively developed large-area deposition processes (sputtering, co-evaporation, physical or chemical vapor depositions) are industrially-relevant vacuum-based methods for the fabrication of CIGSe solar cell modules. On the other hand, small-area deposition methods (pulsed laser deposition, molecular beam epitaxy) are commonly used in the laboratory research to advance CIGSe PVs.

In the typical scenario of CIGSe PV fabrication, the Mo back contact is first deposited on a rigid or flexible substrate followed by the deposition of either Cu–In–Ga alloy or chalcogenide Cu–In–Ga–Se thin film. Next, the resultant film is subjected to the so-called selenization – gas-transport reaction in Se or $\mathrm{H_2Se}$ vapors of CIGSe crystal growth under 450–600 °C – in order to obtain a high-quality CIGSe photoabsorber layer. The PV device is then completed by the deposition of the aforementioned consecutive layers (Figure 1.8), thus affording a high-performing CIGSe solar cell.

The major challenge in the commercialization and market uptake of second-generation CIGSe PV technology is the high cost and the associated environmental impact of the PV fabrication [68]. For example, vacuum processes have been employed for the fabrication of the current champion CIGSe PV with complex cell structure $\mathrm{SLG/Mo/Cu(In,Ga)S,Se_2/CsF/Zn(O,S,OH)_x/ZnMgO/ZnO{:}B/Al/MgF_2}$ [20], thus marking the high versatility and broad applicability of these methods. However, vacuum-based depositions are quite equipment expensive, energy demanding, and time consuming, and an additional shortcoming is imposed by the challenge of uniform film deposition over large substrate areas, which is desired for the production of working PV modules.

Importantly, the number of non-vacuum approaches has gradually increased in the recent years, since such methodologies not only enable challenging fabrication of CIGSe PVs to be carried out in cost-efficient fashion with low environmental impact, but also potentially afford large-scale fabrication via industrial roll-to-roll and screen printing processes.

1.4 Printed/solution-processed CIGSe photovoltaic systems

The non-vacuum approaches can be divided into three classes: (i) electrodeposition, (ii) particulate ink, and (iii) solution ink [69]. Electrodeposition is beyond the scope of this work and for an overview of this process, the readers are referred to the literature [70, 71]. Particulate inks are suspensions of synthesized or commercial particles in solvents (Figure 1.9a, b), while solution inks typically consist of metal salt precursors dissolved in the solvent (Figure 1.9c). The formulated inks are further deposited on a substrate (Figure 1.9d) and subjected to a thermal treatment when required (e.g., calcination, annealing, selenization) to produce a dense CIGSe layer (Figure 1.9e). Both particulate and solution approaches are perfectly fit for printing deposition of the thin film, but the rheological properties of the inks need to be tuned for the chosen printing method. At the moment, CIGSe PVs with similar efficiencies of 17.1% and 17.3% have been achieved using printing technologies employing particulate [72] and solution [73] inks, respectively.

To date, the champion vacuum-derived CIGSe PV cell displays higher efficiency than those obtained by solution processing (23.35% [20] and 17.3% [73], respectively). Notwithstanding the current lower efficiencies, non-vacuum technologies present many positive aspects, such as lower cost, reduced material waste, decreased energy demand, higher resolution of the deposition, operation at RT, straightforward device miniaturization, higher tolerance to flexible substrates, and compatibility with roll-to-roll and screen printing industrial productions [74].

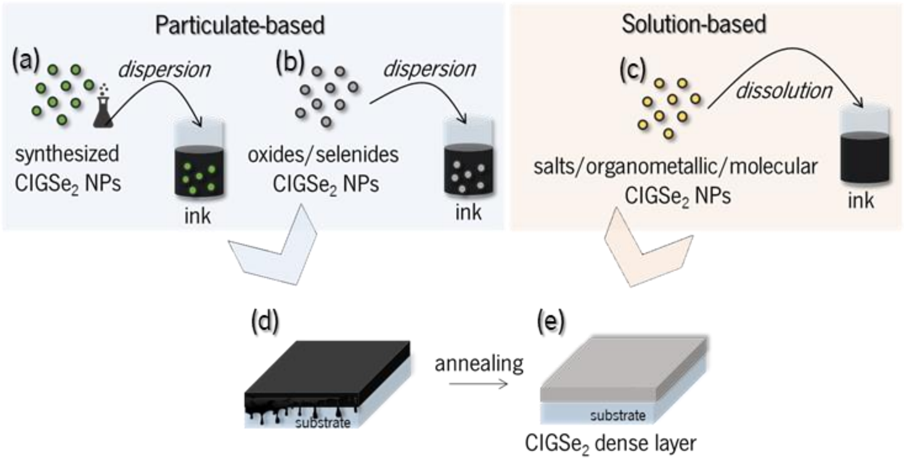

Figure 1.9. Formation of inks for the CIGSe layer using particulate-based synthetic route (a), particulate-based commercial route (b), and solution-based process (c). CIGSe deposited film (d) and CIGSe dense layer after annealing (e).

1.4.1 Nature of ink precursors

In the particulate ink process, the particles used can be either synthesized colloidal CIGSe nanoparticles (NPs) [75-77] or synthesized non-colloidal CIGSe NPs as well as commercially available precursors, for instance, metal oxides. CIGSe NPs have been synthesized by solvothermal [78], hydrothermal [79], hot-injection [80-82], heating-up [83-87], and mechanochemical [88, 89] methods. Accordingly, Cu, In, Ga, and Se metals are used as elemental species or salts dissolved in organic solvents to react and produce a precipitate. Usually, these procedures provide nanocrystalline CIGSe with precise phase and shape control. On the other hand, the scale-up of these procedures is hindered by the use of complex reaction set-ups incorporating autoclaves, Schlenk lines, or gloveboxes. Furthermore, these methods employ toxic organic solvents, such as hydrazine [90], ethylenediamine [78], and trioctylphosphine [81], as well as high boiling point solvents, such as oleylamine [80, 82-86] and hexadecylamine [81, 87] with reaction temperatures above 280 °C, resulting in carbon residues in the obtained films [91]. The highest PV cell efficiency obtained with a colloidal CIGSe NP procedure is 15.0%, using hybrid solvothermal/hot-injection method with sulfur/oleylamine and subsequent selenization treatment to grow the crystal [92].

Environmentally friendly synthesis of CIGSe remains rather unexplored in the literature. Le and co-workers established a method with a less complex experimental set-up based on sonochemistry with ethanol as solvent [93], while Juhaiman et al. reported a microwave-assisted synthesis without organic solvents [94]. Chaure and co-workers synthesized CIGSe NPs using a chemical ion reduction method with polyethylene glycol as solvent and stabilizer and sodium borohydride as reducing agent, delivering a PV cell with 9.3% efficiency [41]. However, the transition to aqueous synthesis of colloidal CIGSe NPs has not been achieved yet, as strongly agglomerated NPs typically result with no suitable control of the crystal phase or size distribution. Based on the use of capping ligands (stabilizers) in non-aqueous synthesis to produce more stable and uniform CIGSe NPs recently, aqueous colloidal synthesis of quaternary chalcogenide $\mathrm{Cu_2ZnSnS_4}$ NPs [95] and ternary CISe NPs [96] have been addressed. Such works give hope for an aqueous colloidal synthesis of CIGSe NPs.

The commercial route, usually using metal oxides or selenides as precursors, gives access to PV cells with higher efficiency than those produced with synthesized NPs. When using oxides, a two-step thermal treatment is required to provide a dense and uniform CIGSe layer. First, a thermal treatment (≈500 °C) with a reductive atmosphere converts the oxides to a Cu–In–Ga alloy. Then, a selenization (≈550 °C) introduces Se and grows the crystal. This method usually produces a Ga segregation on the back contact which negatively impacts the photovoltaic performance. Maximum efficiency of 13.6% has been achieved by this process [97], using a hybrid solution/particulate ink process of sequential chemical reactions to obtain the metal oxides. When metal selenides are used as precursors, the particles are mixed and subjected to a single thermal treatment. An efficiency of 17.1% has been achieved by the company Nanosolar using this process, however, Ga segregation was also identified as a problem [72].

The solution ink process employs metal salts, organometallic, and molecular precursors as solutions, which omits the need for additives, leading to a homogenous layer composition with a lower number of defects than particulate inks. This process can include a final annealing treatment or not [44]. Among solution ink processes, the molecular approach provides higher efficiency PV cells (17.3%), however, it employs the highly toxic and explosive hydrazine, the use of which is not allowed at industrial-scale production [73]. Greener solutions using ethanol and propylene glycol followed by post-selenization treatment have delivered efficiencies of 8.0% and 12.4%, respectively [98, 99].

1.4.2 Selenization

Selenization is a gas-transport reaction that occurs when a film containing Cu, In and Ga precursors is exposed to a thermal treatment with Se vapor under controlled atmosphere. Se element can be also supplied in the gas phase in the form of $\mathrm{H_2Se}$, turning the process faster and providing more homogenous and larger crystals than those obtained by elemental Se vapor, however this last is less toxic and therefore desirable. During this process, in addition to the growth of the crystal, when using Mo back contacts, a $\mathrm{MoSe_2}$ thin layer is created between the back contact and the photoabsorber layer producing a quasi-ohmic contact, which is beneficial for the PV cell efficiency [24, 100].

The growth of the CIGSe crystal is a complex process, turning challenging the control of its crystallization parameters. Initially, binary selenides of Cu and In grow, followed by the growth of the CISe phase around 370–380 °C, and the $\mathrm{CuGaSe_2}$ phase at around 425 °C. The complete growth of the CIGSe crystal occurs at T > 500 °C by the slow interdiffusion between CISe and $\mathrm{CuGaSe_2}$ along with Ga segregation towards the back contact. This segregation occurs due to a more favorable reaction between In–Se than Ga–Se and tends to create a lower energy band gap at the SCR of the photoabsorber, leading to poor V_{OC} [100]. Nevertheless, it can be overcome by performing a sulfurization after selenization [100].

Selenization can be performed using a rapid thermal annealing (RTA) or a one-step, two-step, or even three-step selenization procedure. RTA provides a short and scalable thermal treatment [101], while two and three-step selenization promotes a slow interdiffusion step between CISe and $\mathrm{CuGaSe_2}$, ensuring their homogenization [100]. All thermal treatments use a specific setup usually comprising a furnace and a horizontal quartz reactor tube to withstand high temperatures. The conditions of the process depend on the composition and deposition of the film and need to be optimized in terms of temperature, time, pressure, atmosphere, and Se concentration. In some cases, the films are placed inside a graphite box to ensure constant partial pressure and temperature to grow the CIGSe crystals [101, 102].

Despite providing large and homogenous crystals, selenization releases toxic Se vapors, which are hazardous to humans in large-scale production, rendering it non-suitable for roll-to-roll processes. To overcome this hazardous process, one can deposit thin films with ink formulation comprising synthesized CIGSe NPs, as no further selenization is required in this approach. Though, it requires a high temperature annealing for obtaining dense photoabsorber films, which are undesirable specially when considering the use of flexible substrates and roll-to-roll production. Femtosecond laser annealing, on the other hand, does not require temperature, is more compatible with industrial production and has demonstrated to enhance the efficiency of the devices [103], turning it a great solution to replace conventional annealing treatments.

1.4.3 Inks and deposition processes

Not only the ink formulation determines the quality of the films, but also the type of substrate and the post-deposition treatment to apply. It plays a huge role in cost, as well as, on the range of applicability of the resulting PV cell. An ink formulation comprises a precursor, a solvent, and additives. In addition to the precursor quality, the solvent is a key element for a good dispersion/dissolution. Solvent polarity, reactivity, surface tension, viscosity, and volatility must be considered not only to adjust the ink's properties for the chosen deposition process but also to guarantee a suitable dispersion/dissolution of the precursors [104]. The use of additives, such as binders and surfactants, helps to adjust the ink's viscosity and surface tension, improving its wettability, dispersion, and stability and therefore leading to dense and smooth CIGSe layers, without voids. Binders are synthetic or natural polymers and surfactants are ionic or non-ionic surface tension modifiers [74, 104]. The additives also enhance the integrity of the films by improving their adhesion to the substrate and preventing cracking and delamination during the post-deposition thermal processes, which compromise the device's performance.

Particulate-based inks with synthetic precursors allow for a higher control of the layer's composition, with the only lack of homogeneity arising from its thickness, which does not affect the crystal stoichiometry. These NPs, when synthesized without stabilizers, need surfactants to produce an ink formulation with uniform composition. With commercial precursors, NP agglomeration is very common and leads to different settling rates in the solution, compromising the correct stoichiometry within the films. Although surfactants can provide a solution, they may leave residues even after annealing the films which compromise their quality, turning it a challenging process [74].

Inks from solution-based precursors are generally more homogeneous on the molecular level and are often considered an excellent choice to achieve smooth layers with uniform composition. However, the precursors' dissolution is a limiting step, as an incomplete dissolution can result in cracks and shrinkage of the films during annealing. Consequently, the components of the ink, as well as, the temperature and pH should be carefully selected to promote complete solubilization and avoid the premature precipitation of the precursors [74].

Table 1.2 shows the highest PV cell efficiencies achieved by printing/coating the CIGSe or CISe layer, showing the nature of the precursors, ink formulation, post-deposition treatments, and substrate. From this table it is evident that most of the PV cells showing the highest efficiencies are obtained using toxic or hazardous solvents. More importantly, all procedures use selenization, which is non-suitable for a roll-to-roll sustainable fabrication.

Table 1.2. Most efficient PV cells comprising printed/coated CIGSe/CISe layer, with corresponding precursor nature, ink formulation, deposition process, and substrate.

Precursor nature	Ink formulation		Post-deposition treatment	Substrate	Deposition process	Efficiency (%)	Ref.
	Solvent	Additives					
Particulate-based (commercial)	No information	No information	Atmospheric-pressure RTA (no gas or temperature(T) information)	Mo-coated Al foil	Not revealed	17.1	[72]
Solution-based (molecular)	Hydrazine	–	Annealing 500–600 °C (N_2)	Mo-coated SLG	Spin coating	17.3	[73]
Solution-based (molecular)	Hydrazine	–	Annealing 540 °C (N_2)	Mo-coated SLG	Spin coating	15.2	[105]
Particulate-based (synthetic)	Toluene	–	Annealing and selenization (N_2) (no T information)	Mo-coated SLG	Spin coating	13.8	[106]
Hybrid particulate-based (synthetic) + solution-based (salts)	2-methoxyethanol + ethanolamine	–	Calcination 100 °C and 270 °C Selenization 600 °C (90 torr)	Mo-coated SLG	Spin coating	5.1	[107]
Particulate-based (synthetic)	Hexanethiol	–	Calcination 350 °C Selenization 500 °C	Mo-coated SLG	Blade coating	15.0	[92]
Solution-based (salts)	Tetramethylguanidine + methanol	Sodium thiocyanate	Annealing 200 °C (N_2) Selenization 600 °C	Mo-coated SLG	Blade coating	13.3	[108]
Particulate-based (synthetic)	Hexanethiol	–	Selenization 500 °C	Mo-coated SLG	Blade coating	12.0	[82]
Solution-based (salts)	2-Propanol	Anhydrous ethylene glycol	Calcination 250 °C Two-step selenization 400/560 °C	Mo-coated SLG	Inkjet printing	11.3	[109]
Solution-based (salts)	Ethanol + ethanolamine	Ethylene glycol	Calcination 300 °C Selenization 500 °C	Mo-coated SLG	Inkjet printing	5.0	[110]
Solution-based (salts)	Water	Sodium nitrate	Annealing 330–360 °C (N_2) Selenization 560 °C	Mo-coated SLG	Spray coating	10.7	[111]
Solution-based (salts)	1,2-Ethylenediamine + 1,2-ethanedithiol + ethylacetate	–	Calcination 310 °C Selenization (no T information,53 kPa)	Mo-coated SLG	Spray coating	9.8	[112]
Particulate-based (commercial)	2-Mercaptoethanol	Ethyl cellulose	Calcination 300–400 °C Annealing 500 °C (Ar/H_2) Selenization 550 °C	Mo-coated SLG	Screen printing	2.4	[113]
Particulate-based (commercial)	Diethylene glycol monobutyl ether	Ethyl cellulose	Calcination 400 °C Annealing 500 °C (Ar/H_2) Selenization + sulfurization 500 °C	Mo-coated SLG	Screen printing	2.2	[114]

Due to their toxicity, harmfulness, and damage to the environment, replacement of hazardous organic solvents, such as hydrazine, toluene and hexanethiol, in industrial processes is essential from the green chemistry and sustainability point of view. Solvents have been ranked according to their environmental safety and health characteristics [115, 116], which helps in the selection of green solvents and discourages the use of hazardous ones, that are commonly used in laboratories. Green solvents are environmentally friendly solvents derived from the processing of crops. In the search of environmentally friendly inks for the CIGSe layer (Table 1.3), environmentally friendly propanol, ethanol, and water-based inks have been employed.

However, in most cases, a hazardous selenization treatment is employed. An option to avoid selenization is to synthesize high-quality CIGSe NPs, incorporate them into green particulate ink formulations, and annealing the film without Se source. To avoid high temperature annealing, a method was developed where the layer was crystallized using powerful lasers, which does not represent a danger to humans or the environment, and it is more feasible for the roll-to-roll industry [117-119].

Table 1.3. Environmentally friendly alternatives for CIGSe PV cells comprising printed/coated CIGSe layer, with the corresponding precursor nature, ink formulation, deposition process, and substrate.

Precursor nature	Ink formulation		Post-deposition treatment	Substrate	Deposition process	Efficiency (%)	Ref.
	Solvent	Additives					
Hybrid solution-based + particulate-based (commercial)	Water	No information	Annealing 500–550 °C (N/H_2) Selenization 420–450 °C	Mo-coated SLG	Not revealed	13.6	[97]
Solution-based (salts)	Water	Sodium nitrate	Annealing 330–360 °C (N_2) Selenization 560 °C	Mo-coated SLG	Spray coating	10.7	[111]
Particulate-based (synthetic)	Water	–	Pulsed laser annealing with pulser fiber laser (1064 nm) under air and RT	CdS/ZnO/AZO-coated SLG	Spray coating	1.1	[117]
Particulate-based (synthetic)	Ethanol	–	Flash-light (9W in air at RT)	Mo-coated SLG	Spray coating	0.2	[118]
Particulate-based (synthetic)	Ethanol + ethylene glycol	–	Annealing 450 °C (Ar)	FTO-coated SLG	Blade coating	9.3	[41]
Particulate-based (synthetic)	Propanol	Cationic dispersant	Two-steps selenization: 350/540 °C	Mo-coated SLG	Blade coating	5.6	[120]
Solution-based (salts)	Ethanol	–	Selenization 550 °C Sulfurization 550 °C	Mo-coated SLG	Spin coating	12.4	[99]
Solution-based (salts)	Ethanol + propylene glycol	–	Calcination 350 °C Selenization 500–530 °C	Mo-coated SLG	Spin coating	8.0	[98]
Solution-based (salts)	Water	Polyethylene glycol	Calcination 150 °C Two steps selenization 250/550 °C	Mo-coated SLG	Inkjet printing	4.0	[121]

The following deposition processes: spin coating, blade coating, inkjet printing, spray coating, and screen printing are the most relevant ones to produce CIGSe films (Figure 1.10), and their main advantages, limitations, and principal parameters are addressed in Table 1.4.

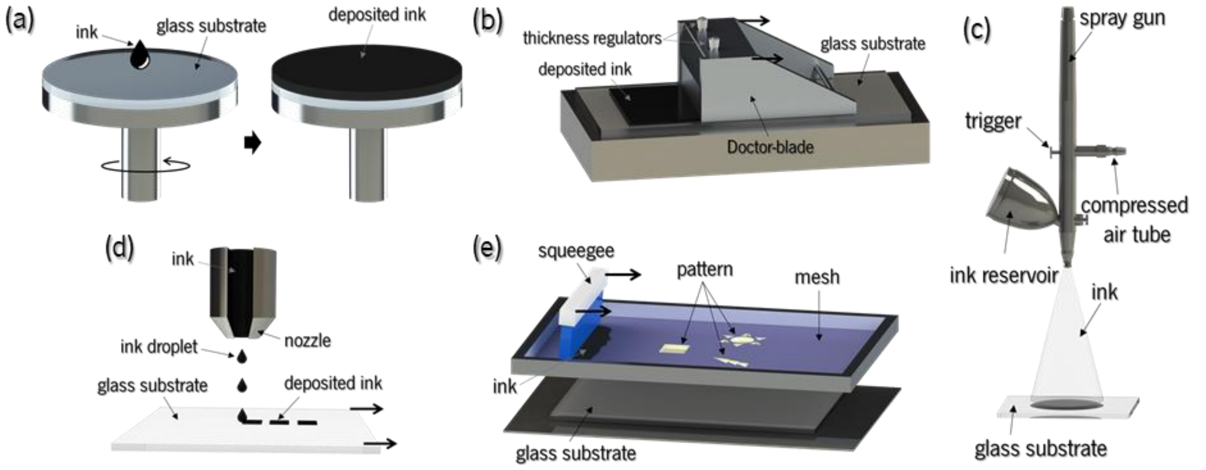

Figure 1.10. Schematic representation of deposition processes, spin coating (a), blade coating (b), spray coating (c), inkjet printing (d), and screen printing (e).

Among these processes, spin coating provides most efficient CIGSe PV cells, with 17.3% [73]. The associated simplicity, low cost and needless of rheology additives are the major characteristics leading to its implementation on PVs production. However, a significant amount of material is wasted during the inks deposition and more importantly spin coating is the only process herein focused that is not compatible with roll-to-roll industry, limiting its employment on scale-up production of PVs. Blade coating, beyond its compatibility with roll-to-roll industry, is very simple, low-priced and the second most efficient deposition process with CIGSe PV cells reaching up to 15.0% of efficiency [92]. Nevertheless, its low control over the deposited layer thickness is a limiting step for reproducible industrial production of PVs. Similarly, spray coating with CIGSe PV cells with a maximum 10.7% of efficiency [111], despite providing a higher throughput than blade coating, the low control over the thickness is the major limitation as well. The use of inkjet not only affords a strict control over the layer thickness, as produce no waste, and requires simple low viscosity inks formulations. PV cells with 11.3% of efficiency [109] were accomplished and despite the roll-to-roll compatibility, clothing problems are quite common during the printing process. To avoid it, the particles dispersion should be carried out with extra caution, since the presence of agglomerations can lead to serious damages on the equipment.

Table 1.4. Comparison of deposition processes for CIGSe/CISe layer with advantages, limitations, and characteristics [24, 122].

	Spin coating	**Blade coating**	**Inkjet printing**	**Spray coating**	**Screen printing**
Advantages	- Simple - Good control over thickness for small areas - Low cost	- Better stoichiometry control - Low cost	- Precise control over thickness and pattern - Maskless technique	- Simple - Low cost - High throughput	- Simple - Low cost - Good control over thickness - High throughput
Limitations	- Low control over thickness for large areas	- Low control over thickness	- Difficult ink preparation (clothing) - High cost	- Low control over thickness	- Ink preparation (high viscosity)
Material waste	Significant	Little	None	Some	None
Wet thickness (μm)	1–200	10–200	0.5–5	5–200	10–100
Ink viscosity (cP)	<10	<10	<10	10–1000	100–100,000
Pattern resolution	Zero-dimensional	One-dimensional	Three-dimensional 16–50 μm	Zero-dimensional	Two-dimensional 30 μm
Roll-to-roll compatibility	No	Yes	Yes	Yes	Yes
Highest efficiency PV cell (%)	17.3 [73]	15.0 [92]	11.3 [109]	10.7 [111]	2.4 [113]

Notably, screen printing (Figure 1.11) is the least explored process with no devices produced using CIGSe crystal. Nevertheless, when using CISe the maximum efficiency achieved by a screen-printed device is 2.4% [113]. Despite the need of an additive to meet the high viscosity requirement, it is a very promising approach since it allows the deposition of large dimension layers with a good uniformity, high resolution and low cost, which is very attractive for roll-to-roll industry. Furthermore, it is the most suitable process to print layers with few micrometers of thickness, desirable for the CIGSe layer [123]. Although no PV cells with screen-printed CIGSe layer have been reported, its deposition is being optimized in both rigid [124, 125] and flexible substrates [126, 127].

Interestingly, screen printing is a very simple process commonly used in the textile industry. It can be used to print active layers and produce devices on many different substrates, such as glass, polymer, textile, metal, and paper. The printed pattern is created by first placing a mesh above the chosen substrate (Figure 1.11a), then with the use of a squeegee, the ink is spread through the mesh by applying pressure on it until the mesh touches the substrate. With a $45°$ angle between the squeegee and the mesh and a continuous pressure and velocity of the squeegee, the ink will pass through the mesh (Figure 1.11b) and finally print the desired pattern on the substrate (Figure 1.11c). A subsequent low-temperature treatment is performed to evaporate the solvent used in the ink formulation.

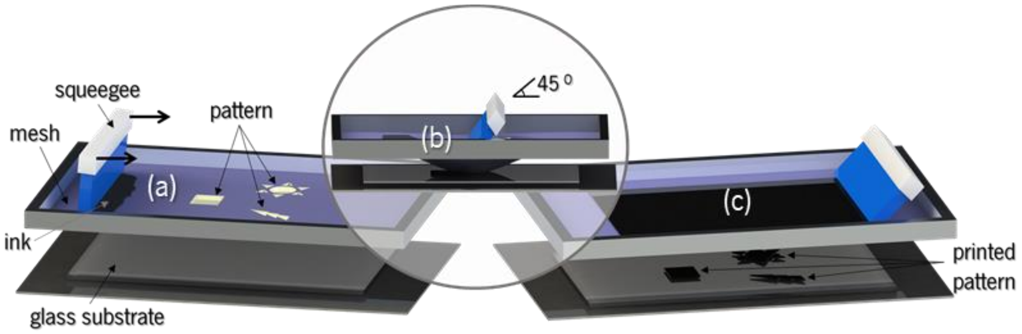

Figure 1.11. The screen printing process steps and elements; placement of the mesh with the printing pattern above the chosen substrate (a), spread of the ink through the mesh by a squeegee (b) and achievement of the printed pattern over the substrate (c).

When implemented in roll-to-roll processing, printing technologies enable a much larger throughput, improving the development of flexible lightweight devices and their miniaturization, expanding the devices field of application. This idea has been attracting much attention during the last decade, driving several researchers to put effort into fully printed device development in many different fields [128-131].

1.4.4 Fully-printed/solution-processed CIGSe photovoltaic systems

Combining printing techniques with the roll-to-roll process is of high benefit for a PV cell's final price. In addition, the amount of waste products and the energy demand are lower than vacuum-processed devices, resulting in a more sustainable way to produce PV cells. A few fully solution-processed PV cells have been recently developed [132-135] and currently, their major limitation lies in the low efficiency, mostly stemming from the photoabsorber layer. As an example, a fully printed $\mathrm{CuInS_2}$ chalcogenide PV cell delivered a maximum efficiency of 7.2% [136-138].

Very few examples of fully solution-processed CIGSe PVs have been reported. Nagino et al. [139] reported the one with the highest efficiency of 10.9%. It comprises an FTO back contact spray-coated over SLG, a spin-coated CIGSe layer, with a final annealing and selenization under 550 °C to grow the crystal.

There is no specification about the precursors nature, ink formulation or deposition process used. Thereafter, a CdS layer deposited by chemical bath and both ZnO NPs, working as a high-resistance buffer, and Ag nanowires (NWs), working as a transparent front contact, were sequentially spin coated. Finally, Ag grid electrodes were screen-printed on top of Ag NWs.

Another fully solution-processed CIGSe PV cell showed an efficiency of 1.6% [140]. CIGSe NPs synthesized in dodecylamine were suspended in *o*-dichlorobenzene to produce a spin-coating ink, which was further annealed, without the need of selenization. Next, the CdS buffer and a conductive layer of sol–gel derived ZnO precursor solution were spin-coated sequentially. ZnO precursor solution comprises 2-methoxyethanol and monoethanolamine solvents. Finally, AgNWs were spin-coated over the ZnO layer, and finally, another ZnO layer was spin-coated on top of it, requiring final annealing of 200 °C. The authors attribute the low efficiency of the device to the poor quality of the photoabsorber film. More specifically, the low CIGSe particle size (20 nm) results in a partly dense film which increases the potential recombination of charge carries, and therefore decreases the photovoltaic performance.

The limited efficiency given by fully printed/solution-processed PV cells typically stems from the CIGSe photoabsorber layer deposition [141]. While the search for more effective printed CIGSe layers is ongoing, improvements have been achieved on the buffer and front contact layers. Regarding the CdS buffer layer, chemical bath deposition (CBD) is a well-established method used in high-efficiency CIGSe PV cells [142]. Although it is a non-vacuum deposition process, the toxicity of Cd has driven the search for greener alternatives [20].

Printable transparent front contacts, on the contrary, have been extensively investigated. In addition to the basic requirements on high transmittance and conductivity, the maximum processing temperature should not exceed 220 °C, otherwise, the layers below will be compromised. There are several candidates fulfilling these requirements, such as conductive polymers, carbon allotropes, and metal NWs [143]. Printable front contacts have been developed to be implemented in CIGSe PV cells with vacuum-deposited CIGSe layer to replace the commonly used vacuum-deposited ZnO and AZO layers (Table 1.5). Among all the candidates, AgNWs seem to be a viable solution due to their excellent optical and electrical properties as well as low-temperature deposition [143]. The combination of these highly efficient printable transparent top contacts with well-established buffer layer deposition and more homogenous CIGSe printed layers will provide fully printed CIGSe PV systems with higher efficiency and bring this technology to a higher commercially competitive path comparable to vacuum-based CIGSe PV cells.

Table 1.5. Printed conductive transparent top layers (first layer on the left) used in CIGSe PV cells and their R_s, transmittance at 550 nm (T_{550nm}), and the reported efficiency.

PV cell configuration	Deposition process	R_s (Ω/sq)	$T_{550\text{nm}}$ (%)	Efficiency (%)	Ref.
SWCNT/*i*-ZnO/CdS/CIGSe/Mo/SLG	Spray coating	50	78	19.5	[144]
AZO/AgNWs/AZO/*i*-ZnO/CdS/CIGSe/Mo/SLG	Spin coating	11	93	11.0	[145]
AgNWs-ITO NP/ZnS/CIGSe/Mo/SLG	Spin coating	23	87	8.0	[146]
AgNWs+PEDOT:PSS/Zn(S,O,OH)/CdS/CIGSe/Mo/SLG	Spray coating	12	82	11.6	[147]
AgNWs/AZO/*i*-ZnO/CdS/CIGSe/Mo/SLG	Spray coating	20	92	14.1	[143]
ZnO/AgNWs/ZnO/CdS/CIGSe/Mo/SLG	Spin coating	11	90	13.5	[148]

1.5 Objectives

The main objective of this work was to develop a new generation of sustainable and cost-efficient CIGSe PV cells using solution processing methodologies for the photoabsorber layer deposition. To meet this goal, screen-printable inks comprising well-dispersed CIGSe precursors films, with a nominal metals ratio of [Cu] / [In + Ga] = 0.83 and [Ga] / [In + Ga] = 0.3, were formulated using conventional and sustainable methodologies in concern to the ink's solvents. Importantly, CIGSe precursors with distinct natures were used by following either synthetic or commercial (oxides) route. The resultant inks and printed films were characterized to evaluate their rheological, structural, morphological, optical and physical properties to continue for the PV devices production, using the conventional vacuum-based deposition processes for the upper layers. As ultimate goal, an all-non-vacuum processed CIGSe PV cell was produced by using environmentally friendly inks for both photoabsorber and top conductive layers deposition.

The specific objectives of this work were:

- Formulation of screen-printable inks with tailored rheological properties, comprising either synthesized CIGSe NPs or well-dispersed Cu, In, and Ga commercial oxides, following conventional and environmentally friendly methodologies.
- Screen printing with further thermal treatments for dense and compact CIGSe photoabsorber thin films with great optical properties.
- Production of CIGSe PV cells comprising screen-printed CIGSe photoabsorber, CBD of CdS buffer layer and sputtering of top conductive layers (*i*–ZnO/AZO).

- Formulation of environmentally friendly inks with tailored rheology properties for spray coating of top conductive layers (*i*–ZnO/ITO).
- Production of a sustainable all-non-vacuum processed CIGSe PV cell with screen-printed CIGSe photoabsorber, CBD of CdS buffer layer and spray coating of top conductive layers.

1.6 Structure of the work and methodologies

The herein presented thesis is divided into two major sections: **Section I** – Conventional methodologies for solution-processed CIGSe PV systems and **Section II** – Environmentally friendly methodologies for solution-processed CIGSe PV systems, comprising six chapters, five of them based on published or submitted scientific manuscripts. The arrangement of the sections and chapters follows a sequential ordering for a better understanding of the developed work and represents the implemented methodology to achieve the main and specific goals. A summary of the work addressed in each one of the chapters is next described.

Chapter 1 includes a general introduction to solar energy and PV systems, focusing on CIGSe thin film technology state of the art and the existing partial and full solution processing of CIGSe PV systems, using conventional and environmentally friendly methodologies. The main objectives and the structure of the thesis are addressed, as well. To a better acknowledgment of the achievements, a specific state of the art is provided in each chapter.

Section I, covering conventional methodologies, begins with **Chapter 2** where a large-scale synthesis of CIGSe NPs is addressed. The herein presented heat-up synthesis is conducted in a high boiling point organic solvent working also as a stabilizer, under Schlenk line vacuum and inert conditions. Structural and optical characterization were used for the evaluation of the chemical composition and thermal behavior of the synthesized NPs. Additionally, the NPs were chemically modified to be embedded in a water-based ink for screen printing deposition over SLG, followed by an annealing treatment. The ink rheological properties were characterized for a proper deposition. Moreover, morphological and structural characterizations were conducted on the resulting photoabsorber films to study the impact of the used printing and thermal processes.

Chapter 3 addresses the production of a CIGSe PV cell comprising a screen-printed CIGSe photoabsorber over FTO-coated SLG substrate. The reported ink formulation comprises Cu, In and Ga commercial oxides well-dispersed in terpineol solvent for screen printing deposition followed by calcination and selenization processes. The photoabsorber thin film crystalline structure, morphology, chemical composition and optical properties were evaluated. To complete the device, CBD of a CdS buffer layer and sputtering of *i*–ZnO/AZO were conducted and the photovoltaic performance of the device was evaluated.

In **Section II,** sustainable methodologies for the development of CIGSe PV systems are reported. **Chapter 4** includes a large-scale aqueous synthesis of CIGSe NPs using a natural antioxidant as a complexing agent. The structural and optical properties, as the chemical composition of the resulting NPs were evaluated.

Chapter 5 includes two water-based ink formulations comprising Cu, In and Ga commercial oxides with rheology tailored for screen printing deposition are addressed. The reported work comprises a study of the screen printing deposition over several conductive substrates followed by selenization. The substrate-photoabsorber interfaces were studied and the most suitable substrate was selected to produce a CIGSe PV cell, with screen-printed photoabsorber, CBD of CdS and sputtering of *i*–ZnO/AZO. The photoabsorber structural, morphological and optical properties were evaluated. Here is also addressed the formulation of water-based inks for the top conductive layers *i*–ZnO/ITO, to further produce a sustainable all-non-vacuum processed CIGSe PV cell comprising screen-printed photoabsorber, CBD of CdS and spray coating of *i*–ZnO/ITO. A comparative study between the sputtering and spray coating of top conductive layers was conducted by the evaluation of the photovoltaic performance of the corresponding produced PV devices.

Finally, in **Chapter 6**, the main conclusions of this thesis are presented together with suggestions for future work.

1.7 References

1. *International Renewable Energy Agency*, in *Future of Solar Photovoltaic: Deployment, investment, technology, grid integration and socio-economic aspects (A Global Energy Transformation: paper)*. 2019: Abu Dhabi.
2. *International Renewable Energy Agency*, in *Global energy transformation: A roadmap to 2050*. 2019: Abu Dhabi.
3. *European Comission*, in *Communication from the comission to the european parliament, the european council, the council, the european economic and social commitee and the commitee of the regions: The European Green Deal*. 2019: COM 640 final.
4. Morton, O., *A new day dawning?: Silicon Valley sunrise.* Nature, 2006. **443**(7107): p. 19-22.
5. Hersch, P. and K. Zweibel, *Basic photovoltaic principles and methods*. Technical Information Office Solare Energy Research Institute. 1982, Golden, CO.
6. *International Renewable Energy Agency*, in *Renewable Energy Statistics 2020*. 2020: Abu Dhabi.

7. *International Renewable Energy Agency*, in *10 Years: Progress to Action, 10th Assembly of the International Renewable Energy Agency*. 2020: Abu Dhabi.
8. Bhatia, S.C., *Chapter 5 - Solar photovoltaic systems*, in *Advanced Renewable Energy Systems*, S.C. Bhatia, Editor. 2014, Woodhead Publishing India. p. 144-157.
9. Haque, A., *Chapter 3 - Solar energy*, in *Electric Renewable Energy Systems*, M.H. Rashid, Editor. 2016, Academic Press: Boston. p. 40-59.
10. Shah, A.V., *Chapter IV - Theory of solar cell devices semiconductor diodes*, in *Thin-Film Silicon Solar Cells*. 2010, CRC Press. p. 145-172.
11. Kasap, S.O., *Chapter 6 - Semiconductor devices*, in *Principles of electronic materials and devices*, McGraw-Hill, Editor. 2006. p. 551-563.
12. *National Renewable Energy Laboratory*. Best Research-Cell Efficiency chart; Available from: https://www.nrel.gov/pv/assets/pdfs/best-research-cell-efficiencies.20191105.pdf, accessed on March 2020.
13. Mustansar, C., *Chapter 41 - Engineered Nanomaterials for Energy Applications*, in *Handbook of Nanomaterials for Industrial Applications*, C. Mustansar, Editor. 2018, Elsevier. p. 751-767.
14. Luceño-Sánchez, J.A., A.M. Díez-Pascual, and R. Peña Capilla, *Materials for Photovoltaics: State of Art and Recent Developments.* International journal of molecular sciences, 2019. **20**(4): p. 976.
15. Ando, B. and S. Baglio, *Inkjet-printed sensors: a useful approach for low cost, rapid prototyping.* Instrumentation & Measurement Magazine, IEEE, 2011. **14**(5): p. 36-40.
16. Geisz, J.F., et al., *Six-junction concentrator solar cells.* AIP Conference Proceedings, 2018. **2012**(1): p. 040004.
17. Green, M.A., et al., *Solar cell efficiency tables (Version 55).* Progress in Photovoltaics: Research and Applications, 2020. **28**(1): p. 3-15.
18. Slade, A. and V. Garboushian, *27.6% Efficient Silicon Concentrator Solar Cells for Mass Production*, in *Proceedings of the 15th International Photovoltaic Science & Engineering Conference (PVSEC-15)*. 2005: Beijing.
19. Jung, E.H., et al., *Efficient, stable and scalable perovskite solar cells using poly(3-hexylthiophene).* Nature, 2019. **567**(7749): p. 511-515.
20. Nakamura, M., et al., *Cd-Free Cu(In,Ga)(Se,S)$_2$ Thin-Film Solar Cell With Record Efficiency of 23.35%.* IEEE Journal of Photovoltaics, 2019. **9**: p. 1863-1867.
21. Goetzberger, A. and C. Hebling, *Photovoltaic materials, past, present, future.* Solar Energy Materials and Solar Cells, 2000. **62**(1): p. 1-19.
22. Wagner, S., et al., *CuInSe$_2$/CdS heterojunction photovoltaic detectors.* Applied Physics Letters, 1974. **25**(8): p. 434-435.
23. *CIGS White Paper 2019*. 2019; Available from: https://cigs-pv.net/wortpresse/wp-content/uploads/2019/04/CIGS_White_Paper_2019_online.pdf, accessed on February 2021.
24. Ramanujam, J. and U.P. Singh, *Copper indium gallium selenide based solar cells – a review.* Energy & Environmental Science, 2017. **10**(6): p. 1306-1319.
25. Koebrich, S., T. Bowen, and A. Sharpe, *Renewable Energy Data Book*. Office of Energy Efficiency & Renewable Energy. 2020, U.S. Department of Energy.
26. Stanbery, B.J., *Copper Indium Selenides and Related Materials for Photovoltaic Devices.* Critical Reviews in Solid State and Materials Sciences, 2002. **27**(2): p. 73-117.
27. Schock, H.-W., *Solar Cells, Chalcopyrite-Based Thin Film*, in *Solar Energy*, C. Richter, D. Lincot, and C.A. Gueymard, Editors. 2013, Springer: New York. p. 323-340.
28. Xu, L.-C., et al., *Wurtzite-type CuInSe$_2$ for high-performance solar cell absorber: ab initio exploration of the new phase structure.* Journal of Materials Chemistry, 2012. **22**(40): p. 21662-21666.

29. Rühle, S., *Tabulated values of the Shockley–Queisser limit for single junction solar cells.* Solar Energy, 2016. **130**: p. 139-147.
30. Guillemoles, J.-F., et al., *Guide for the perplexed to the Shockley–Queisser model for solar cells.* Nature Photonics, 2019. **13**(8): p. 501-505.
31. Green, M., et al., *Solar cell efficiency tables (version 57).* Progress in Photovoltaics: Research and Applications, 2021. **29**(1): p. 3-15.
32. Kosyachenko, L.A., et al., *Optical and recombination losses in thin-film Cu(In,Ga)Se_2 solar cells.* Solar Energy Materials and Solar Cells, 2014. **130**: p. 291-302.
33. Kosyachenko, L.A., *Chapter I - A theoretical Description of Thin-Film Cu(In,Ga)Se_2 Solar Cell Performance*, in *Solar Cells: New Approaches and Reviews*. 2015, IntechOpen. p. 1-43.
34. Goswami, D.Y. and F. Kreith, *Chapter 20 - Photovoltaics Fundamentals Technology and Applications*, in *Energy Conversion*. 2007, CRC Press. p. 48-54.
35. Rau, U. and H.W. Schock, *Chapter IC-3 - Cu(In,Ga)Se_2 Thin-Film Solar Cells*, in *Practical Handbook of Photovoltaics (2nd Edition)*, A. McEvoy, T. Markvart, and L. Castañer, Editors. 2012, Academic Press: Boston. p. 323-371.
36. Kaufmann, C.A., et al., *Transfer of Cu(In,Ga)Se_2 thin film solar cells to flexible substrates using an in situ process control.* Thin Solid Films, 2005. **480-481**: p. 515-519.
37. Kawano, Y., et al., *Manipulation of [Ga]/([Ga]+[In]) profile in 1.4-μm-thick Cu(In,Ga)Se_2 thin film on flexible stainless steel substrate for enhancing short-circuit current density and conversion efficiency of its solar cell.* Solar Energy, 2020. **204**: p. 231-237.
38. Chirilă, A., et al., *Highly efficient Cu(In,Ga)Se_2 solar cells grown on flexible polymer films.* Nature Materials, 2011. **10**(11): p. 857-861.
39. Reinders, A., et al., *Chapter 4 - Basics of chalcogenide thin film solar cells*, in *Photovoltaic Solar Energy: From Fundamentals to Applications*. 2017, Wiley. p. 169-212.
40. Li, Y., et al., *Sodium control in Ultrathin Cu(In,Ga)Se_2 solar cells on transparent back contact for efficiencies beyond 12%.* Solar Energy Materials and Solar Cells, 2021. **223**: p. 110969.
41. Londhe, P.U., A.B. Rohom, and N.B. Chaure, *Solar cell studies on $CuIn_{1-x}Ga_xSe_2$ nanoparticles derived from chemical reduction process.* Solar Energy, 2020. **206**: p. 18-26.
42. Saifullah, M., et al., *The role of NaF post-deposition treatment on the photovoltaic characteristics of semitransparent ultrathin Cu(In,Ga)Se_2 solar cells prepared on indium-tin-oxide back contacts: a comparative study.* Journal of Materials Chemistry A, 2019. **7**(38): p. 21843-21853.
43. Gouillart, L., et al., *Development of reflective back contacts for high-efficiency ultrathin Cu(In,Ga)Se_2 solar cells.* Thin Solid Films, 2019. **672**: p. 1-6.
44. Regmi, G., et al., *Perspectives of chalcopyrite-based CIGSe thin-film solar cell: a review.* Journal of Materials Science: Materials in Electronics, 2020. **31**(10): p. 7286-7314.
45. Vermang, B., et al., *Introduction of Si PERC Rear Contacting Design to Boost Efficiency of Cu(In,Ga)Se_2 Solar Cells.* IEEE Journal of Photovoltaics, 2014. **4**(6): p. 1644-1649.
46. Casper, P., et al., *Optoelectrical improvement of ultra-thin Cu(In,Ga)Se_2 solar cells through microstructured MgF_2 and Al_2O_3 back contact passivation layer.* Physica Status Solidi – Rapid Research Letters, 2016. **10**(5): p. 376-380.
47. Yin, G., et al., *Well-Controlled Dielectric Nanomeshes by Colloidal Nanosphere Lithography for Optoelectronic Enhancement of Ultrathin Cu(In,Ga)Se_2 Solar Cells.* ACS Applied Materials & Interfaces, 2016. **8**(46): p. 31646-31652.
48. van Lare, C., et al., *Light Coupling and Trapping in Ultrathin Cu(In,Ga)Se_2 Solar Cells Using Dielectric Scattering Patterns.* ACS Nano, 2015. **9**(10): p. 9603-9613.
49. Yin, G., et al., *Enhanced performance of ultra-thin Cu(In,Ga)Se_2 solar cells deposited at low process temperature.* Solar Energy Materials and Solar Cells, 2015. **132**: p. 142-147.

50. Mughal, M.A., R. Engelken, and R. Sharma, *Progress in indium (III) sulfide (In_2S_3) buffer layer deposition techniques for CIS, CIGS, and CdTe-based thin film solar cells.* Solar Energy, 2015. **120**: p. 131-146.
51. Hwang, S., et al., *Wet Pretreatment-Induced Modification of Cu(In,Ga)Se_2/Cd-Free ZnTiO Buffer Interface.* ACS Applied Materials & Interfaces, 2018. **10**(24): p. 20920-20928.
52. Chantana, J., et al., *20% Efficient $Zn_{0.9}Mg_{0.1}O$:Al/$Zn_{0.8}Mg_{0.2}O$/Cu(In,Ga)$(S,Se)_2$ Solar Cell Prepared by All-Dry Process through a Combination of Heat-Light-Soaking and Light-Soaking Processes.* ACS Applied Materials & Interfaces, 2018. **10**(13): p. 11361-11368.
53. Gour, K.S., et al., *Cd-Free Zn(O,S) as Alternative Buffer Layer for Chalcogenide and Kesterite Based Thin Films Solar Cells: A Review.* Journal of Nanoscience & Nanotechnology, 2020. **20**(6): p. 3622-3635.
54. Powalla, M., et al., *Advances in Cost-Efficient Thin-Film Photovoltaics Based on Cu(In,Ga)Se_2.* Engineering, 2017. **3**(4): p. 445-451.
55. Kumar, A., et al., *Increased efficiency of 23% for CIGS solar cell by using ITO as front contact.* Materials Today: Proceedings, 2020. **28**: p. 361-365.
56. Minemoto, T. and J. Julayhi, *Buffer-less Cu(In,Ga)Se_2 solar cells by band offset control using novel transparent electrode.* Current Applied Physics, 2013. **13**(1): p. 103-106.
57. Kuwahata, Y. and T. Minemoto, *Impact of $Zn_{1-x}Mg_xO$:Al transparent electrode for buffer-less Cu(In, Ga)Se_2 solar cells.* Renewable Energy, 2014. **65**: p. 113-116.
58. Delahoy, A.E., et al., *New technologies for CIGS photovoltaics.* Solar Energy, 2004. **77**(6): p. 785-793.
59. Jäger, T., et al., *Hydrogenated indium oxide window layers for high-efficiency Cu(In,Ga)Se_2 solar cells.* Journal of Applied Physics, 2015. **117**(20): p. 205301.
60. Kramer, B., *Advances in Solid State Physics*. 2004: Springer Berlin Heidelberg.
61. Klein, A., *Energy band alignment in chalcogenide thin film solar cells from photoelectron spectroscopy.* Journal of Physics: Condensed Matter, 2015. **27**(13): p. 134201.
62. Walter, T., *Chapter Three - Reliability Issues of CIGS-Based Thin Film Solar Cells*, in *Semiconductors and Semimetals*, G.P. Willeke and E.R. Weber, Editors. 2015, Elsevier. p. 111-150.
63. Mansfield, L., *Manufacturing and Reliability Science of CIGS Photovoltaics.* Golden, CO: National Renewable Energy Laboratory, 2019(NREL/TP-5K00-72953).
64. Theelen, M. and F. Daume, *Stability of Cu(In,Ga)Se_2 solar cells: A literature review.* Solar Energy, 2016. **133**: p. 586-627.
65. M. M. Lunardi, J.P.A.-G., J. I. Bilbao and R. Corkish, *A Review of Recycling Processes for Photovoltaic Modules, Solar Panels and Photovoltaic Materials*, ed. B. Zaidi. 2018: IntechOpen.
66. Chowdhury, M.S., et al., *An overview of solar photovoltaic panels' end-of-life material recycling.* Energy Strategy Reviews, 2020. **27**: p. 100431.
67. Kemell, M., M. Ritala, and M. Leskelä, *Thin Film Deposition Methods for CuInSe_2 Solar Cells.* Critical Reviews in Solid State and Materials Sciences, 2005. **30**(1): p. 1-31.
68. Kapur, V.K., M. Fisher, and R. Roe, *Nanoparticle Oxides Precursor Inks for Thin film Copper Indium Gallium Selenide (CIGS) Solar Cells.* MRS Proceedings, 2011. **668**: p. H2.6.
69. Yang, R., et al., *Non-vacuum deposition methods for thin film solar cell: Review.* AIP Conference Proceedings, 2017. **1824**(1): p. 030018.
70. *NEXCIS Achieves a New Record Performance @ 17.3% Certified Pixel Measurement with its CIGS PV Technology*. 2014; Available from: www.nexcis.fr, accessed on February 2021.
71. Kaelin, M., D. Rudmann, and A.N. Tiwari, *Low cost processing of CIGS thin film solar cells.* Solar Energy, 2004. **77**(6): p. 749-756.

72. Brown, G., et al. *Device characteristics of a 17.1% efficient solar cell deposited by a non-vacuum printing method on flexible foil*. in *2012 38th IEEE Photovoltaic Specialists Conference*. 2012.

73. Zhang, T., et al., *High efficiency solution-processed thin-film* $Cu(In,Ga)(Se,S)_2$ *solar cells.* Energy & Environmental Science, 2016. **9**(12): p. 3674-3681.

74. Hibberd, C.J., et al., *Non-vacuum methods for formation of* $Cu(In,Ga)(Se,S)_2$ *thin film photovoltaic absorbers.* Progress in Photovoltaics: Research and Applications, 2010. **18**(6): p. 434-452.

75. Hillhouse, H.W. and M.C. Beard, *Solar cells from colloidal nanocrystals: Fundamentals, materials, devices, and economics.* Current Opinion in Colloid & Interface Science, 2009. **14**(4): p. 245-259.

76. Carey, G.H., et al., *Colloidal Quantum Dot Solar Cells.* Chemical Reviews, 2015. **115**(23): p. 12732-12763.

77. Azimi, H., Y. Hou, and C.J. Brabec, *Towards low-cost, environmentally friendly printed chalcopyrite and kesterite solar cells.* Energy & Environmental Science, 2014. **7**(6): p. 1829-1849.

78. Liu, Y. and D. Kong *Synthesis and characteristics of* $Cu(In,Ga)Se_2$ *thin films from nanoparticles by solvothermal method and selenisation process*. Micro & Nano Letters, 2012. **7**, 1112-1116.

79. Báez, Y.T.C., et al., *Hydrothermal synthesis of a photovoltaic material based on* $CuIn_{0.5}Ga_{0.5}Se_2$*.* Journal of Physics: Conference Series, 2017. **935**: p. 012004.

80. Latha, M., R. Aruna Devi, and S. Velumani, *Hot injection synthesis of* $Cu(In, Ga)Se_2$ *nanocrystals with tunable bandgap.* Optical Materials, 2018. **79**: p. 450-456.

81. Mubiayi, K.P., et al., *Colloidal synthesis of* $CuIn_{0.75}Ga_{0.25}Se_2$ *nanoparticles and their photovoltaic performance.* 2016. **14**(1): p. 420.

82. Guo, Q., et al., *Ink formulation and low-temperature incorporation of sodium to yield 12% efficient* $Cu(In,Ga)(S,Se)_2$ *solar cells from sulfide nanocrystal inks.* Progress in Photovoltaics: Research and Applications, 2013. **21**(1): p. 64-71.

83. Zarei, H. and R. Malekfar, *Quaternary* $Cu\ (In_xGa_{1-x})Se_2$ *Nanoparticles Synthesis Using Heating-up Method for Photovoltaic Applications.* International Journal of Optics and Photonics, 2018. **12**(1): p. 13-20.

84. Panthani, M.G., et al., *Synthesis of* $CuInS_2$*,* $CuInSe_2$*, and* $Cu(In_xGa_{1-x})Se_2$ *(CIGS) Nanocrystal "Inks" for Printable Photovoltaics.* Journal of the American Chemical Society, 2008. **130**(49): p. 16770-16777.

85. Latha, M., et al., *Solution based synthesis of* $Cu(In,Ga)Se_2$ *microcrystals and thin films.* RSC Advances, 2019. **9**(60): p. 35197-35208.

86. Latha, M., et al., *Synthesis of* $CuIn_{1-x}Ga_xSe_2$ *Nanoparticles by Thermal Decomposition Method with Tunable Ga Content.* Journal of Nanoscience and Nanotechnology, 2015. **15**(11): p. 8388-8394.

87. Sousa, V., et al., *Superstructural Ordering in Hexagonal* $CuInSe_2$ *Nanoparticles.* Chemistry of Materials, 2019. **31**(1): p. 260-267.

88. Kubo, J., et al., *Fabrication of* $Cu(In,Ga)Se_2$ *Films by a Combination of Mechanochemical Synthesis, Wet Bead Milling, and a Screen Printing/sintering Process.* MRS Proceedings, 2011. **1165**: p. 1165-M05-13.

89. Rohini, M., et al., *Parametric optimization of mechanochemical process for synthesis of* $Cu(In,Ga)_{0.5}Se_2$ *nanoparticles.* Materials Science in Semiconductor Processing, 2015. **37**: p. 151-158.

90. Cha, J.-H., S.J. Noh, and D.-Y. Jung, *Synthesis and Nanostructures of Metal Selenide Precursors for* $Cu(In,Ga)Se_2$ *Thin-Film Solar Cells.* ChemSusChem, 2015. **8**(14): p. 2407-2413.

91. Le, T.T.T., et al., *Green and low-cost synthesis of CIGSe nanoparticles using ethanol as a solvent by a sonochemical method - A new approach.* Materials Chemistry and Physics, 2018. **207**: p. 522-529.

92. McLeod, S.M., et al., *Synthesis and characterization of 15% efficient CIGSSe solar cells from nanoparticle inks.* Progress in Photovoltaics: Research and Applications, 2015. **23**(11): p. 1550-1556.

93. Le, T.T.T., et al., *Green and low-cost preparation of CIGSe thin film by a nanocrystals ink based spin-coating method.* Korean Journal of Chemical Engineering, 2019. **36**(12): p. 2110-2117.

94. Al Juhaiman, L., et al., *Green synthesis of tunable* $Cu(In_{1-x}Ga_x)Se_2$ *nanoparticles using non-organic solvents.* Green Chemistry, 2010. **12**(7): p. 1248-1252.

95. Stroyuk, O., et al., *"Green" Aqueous Synthesis and Advanced Spectral Characterization of Size-Selected* Cu_2ZnSnS_4 *Nanocrystal Inks.* Scientific Reports, 2018. **8**(1): p. 13677.

96. Abate, M.A., et al., *Aqueous synthesis of Mn-doped* $CuInSe_2$ *quantum dots to enhance the performance of quantum dot sensitized solar cells.* Dalton Transactions, 2019. **48**(42): p. 16115-16122.

97. Kapur, V.K., et al., *Non-vacuum processing of* $CuIn_{1-x}Ga_xSe_2$ *solar cells on rigid and flexible substrates using nanoparticle precursor inks.* Thin Solid Films, 2003. **431-432**: p. 53-57.

98. Wang, W., et al., *8.01%* $CuInGaSe_2$ *solar cells fabricated by air-stable low-cost inks.* Physical Chemistry Chemical Physics, 2012. **14**(31): p. 11154-11159.

99. Lu, C.-H., et al., *Solution-processed* $Cu(In,Ga)(Se,S)_2$ *solar cells prepared via a surface sulfurization process.* Journal of the Taiwan Institute of Chemical Engineers, 2020. **110**: p. 41-50.

100. Chandran, R., S.K. Panda, and A. Mallik, *A short review on the advancements in electroplating of* $CuInGaSe_2$ *thin films.* Materials for Renewable and Sustainable Energy, 2018. **7**(2): p. 6.

101. Yadav, B.S., et al., *Microstructural investigation of inkjet printed* $Cu(In,Ga)Se_2$ *thin film solar cell with improved efficiency.* Journal of Alloys and Compounds, 2020. **827**: p. 154295.

102. Qu, Y., G. Zoppi, and N.S. Beattie, *Selenization kinetics in* $Cu_2ZnSn(S,Se)_4$ *solar cells prepared from nanoparticle inks.* Solar Energy Materials and Solar Cells, 2016. **158**: p. 130-137.

103. Chen, S.-C., et al., *Crystalline Engineering Toward Large-Scale High-Efficiency Printable* $Cu(In,Ga)Se_2$ *Thin Film Solar Cells on Flexible Substrate by Femtosecond Laser Annealing Process.* ACS Applied Materials & Interfaces, 2017. **9**(16): p. 14006-14012.

104. Todorov, T. and D.B. Mitzi, *Direct Liquid Coating of Chalcopyrite Light-Absorbing Layers for Photovoltaic Devices.* European Journal of Inorganic Chemistry, 2010. **2010**(1): p. 17-28.

105. Todorov, T.K., et al., *Solution-processed* $Cu(In,Ga)(S,Se)_2$ *absorber yielding a 15.2% efficient solar cell.* Progress in Photovoltaics: Research and Applications, 2013. **21**(1): p. 82-87.

106. Eeles, A., et al., *High-Efficiency Nanoparticle Solution-Processed* $Cu(In,Ga)(S,Se)_2$ *Solar Cells.* IEEE Journal of Photovoltaics, 2018. **8**(1): p. 288-292.

107. Han, J.H., et al., *Actual partial pressure of Se vapor in a closed selenization system: quantitative estimation and impact on solution-processed chalcogenide thin-film solar cells.* Journal of Materials Chemistry A, 2016. **4**(17): p. 6319-6331.

108. Berner, U., et al., *13.3% efficient solution deposited* $Cu(In,Ga)Se_2$ *solar cells processed with different sodium salt sources.* Progress in Photovoltaics: Research and Applications, 2016. **24**(6): p. 749-759.

109. Lin, X., et al., *11.3% efficiency* $Cu(In,Ga)(S,Se)_2$ *thin film solar cells via drop-on-demand inkjet printing.* Energy & Environmental Science, 2016. **9**(6): p. 2037-2043.

110. Wang, W., Y.-W. Su, and C.-h. Chang, *Inkjet printed chalcopyrite* $CuIn_xGa_{1-x}Se_2$ *thin film solar cells.* Solar Energy Materials and Solar Cells, 2011. **95**(9): p. 2616-2620.

111. Septina, W., et al., $Cu(In,Ga)(S,Se)_2$ *Thin Film Solar Cell with 10.7% Conversion Efficiency Obtained by Selenization of the Na-Doped Spray-Pyrolyzed Sulfide Precursor Film.* ACS Applied Materials & Interfaces, 2015. **7**(12): p. 6472-6479.

112. Arnou, P., et al., *Solution processing of CuIn(S,Se)$_2$ and Cu(In,Ga)(S,Se)$_2$ thin film solar cells using metal chalcogenide precursors.* Thin Solid Films, 2017. **633**: p. 76-80.

113. Pulgarín-Agudelo, F.A., et al., *A thermal route to synthesize photovoltaic grade CuInSe$_2$ films from printed CuO/In$_2$O$_3$ nanoparticle-based inks under Se atmosphere.* Journal of Renewable and Sustainable Energy, 2013. **5**(5): p. 053140.

114. López-García, J., et al., *Synthesis of CuIn(S,Se)$_2$ quaternary alloys by screen printing and selenization-sulfurization sequential steps: Development of composition graded absorbers for low cost photovoltaic devices.* Materials Chemistry and Physics, 2015. **160**: p. 237-243.

115. Capello, C., U. Fischer, and K. Hungerbühler, *What is a green solvent? A comprehensive framework for the environmental assessment of solvents.* Green Chemistry, 2007. **9**(9): p. 927-934.

116. Byrne, F.P., et al., *Tools and techniques for solvent selection: green solvent selection guides.* Sustainable Chemical Processes, 2016. **4**(1): p. 7.

117. Badgujar, A.C., R.O. Dusane, and S.R. Dhage, *Pulsed laser annealing of spray casted Cu(In,Ga)Se$_2$ nanocrystal thin films for solar cell application.* Solar Energy, 2020. **199**: p. 47-54.

118. Badgujar, A.C., R.O. Dusane, and S.R. Dhage, *Cu(In,Ga)Se$_2$ thin film absorber layer by flash light post-treatment.* Vacuum, 2018. **153**: p. 191-194.

119. Dhage, S.R., M. Tak, and S.V. Joshi, *Fabrication of CIGS thin film absorber by laser treatment of pre-deposited nano-ink precursor layer.* Materials Letters, 2014. **134**: p. 302-305.

120. Chiou, C.-S. and H.-C. Penga, *Copper-indium-gallium-diselenide nanoparticles synthesized by a solvothermal method for solar cell application.* MATEC Web Conf., 2017. **108**: p. 14005.

121. Yadav, B.S., S.R. Dey, and S.R. Dhage, *Effective ink-jet printing of aqueous ink for Cu(In,Ga)Se$_2$ thin film absorber for solar cell application.* Solar Energy, 2019. **179**: p. 363-370.

122. Krebs, F.C., *Fabrication and processing of polymer solar cells: A review of printing and coating techniques.* Solar Energy Materials and Solar Cells, 2009. **93**(4): p. 394-412.

123. Burgelman, M., *Thin film solar cells by screen printing technology.* Proceedings of the Workshop Microtechnology and Thermal Problems in Electronics. 1998, The Summer School. Technical University of Lodz.

124. Wada, T., et al., *Fabrication of Cu(In,Ga)Se$_2$ thin films by a combination of mechanochemical and screen-printing/sintering processes.* Physica Status Solidi A, 2006. **203**(11): p. 2593-2597.

125. Kuo, H.-P., et al., *CIGS absorber preparation by non-vacuum particle-based screen printing and RTA densification.* Applied Energy, 2016. **164**: p. 1003-1011.

126. Faraj, M.G., K. Ibrahim, and A. Salhin, *Fabrication and characterization of thin-film Cu(In,Ga)Se$_2$ solar cells on a PET plastic substrate using screen printing.* Materials Science in Semiconductor Processing, 2012. **15**(2): p. 165-173.

127. Faraj, M.G., K. Ibrahim, and A. Salhin, *Effects of Ga concentration on structural and electrical properties of screen printed-CIGS absorber layers on polyethylene terephthalate.* Materials Science in Semiconductor Processing, 2012. **15**(2): p. 206-213.

128. Wang, Y.-F., et al., *Fully Printed PEDOT:PSS-based Temperature Sensor with High Humidity Stability for Wireless Healthcare Monitoring.* Scientific Reports, 2020. **10**(1): p. 2467.

129. Bandodkar, A.J., et al., *Highly Stretchable Fully-Printed CNT-Based Electrochemical Sensors and Biofuel Cells: Combining Intrinsic and Design-Induced Stretchability.* Nano Letters, 2016. **16**(1): p. 721-727.

130. Cai, L., et al., *Fully Printed Stretchable Thin-Film Transistors and Integrated Logic Circuits.* ACS Nano, 2016. **10**(12): p. 11459-11468.

131. Bade, S.G.R., et al., *Fully Printed Halide Perovskite Light-Emitting Diodes with Silver Nanowire Electrodes.* ACS Nano, 2016. **10**(2): p. 1795-1801.

132. Eggenhuisen, T.M., et al., *High efficiency, fully inkjet printed organic solar cells with freedom of design.* Journal of Materials Chemistry A, 2015. **3**(14): p. 7255-7262.
133. Gheno, A., et al., *Toward Highly Efficient Inkjet-Printed Perovskite Solar Cells Fully Processed Under Ambient Conditions and at Low Temperature.* Solar RRL, 2018. **2**(11): p. 1800191.
134. Corzo, D., et al., *Digital Inkjet Printing of High-Efficiency Large-Area Nonfullerene Organic Solar Cells.* Advanced Materials Technologies, 2019. **4**(7): p. 1900040.
135. Tregnago, G., *Printing organic photovoltaics.* Nature Energy, 2018. **3**(7): p. 537-537.
136. Dehghani, M., et al., *Totally solution-processed $CuInS_2$ solar cells based on chloride inks: reduced metastable phases and improved current density.* Journal of Physics D: Applied Physics, 2015. **48**(11): p. 115304.
137. Cheshme khavar, A.H., et al., *Fabrication of selenization-free superstrate-type $CuInS_2$ solar cells based on all-spin-coated layers.* Materials Chemistry and Physics, 2017. **186**: p. 446-455.
138. Cheshme Khavar, A.H., A.R. Mahjoub, and N. Taghavinia, *Low-temperature solution-based processing to 7.24% efficient superstrate $CuInS_2$ solar cells.* Solar Energy, 2017. **157**: p. 581-586.
139. Nagino, S., H. Suzuki, and S. Ueno. *Substrate-type $Cu(In,Ga)Se_2$ solar cells with all layers deposited by non-vacuum solution-based methods*. in *2013 IEEE 39th Photovoltaic Specialists Conference*. 2013. Tampa, FL, USA.
140. Singh, M., et al., *Thin-Film Copper Indium Gallium Selenide Solar Cell Based on Low-Temperature All-Printing Process.* ACS Applied Materials & Interfaces, 2014. **6**(18): p. 16297-16303.
141. Kovalenko, A., Hrabal, M., *Printable Solar Cells*, in *Printable Solar Cells*, N.D. Sankir, Sankir, M. , Editor. 2017. p. 163-202.
142. Jackson, P., et al., *Effects of heavy alkali elements in $Cu(In,Ga)Se_2$ solar cells with efficiencies up to 22.6%.* Physica Status Solidi – Rapid Research Letters, 2016. **10**(8): p. 583-586.
143. Wang, M. and K.-L. Choy, *All-Nonvacuum-Processed CIGS Solar Cells Using Scalable Ag NWs/AZO-Based Transparent Electrodes.* ACS Applied Materials & Interfaces, 2016. **8**(26): p. 16640-16648.
144. Contreras, M.A., et al., *Replacement of Transparent Conductive Oxides by Single-Wall Carbon Nanotubes in $Cu(In,Ga)Se_2$-Based Solar Cells.* The Journal of Physical Chemistry C, 2007. **111**(38): p. 14045-14048.
145. Kim, A., et al., *All-Solution-Processed Indium-Free Transparent Composite Electrodes based on Ag Nanowire and Metal Oxide for Thin-Film Solar Cells.* Advanced Functional Materials, 2014. **24**(17): p. 2462-2471.
146. Xiao-Hui Tan, Y.C., and Ye-Xiang Liu, *Silver nanowire composite thin films as transparent electrodes for $Cu(In,Ga)Se_2/ZnS$ thin film solar cells.* Applied Optics, 2014. **53**(15): p. 3273-3277.
147. Shin, D., et al., *Solution-Processed Ag Nanowires + PEDOT:PSS Hybrid Electrode for $Cu(In,Ga)Se_2$ Thin-Film Solar Cells.* ACS Applied Materials & Interfaces, 2015. **7**(24): p. 13557-13563.
148. Singh, M., P. Prasher, and J. Kim, *Solution processed silver-nanowire/zinc oxide based transparent conductive electrode for efficient photovoltaic performance.* Nano-Structures & Nano-Objects, 2018. **16**: p. 151-155.

Section I

Conventional methodologies for solution-processed CIGSe photovoltaic systems

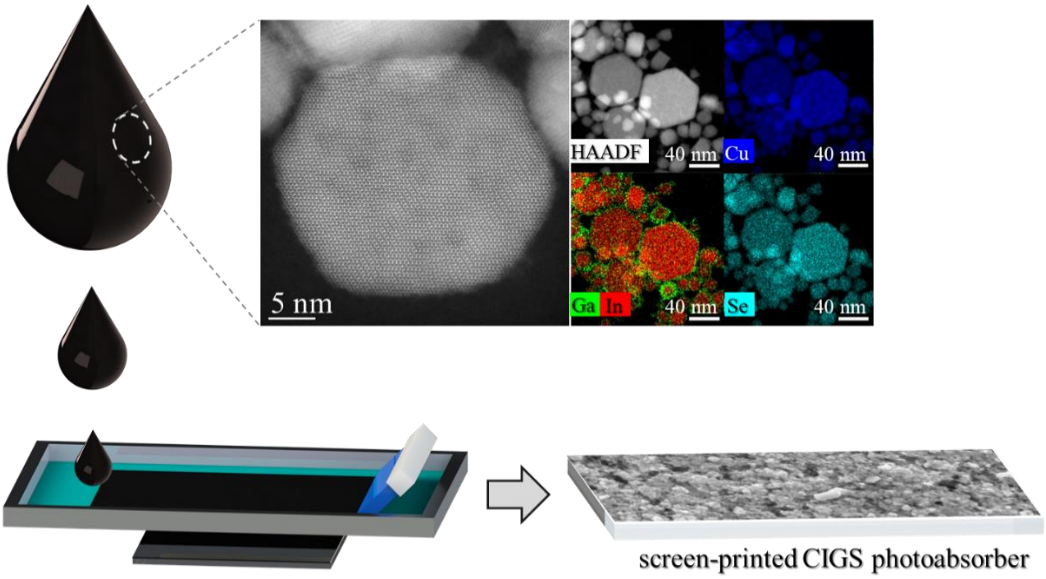

Chapter 2. Large-scale synthesis of semiconducting Cu(In,Ga)Se$_2$ nanoparticles for screen printing application

Thin film deposition through solution processing is gaining increasing attention from the industry, due to the potential low cost and high throughput production. To this end, the elimination of the selenization procedure in the synthesis of $\mathrm{Cu(In,Ga)Se_2}$ nanoparticles with following dispersion into ink formulations for printing/coating deposition processes are of high relevance. However, most of the reported syntheses procedures give access to tetragonal chalcopyrite $\mathrm{Cu(In,Ga)Se_2}$ nanoparticles, whereas methods to obtain other structures are scarce. To this end, this chapter presents a large-scale synthesis of high-quality $\mathrm{Cu(In,Ga)Se_2}$ nanoparticles with wurtzite hexagonal structure, wide absorption in visible to near-infrared regions, and [Cu] / [In + Ga] ≈ 0.8 and [Ga] / [Ga + In] ≈ 0.3 metal ratios. Moreover, the inclusion of the synthesized NPs into a water-based ink formulation for screen printing deposition has been addressed, resulting in thin films with homogenous thickness of ≈4.5 μm, paving the way towards environmentally friendly roll-to-roll production of photovoltaic systems.

This chapter is based on the following publication: **B. F. Gonçalves**, A. P. LaGrow, S. Pyrlin, B. Owens-Baird, G. Botelho, L. S. A. Marques, M. M. D. Ramos, K. Kovnir, S. Lanceros-Méndez and Y. V. Kolen'ko, *Large-Scale Synthesis of Semiconducting Cu(In,Ga)Se$_2$ Nanoparticles for Screen Printing Application*; Nanomaterials, 11(5), 1148, 2021.

2.1 Introduction

Solution-processed CIGSe PVs give access to semi-transparent, lightweight, and flexible PV devices [1], opening widely their range of application from windows [2] to space exploration [3]. Moreover, solution processing methodologies are compatible with roll-to-roll production of PV devices, rendering solution processing more sustainable and cost-efficient than vacuum deposition methodologies [4]. Nevertheless, the employment of a selenization step during the fabrication of the CIGSe PV is a shortcoming due to the potential risk it carries through the high toxicity of the evolved selenium species, i.e. Se vapor and $\mathrm{H_2Se}$ gas.

To overcome this shortcoming, fabrication of the CIGSe PVs directly from CIGSe NPs would eliminate the need for the selenization step, thus lowering the environmental impact of the PV cell production. In this context, the synthesis of CIGSe NPs has attracted considerable interest, and reports based on hot-injection [5, 6], heat-up [7, 8], solvothermal [9, 10], hydrothermal [11, 12], or mechanochemical [13, 14] methods have appeared, usually delivering crystalline and phase-pure CIGSe NPs [15]. Notably, most of the synthesis protocols, regardless of the method employed [16, 17], are severely limited to the preparation of CIGSe NPs with common tetragonal chalcopyrite-type structure (space group $I\bar{4}2d$), the most thermodynamically stable phase at room temperature [16, 17]. There are only few reports on the synthesis of CISe NPs with uncommon hexagonal wurtzite-type structure (space group $P6_3mc$) [16, 18-21], mostly due to the challenging control over stoichiometry and crystal structure [22]. Notably, only one synthesis strategy has given access to quaternary CIGSe NPs [23]. Most likely, this could be associated with the addition of Ga into the system which significantly slows the nucleation and growth kinetics of the NPs, turning difficult its incorporation into CISe [22]. On the other hand, the presence of Ga in the CIGSe photoabsorber is essential, since the stoichiometry [Cu] / [In + Ga] = 0.8-0.9 and [Ga] / [In + Ga] = 0.3 leads to highly efficient PV cells [24, 25].

The herein presented work covers a synthesis methodology towards the preparation of quaternary CIGSe NPs with uncommon wurtzite-type structure, along with upscaling of the procedure to 5 g scale. The experimental and theoretical results on Ga incorporation into the Cu–In–Se system are discussed, while the thermal stability of the resultant NPs is investigated by *in-situ* powder X-ray diffraction and *in situ* electron microscopy. Furthermore, the formulation of an environmentally friendly ink comprising the synthesized CIGSe NPs for screen printing deposition of phase-pure semiconducting thin films is also addressed.

2.2 Experimental

2.2.1 Chemicals

Tetrakis(acetonitrile)copper(I) tetrafluoroborate (TACT, 98%, TCI), indium(III) acetate ($\mathrm{In(ac)_3}$, 99.99%, Sigma-Aldrich), gallium(III) acetylacetonate ($\mathrm{Ga(acac)_3}$, 99.99%, Sigma-Aldrich), hexadecylamine (HDA, 95%, TCI, melting point 44 °C, boiling point 330 °C), diphenyl diselenide ($\mathrm{Ph_2Se_2}$), 97%, TCI), acetonitrile (ACN, 99.9%, Fisher Scientific), ethylenediamine (EDA, ≥99%, Sigma-Aldrich), dichloromethane (DCM, ≥99.8%, Fisher Scientific), hydroxypropyl methyl cellulose polymer (HPMC, 2% aqueous solution, viscosity 80–120 cP, Sigma-Aldrich), toluene (≥99.5%, Sigma-Aldrich), ethanol (≥99.8%, Honeywell), acetone (≥99.5%, Honeywell), and isopropanol (IPA, ≥99.8%, Honeywell) were used as received. Ultrapure water (18.2 MΩ cm) was generated using Milli-Q (MQ) Advantage A10 system (Millipore).

2.2.2 Synthesis

The synthesis was carried out using standard Schlenk line conditions. Initially, the reaction with the following metal ratio [Cu] / [In + Ga] = 0.83 and [Ga] / [In + Ga] = 0.3 was used. For this purpose, TACT (12.40 mmol), $\mathrm{In(ac)_3}$ (10.8 mmol), $\mathrm{Ga(acac)_3}$ (4.1 mmol), $\mathrm{Ph_2Se_2}$ (20.2 mmol), and HDA (414.10 mmol) were charged into a 500 mL three-neck round-bottom flask. The flask was connected to a condenser and equipped with a magnetic stirrer, thermocouple, and vacuum adapter. After attaching the flask to a Schlenk line under Ar, the system was slowly heated to 90 °C and the precursors dissolved in melted HDA under stirring. After complete dissolution, as observed by the emergence of a clear green solution, the reaction was degassed under vacuum for 30 min to remove undesired low boiling point liquids, as possible water and acetic acid admixtures. The reaction mixture was placed under Ar and the system was rapidly heated to 300 °C and stirred at this temperature for 1 h. As the reaction proceeds, the formation of a brown-black slurry was observed. The slurry was cooled to 70 °C and diluted with 100 mL of toluene, followed by cooling to RT. Notably, it is important to conduct the dilution at 70 °C, since HDA is solid at RT, and therefore, it will be difficult to isolate the product without dilution. Next, the resultant NPs were precipitated by a mixture of toluene/ethanol (3:1), washed with the same solvent, and collected by centrifugation (9000 rpm, 5 min). The washing procedure was repeated three times in total. Finally, the NPs were dried under vacuum overnight and homogenized using an agate mortar, thus affording ~5 g of the product as powder (**Sample I**).

Similarly, **Sample II** was synthesized by modifying the initial concentrations of the metal precursors to give access to CIGSe NPs with the desired metal ratio. Specifically, TACT (8.20 mmol), $\mathrm{In(ac)_3}$ (6.43 mmol), $\mathrm{Ga(acac)_3}$ (2.65 mmol) and same amount of $\mathrm{Ph_2Se_2}$ and HDA as used in the previous synthesis, were used during the synthesis, thus affording ca. 4 g of **Sample II**.

2.2.3 Ink formulation

For ink formulation purposes, a ligand exchange procedure was employed to replace HDA, since is solid at RT. To this end, 120 mL of ACN, 1 mL of EDA, and 15 mL of DCM were loaded into a flask and stirred magnetically at RT [26]. After a few minutes, 3 g of the synthesized NPs were added, and the solution was stirred at RT for 24 h. The NPs were then collected by centrifugation (9000 rpm, 10 min) and dried under vacuum. The resultant powder was subjected to wet ball milling (WBM) to eliminate possible agglomerates and improve the dispersion of the synthesized NPs in the ink. To this end, a dispersion of 3 g of NPs in 5 mL of IPA was ball-milled for 24 h using a KD-6808 rotary polishing machine (Guangzhou) with bidirectional rotation and YSZ balls with two sizes of 0.2 mm and 10 mm (mass ratio 50:50). Finally, the resultant suspension was filtered using a 1 μm syringe filter to homogenize the NP size and dried at 80 °C. The resultant powder was ground in a mortar and preserved.

Then the water-based ink was formulated in a 10 mL glass vial. HPMC (45 mg) was first dissolved in a mixture of water (0.33 mL) and ethanol (0.66 mL) by magnetic stirring at 4 h at RT. Then, the NP powder (0.60 g) was added to the resulting viscous 5% HPMC solution and kept under stirring for 12 h, resulting in a homogenous water-based ink with 40% of NPs content.

2.2.4 Screen printing

For printing, 2.6×2.6 $\mathrm{cm^2}$ SLG substrates (Fisher Scientific) with 1 mm of thickness were consecutively cleaned in acetone, IPA, and water using ultrasonication (ElmasonicP30H) at 60 °C for 20 min each. The substrates were then rinsed with ethanol, dried under $\mathrm{N_2}$ flow, and subjected to $\mathrm{O_2}$ plasma treatment (Harrick Plasma) during 10 min for a complete surface cleaning.

Square patterns of 2.5×2.5 $\mathrm{cm^2}$ were printed above the previously cleaned SLG substrates using a semi-automatic screen printer (DX-3050D, DSTAR) equipped with a vacuum stage to hold the substrate. Thin films were screen printed using 180 $\mathrm{threads\ cm^{-1}}$ count with thread diameter of 27 μm and mesh opening of 24 μm. Three-step printing was employed followed by immediate drying at 90 °C for 3 minutes to evaporate the solvent, followed by annealing to eliminate organic matter inside a quartz tubular furnace

(Termolab) using 100 sccm of Ar at 500 °C with a heating rate of 50 °C min during 50 min in total. Above the same thin film, an additional two-step printing was employed to fill the voids left by the previous printing, followed by the described thermal treatments. The printing process was performed using an 85-shore squeegee at 0.3 $\mathrm{m\,s^{-1}}$ of velocity with a 75° deflection angle and a distance between the mesh and the substrate of 5 mm.

2.2.5 Characterization

X-ray diffraction (XRD):

The phase composition of the NPs was evaluated on an X'Pert PRO diffractometer (PANalytical) set at 45 kV and 40 mA, equipped with a Ni-filtered Cu Kα radiation and PIXcel detector. XRD data were collected using Bragg–Brentano geometry in a 2θ range from 15° to 80° with a scan speed of 0.01° $\mathrm{s^{-1}}$. The XRD patterns were matched to the International Centre for Diffraction Data (ICDD) PDF-4 database using HighScore software package (PANalytical).

The average crystallite size was estimated in HighScore software using the Scherrer equation: $D = \frac{K\lambda}{\beta cos\theta}$, where D is the crystallite size, K is the Scherrer constant (0.89), λ is the X-ray wavelength, β is the width of the peak (full width at half the maximum (FWHM) in radians), and θ is the Bragg angle.

Variable temperature *in-situ* synchrotron powder XRD:

Variable temperature *in-situ* powder XRD data was collected at the synchrotron beamline 17-BM at the Advanced Photon Source, Argonne National Laboratory. Wurtzite CISe sample was loaded into 0.5/0.7 mm inner/outer diameter silica capillaries and sealed under vacuum. The sealed silica capillaries were placed into a secondary shield capillary, with a thermocouple set as close as possible to the measurement area. Details for experimental set-up are provide in [27]. The data were collected with λ = 0.24141 Å at variable temperatures.

Raman spectroscopy:

To inspect the local structure of the CIGSe photoabsorber layer, Raman spectroscopy measurements were performed on an alpha300 R confocal Raman microscope (WITec) using a 532 nm Nd:YAG laser for excitation. The laser beam with power of 0.9 mW was focused on the specimen with a ×50 lens (Zeiss). Afterwards, Raman spectra were collected using 1800 groove $\mathrm{mm^{-1}}$ grating with 100 acquisitions and 1.5 s of acquisition time.

Electron microscopy:

The evaluation of the surface and cross-sectional morphologies of the printed thin films as well as the chemical composition of the NP powders were performed by SEM using a Quanta 650 FEG ESEM microscope (FEI) equipped with energy-dispersive X-ray spectroscopy (EDX). To investigate fine microstructure and the chemical composition of the synthesized NPs, high-angle annular dark-field scanning transmission electron microscopy (HAADF–STEM), selected area electron diffraction (SAED), and energy-dispersive X-ray spectroscopy in STEM mode (STEM–EDX) were performed using a Titan Themis Titan Themis 60-300 (FEI co.) equipped with an X-FEG gun, superX EDX configuration with four detector system, an image corrector, and probe corrector, operating at 200 kV.

The *in-situ* heating studies were carried out on the Titan Themis (FEI co.) transmission electron microscopy (TEM) with the NanoEx i/v heating holder, with microelectromechanical systems (MEMS) chips.

Optical properties:

The optical band gap measurements on the as-synthesized NP powders were performed using UV–Vis–NIR spectroscopy. The resulting data were collected at RT using a LAMBDA 950 UV/Vis/NIR spectrophotometer (PerkinElmer) equipped with a 60 mm integrating sphere and InGaAs detector. Band gap values were determined from the product of Planck's constant with speed of light and absorption cutoff wavelength on the absorption spectra edge [28].

Surface tension and rheological properties:

The surface tension of the ink was measured by a drop-shape analysis–contact angle (DSA–CA) method (KRÜSS) with DSA3 software package, using a drop volume of 10 μL and a needle with 0.9 mm of diameter, at RT. The results are presented together with the standard deviation for ten measurements. The RT dynamic viscosity measurements were performed on a MCR 300 modular compact rheometer (Physica) using a shear rate range of 0–500 s^{-1}.

Thermogravimetric analysis (TGA):

The thermal behavior of the synthesized CIGSe NPs was obtained with a TGA/DSC 1 STARe system (Mettler Toledo) under Ar flow with a heating ramp of 10 $°C\ min^{-1}$.

In silico study:

Density Functional Theory (DFT) calculations of segregation energy where conducted using VASP DFT package for high accuracy [29]. For simulations of the effect of passivating ligands another DFT package – SIESTA [30] - was used as a trade of between accuracy and computational efficiency for molecular systems. A 128-atom 2x2x2 supercell of a hexagonal CISe lattice was used both for bulk and surface calculations with 1.4 nm of vacuum layer added in the latter case. Reciprocal space was sampled using 2x2x2 Monkhorst-Pack grid. In both cases Perdew-Burke-Ernzerhof generalized gradient approximation [31] was used for exchange and correlation functional during the geometry relaxation and the total energies and forces were converged down to 10^{-4} eV and 0.05 $\mathrm{eV\ Ang^{-1}}$ per atom. Energy cutoffs of 520 eV and 800 Ry were used correspondingly for VASP and SIESTA calculations. Scalar-relativistic PSML [32] pseudopotentials were used for the latter. To establish the preferred atomic arrangement on the slab surface where the candidate structures had different atomic composition (Cu- or In-rich), formation enthalpy difference for super-cells with different atomic composition was computed as $\Delta H_{form} = \Delta E_{DFT} - \sum \Delta n_i \mu_i$, where the first term is the total energy difference between candidate structures per super-cell and $\mu_i = E_{i,bulk}/N_{i,bulk}$ – chemical potential of element *i* (Cu or In), estimated from the energy per atom of a corresponding single element crystal.

2.3 Results

2.3.1 Syntheses

The herein presented work was based on a previous study over the synthesis of CISe NPs [20] with excellent crystallinity and phase-pure hexagonal wurtzite structure. In this study, the scope of the synthesis is extended to CIGSe NPs by investigating their applicability for screen printing deposition, which is relevant for roll-to-roll production of PVs. The large-scale synthesis was conducted by reacting $\mathrm{Cu^{+}}$, $\mathrm{In^{3+}}$, and $\mathrm{Ga^{3+}}$ precursors with $\mathrm{Ph_2Se_2}$ in HDA working both as solvent, due to its high boiling point, and as capping agent. First, a synthesis with [Cu] / [In + Ga] = 0.83 and [Ga] / [In + Ga] = 0.3 nominal stoichiometry of the metal precursors was conducted, however, the resultant NPs metal ratio was different from the nominal (**Sample I**) (*vide infra*). Therefore, the ratio of the starting materials was readjusted, which resulted in NPs with the targeted composition (**Sample II**). The conducted syntheses delivered ~4.5 g (~90% yield) and ~3.5 g (~70% yield) of CIGSe NPs for **Samples I** and **II**, respectively.

The XRD phase composition analysis of the resulting NPs from both syntheses (Figure 2.1a) revealed major peaks corresponding to (100), (002), (101), (102), and (110) reflections of wurtzite with relative intensities and positions matching well with the reported characteristic peaks of wurtzite CISe [33]. Notably, no signs of chalcopyrite phase or any secondary phases were found, revealing phase-pure CIGSe NPs with rare wurtzite-type hexagonal structure (space group $P6_3mc$). The Raman data (Figure 2.1b) revealed a sharp peak at around 178 cm^{-1} for **Sample I**, corresponding to the A_1 vibrational mode of CISe [20]. On the other hand, the spectrum of **Sample II** confirmed the presence of phase-pure CIGSe NPs, showing a sharp peak at around 174 cm^{-1}, corresponding to A_1 vibrational mode of CIGSe and two broad bands at 127 cm^{-1} and 211 cm^{-1} corresponding to the B_1 and B_2/E modes, respectively [34, 35]. Importantly, both spectra were found to be free of $\mathrm{CuSe_2}$ secondary phase, which usually emerges as an additional Raman peak at 260 cm^{-1} and is known to be a detrimental phase for PVs by functioning as a recombination center for charge carriers through the photoabsorber. The chemical composition of both NP samples was studied by SEM–EDX (Figure 2.2), which revealed a nominal metal ratio of $\mathrm{Cu_{1.13}(In_{1.42}Ga_{0.10})Se_2}$ for **Sample I** and the successful readjustment for **Sample II** to $\mathrm{Cu_{0.89}(In_{0.72}Ga_{0.28})Se_2}$, well matching with the targeted composition [Cu]/[In + Ga] ≈ 0.8 and [Ga]/[Ga + In] ≈ 0.3. The crystallite size of NPs from **Sample II** was estimated using Scherrer formula, revealing an average of 29 ± 8 nm.

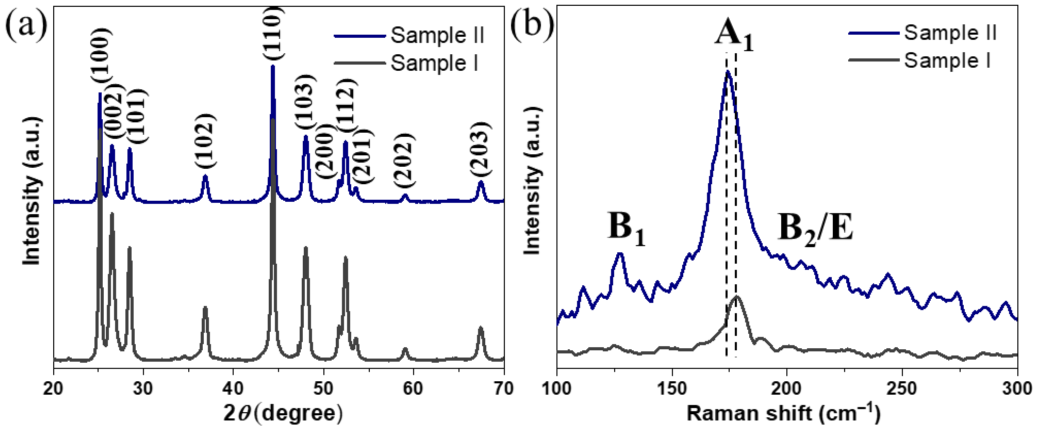

Figure 2.1. XRD diffractogram (*hkl* peak assignment is based on ICDD card no. 01-078-5190 for wurtzite) (a) and Raman data (b) of the synthesized NPs from both samples.

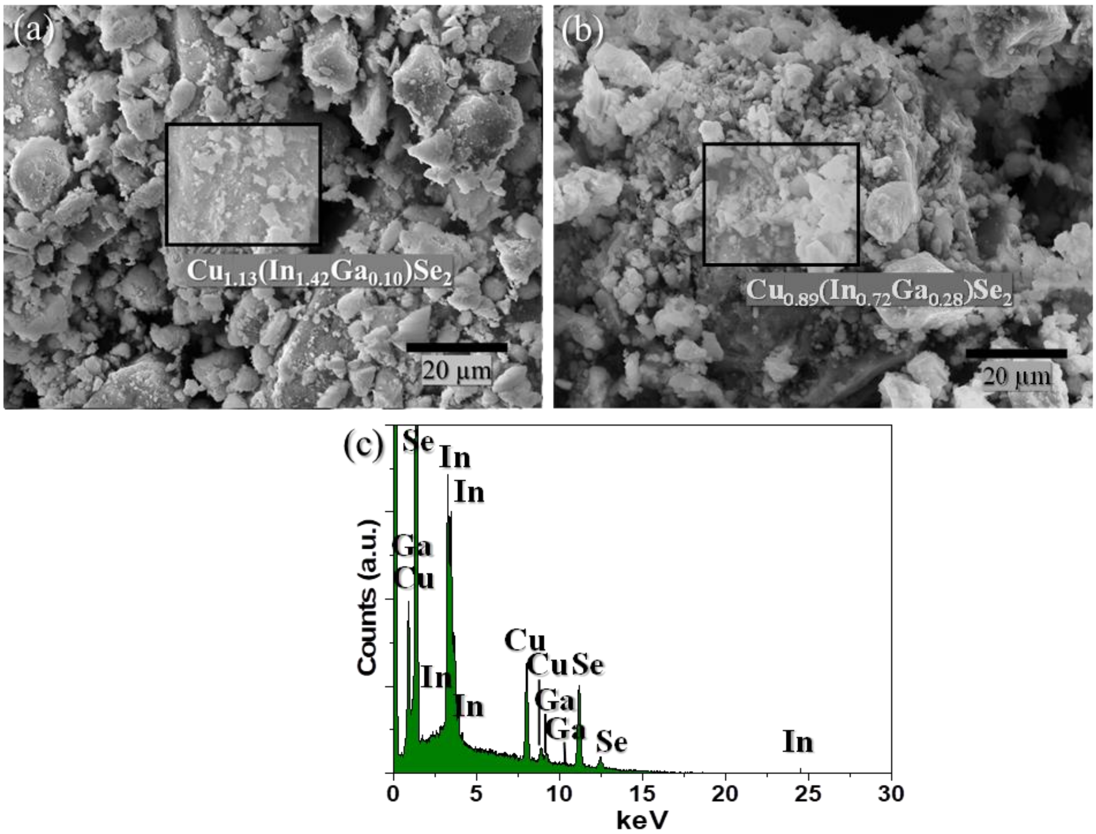

Figure 2.2. SEM images of Sample I (a) and Sample II (b), and EDX spectrum of Sample II (c).

The HAADF–STEM images with STEM–EDX mapping (Figure 2.3) of **Sample I** confirmed the presence of hexagonal plates with 10–80 nm of size. Interestingly, although the maps revealed a uniform distribution of Cu, In, and Se metals, Ga seemed to be segregated at the surface of the NPs. The observed Ga segregation and the Raman spectrum from **Sample I** has driven to the assumption of the existence of CISe + Ga mixed phases in the NPs from this sample.

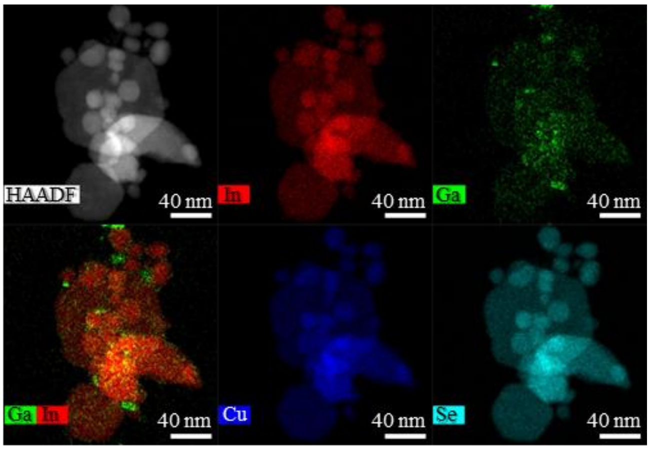

Figure 2.3. HAADF–STEM image and corresponding STEM–EDX elemental maps of Sample I.

On the other hand, hexagonal plates with a size of 10–70 nm are observed in the HAADF–STEM images of **Sample II** along the (001) zone axis (Figure 2.4a). Moreover, the fast Fourier transformer (FFT) patterns (Figure 2.4b) confirm the hexagonal wurtzite phase of the NPs with superstructural ordering with twin planes in the superstructure ordering shown by the streaking in the FFT (Figure 2.4b) and by the red arrows and dashed lines (Figure 2.4c). In the STEM–EDX maps (Figure 2.4d), a more uniform distribution of all metals is detected as compared to **Sample I**, with Ga located not only on the surface but also inside the NPs, revealing pure-phase CIGSe with hexagonal wurtzite structure. Therefore, **Sample II** was selected to move forward with this study.

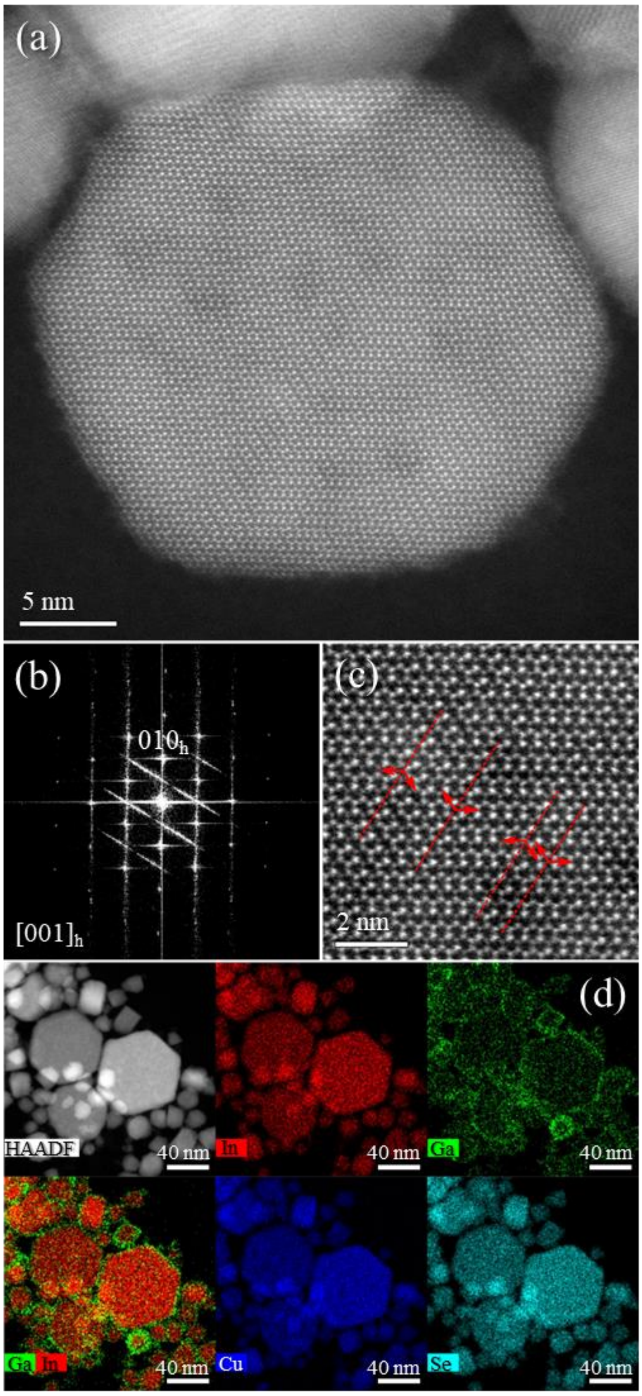

Figure 2.4. HAADF–STEM images (a, c), FFT pattern (b) and STEM–EDX maps (d) of Sample II.

The deposition of a photoabsorber layer requires an annealing treatment to remove organic matter from the HDA stabilizer, which would hamper the performance of the PV device due to creation of recombination centers for charge carriers. Thus, the thermal stability of the synthesized NPs was evaluated by TGA (Figure 2.5), which revealed that at 500 °C all organic matter is degraded, with a weight loss of ~14.5%, leading to the selection of this temperature for the annealing.

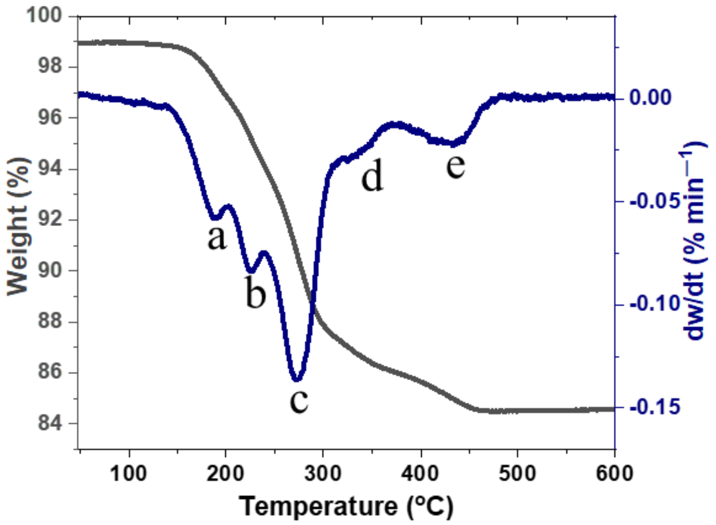

Figure 2.5. Thermogravimetric analysis with the corresponding derivative curve for the NPs from Sample II under Ar. Peak temperatures a: 187 °C, b: 226 °C, c: 273 °C, d: 337 °C, and e: 433 °C.

Interestingly, the previously reported synthesis [20] revealed that the synthesized CISe NPs tend to have superstructural ordering. Wurtzite is considered a metastable phase of CISe that is difficult to stabilize in comparison to the thermodynamically stable chalcopyrite CISe. Thus, prior to annealing the wurtzite films, thermal stability studies were performed on the CISe NPs by *in-situ* XRD (Figure 2.6), where the wurtzite phase was found to be stable up to 400 °C. At higher temperatures, wurtzite CISe started to transform into the thermodynamically stable chalcopyrite phase. No further changes were observed in 480–540 °C range. Due the similarities between the CISe and CIGSe NPs, a similar thermal behavior is assumed for the herein synthesized CIGSe NPs.

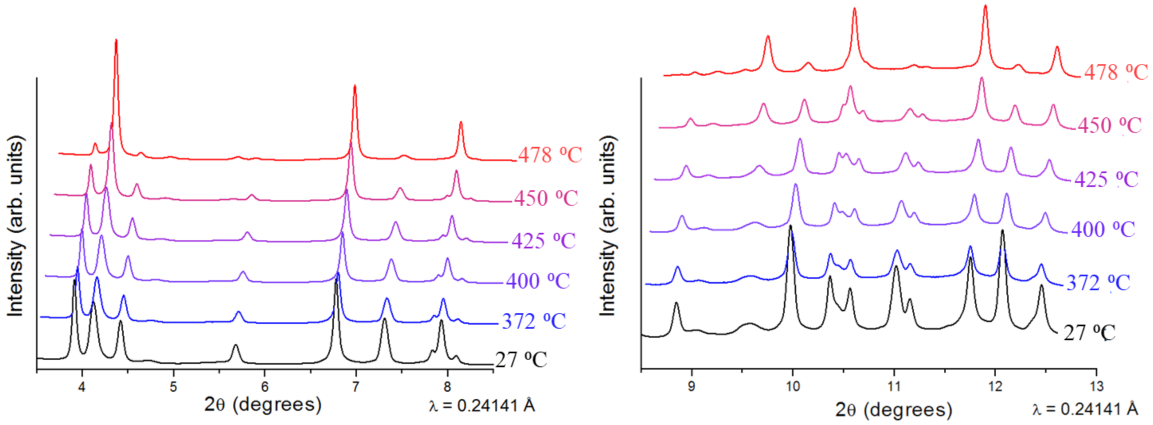

Figure 2.6. In-situ variable temperature synchrotron powder XRD of wurtzite CISe NCs sample (λ = 0.24141 Å). The sample was heated from RT (bottom pattern) to 478 °C (top pattern).

To complete the thermal stability studies, *in-situ* TEM imaging was performed under vacuum on the synthesized CIGSe NPs (Figure 2.7). Similar to previously reported CISe NPs, the as-synthesized CIGSe NPs present hexagonal wurtzite-type structure ($P6_3mc$ subcell) with superstructural ordering. The NPs were heated rapidly to 450 °C over the course of ~ 10 minutes and then left at 450 °C. The conducted experiment revealed no changes in the crystal lattice bellow 450 °C, however, after $\sim$25 min at 450 °C, the supercell lattices of the wurtzite phase disappeared, as indicated by the calculated FFT patterns.

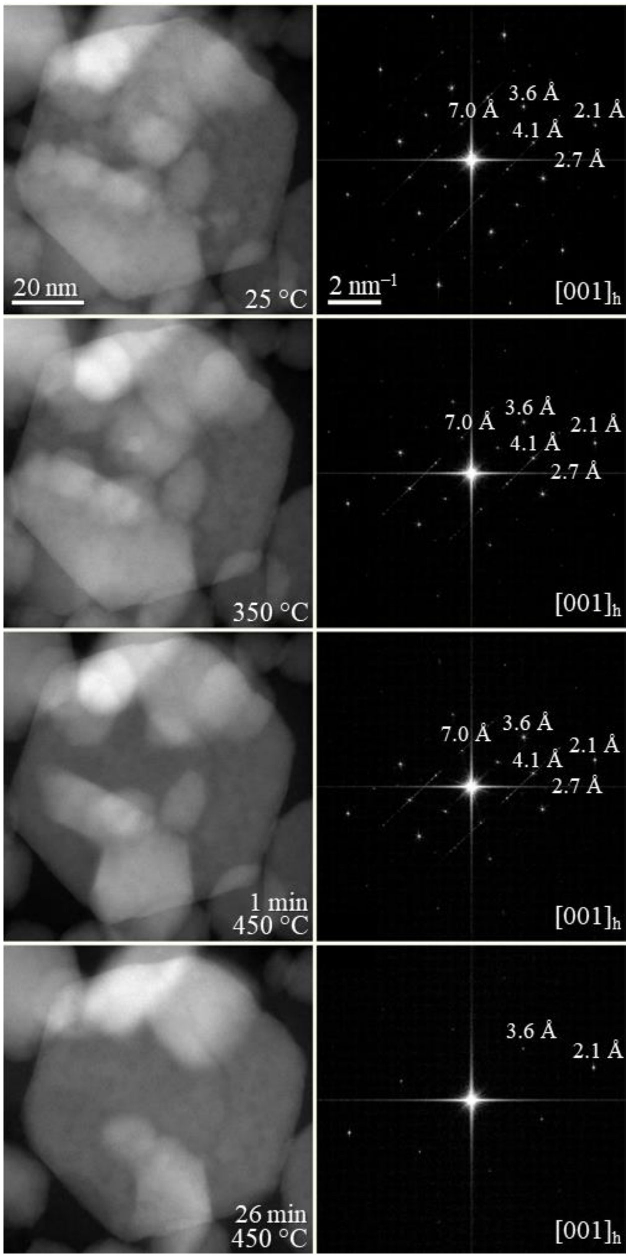

Figure 2.7. From top to bottom: *In situ* TEM imaging under vacuum of the synthesized CIGSe NPs at RT, at 350 °C, and at 450 °C during 1 and 26 min, along with the corresponding FFT patterns.

2.3.2 Screen-printed film

With such high-quality NPs in hand, the study proceeded for the development of a water-based ink for the screen-printed thin film to be employed as photoabsorber layer. To this end, a ligand exchange procedure was successfully employed, as detected by the NPs TGA curve (Figure 2.8), to replace HDA, which is a solid at RT, by EDA. The optical band gap of the NPs after ligand exchange was evaluated through the absorption spectrum resulting from UV–Vis–NIR measurements (Figure 2.9), which revealed a strong absorption of light from the entire visible to the near-infrared regions. Notably, no significant differences on the optical properties were found between the HDA and EDA-capped NPs. The band gap of EDA-capped NPs (E_g) was determined to be 0.95 ± 0.02 eV, which is in good agreement with reported bandgaps for wurtzite CISe NPs [20].

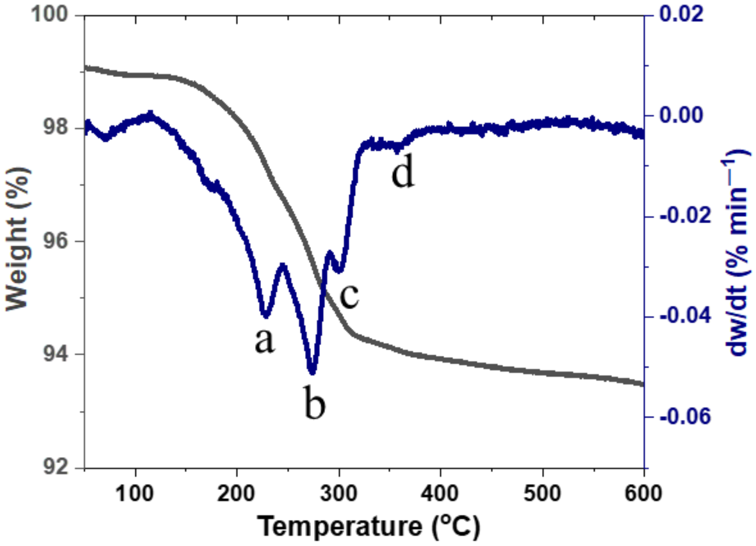

Figure 2.8. Thermogravimetric analysis with the corresponding derivative for the NPs from Sample II after ligand exchange under Ar. Peak temperatures a: 227 °C, b: 274 °C, c: 299 °C, and d: 357 °C.

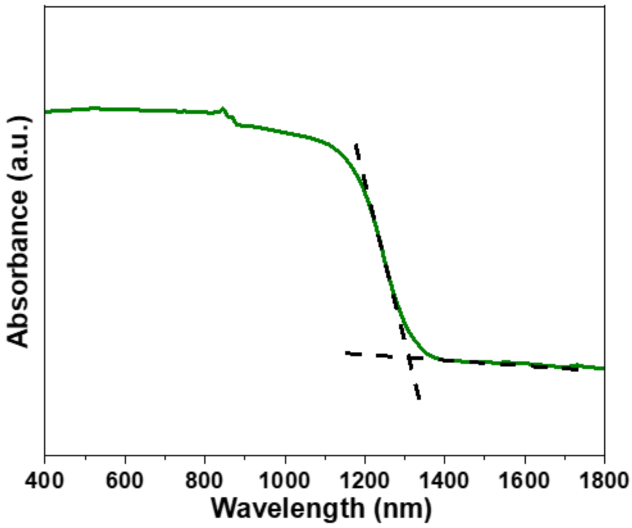

Figure 2.9. UV–Vis–NIR absorption spectrum of the synthesized NPs.

The conducted ligand exchange procedure allowed for the dispersion of the NPs in water/ethanol solvents comprising HPMC as a rheological additive for ink formulation. Notably, the use of WBM procedure gave access to a smoother screen-printed film with improved NPs dispersion (Figure 2.10). The resultant ink, with 40% NP content, revealed a non-Newtonian behavior, with a range of dynamic viscosity of 1.3–4.0 Pa s (Figure 2.11) and a surface tension of 34.3±3.6 $\mathrm{mN\,m^{-1}}$, suitable for screen printing deposition over SLG. Moreover, the TGA of the ink (Figure 2.12) revealed that 500 °C should be employed to remove organic matter from EDA and HPMC.

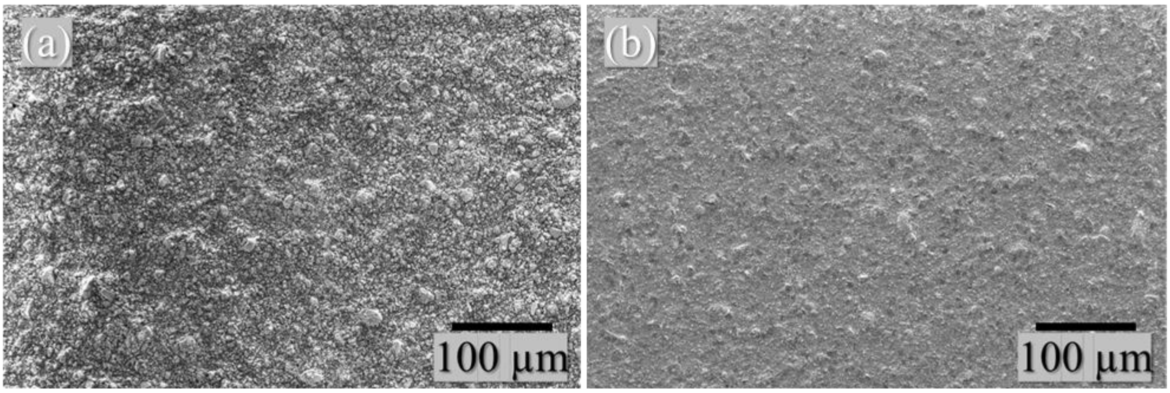

Figure 2.10. SEM surface images from screen-printed films of Sample II before (a) and after (b) WBM.

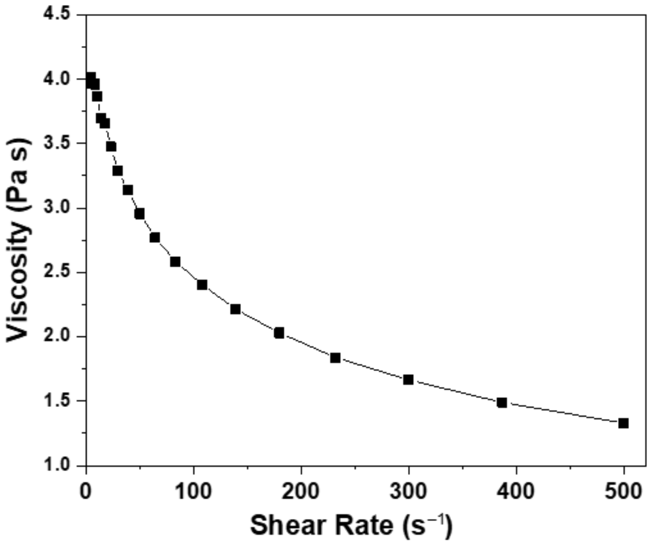

Figure 2.11. Dynamic viscosity of the formulated NP ink showing a non-Newtonian behavior.

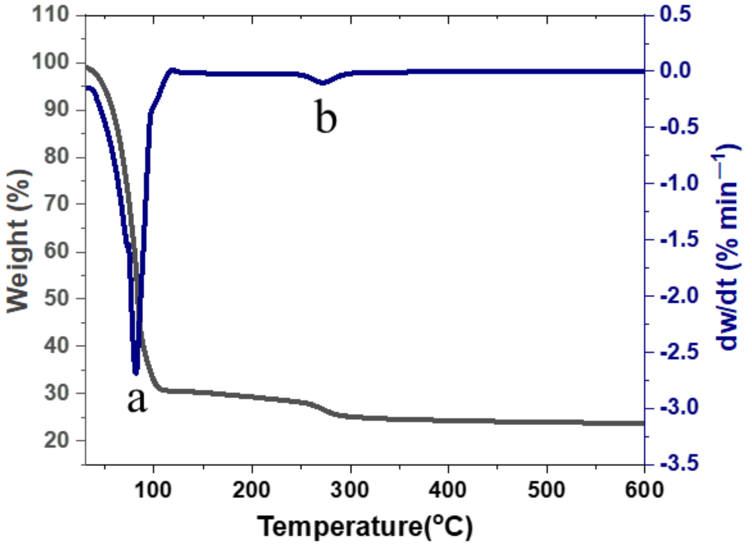

Figure 2.12. Thermogravimetric analysis with the corresponding derivative curve for the screen printable ink under Ar. Peak temperatures a: 81 °C and b: 271 °C.

After employing five-step screen printing of the developed ink and annealing the resultant film at 500 °C to eliminate all organic matter, a porous photoabsorber layer with homogenous thickness of ≈4.5 μm was observed through SEM surface and cross-sectional imaging (Figure 2.13a, b). HAADF–STEM data (Figure 2.13c, d) showed CIGSe NPs surrounded by a tiny layer of carbon, probably arising from the rheological HPMC additive used in the ink formulation, suggesting that a longer annealing treatment should be performed. STEM–EDX (Figure 2.13e) reveals a more uniform distribution of the metals as compared to the powder STEM–EDX analysis.

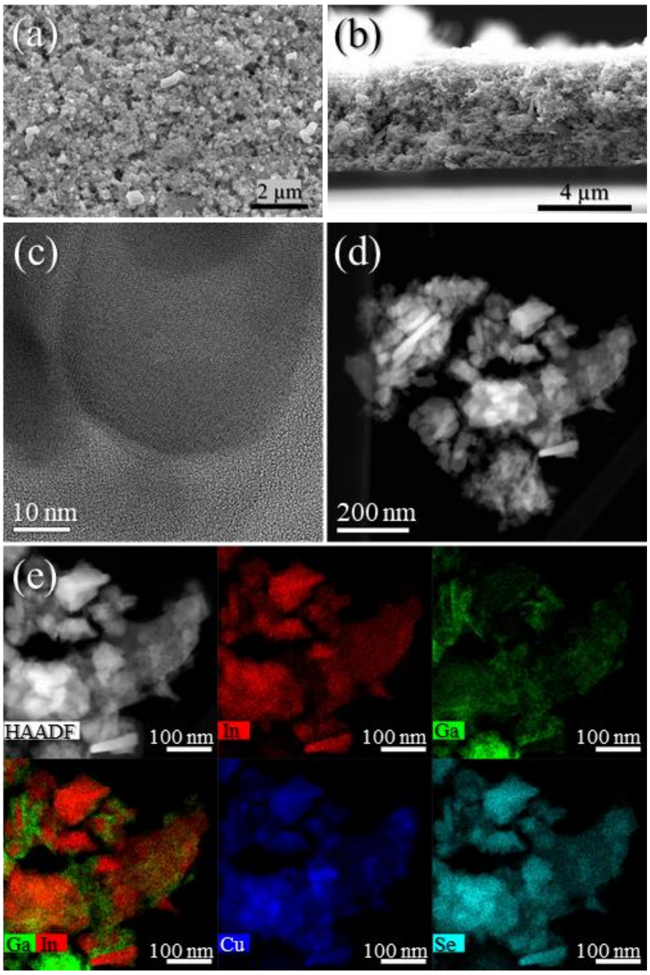

Figure 2.13. SEM surface (a) and cross-sectional (b) images and HAADF–STEM images (c, d) with STEM–EDX maps (e) from screen-printed film of Sample II after annealing.

The resultant screen-printed film after annealing is a phase-pure CIGSe with tetragonal chalcopyrite structure (space group $I\bar{4}2d$) with no signs of undesirable secondary phases (Figure 2.14a). The major peaks found at 26.8, 44.6, and 52.9° correspond to (112), (220/204), and (312/116) reflections of chalcopyrite CIGSe phase [9, 36], respectively. The Raman data (Figure 2.14b) revealed a sharp peak at around 174 cm^{-1}, corresponding to the A_1 vibrational mode of CIGSe and two broad bands at 126 cm^{-1} and 209 cm^{-1} corresponding to the B_1 and B_2/E modes, respectively [34, 35], without presence of CuSe_2 secondary phase.

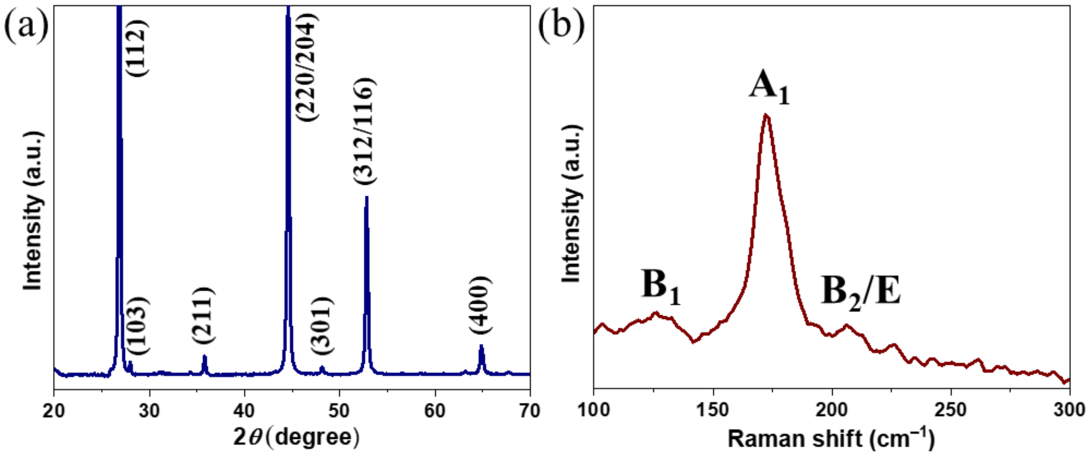

Figure 2.14. The experimental powder XRD pattern (a) and Raman spectrum (b) of the screen-printed film after annealing at 500 °C. In XRD figure, the *hkl* peak assignment is based on ICDD card no. 00-066-0140 for chalcopyrite.

2.4 Discussion

Based on a previous success in the synthesis of high-quality CISe NPs with the hexagonal wurtzite structure [20], the procedure has been adapted for the synthesis of CIGSe NPs. The developed synthesis delivered ~3.5 g of high-quality phase-pure CIGSe NPs with hexagonal wurtzite phase. Although several strategies have been reported for the synthesis of tetragonal chalcopyrite CIGSe NPs, syntheses of hexagonal wurtzite CIGSe is uncommon. Importantly, wurtzite metastable phase is characterized by an increased amount of bonds between Cu and Se atoms, resulting in an improved band structure in regard to the electron transition and transport due to the delocalized d electrons of Cu [37]. Accordingly, the absorption of light from visible and infrared re-gions is higher for wurtzite phase than for the chalcopyrite one, which can result in improved photovoltaic efficiency of devices based on wurtzite NPs [38].

The scale of the NP synthesis is of high importance when considering the ink formulation since substantial gram quantities of NPs are required. Gram-scale syntheses are quite common, e.g. Houck *et al.* synthesized ~1 g of wurtzite CIGSe NPs [23], Mousavi *et al.* prepared a few grams of chalcopyrite CIGSe [39], and Chang *et al.* produced ~1.3 g of quinary Cu(In,Ga)SSe NPs with chalcopyrite structure [40]. Larger sale syntheses of CIGSe NPs are less addressed but existent, e.g. Latha *et al.* synthesized ~3.1 g of chalcopyrite CIGSe [7]. Notably, the herein presented large-scale synthesis delivers a considerable amount of ~3.5 g of wurtzite CIGSe NPs.

The addition of Ga into CISe NP synthesis is known to significantly change the growth kinetics of the NPs, making the control over stoichiometry and structure challenging. Moreover, when dealing with NPs with wurtzite phase, annealing temperature of maximum 400 °C can be employed, otherwise a transformation to chalcopyrite phase will occur. In the present synthesis, the introduction of Ga gave access to phase-pure CIGSe NPs with hexagonal wurtzite structure. However, in addition to being distributed inside the NPs, Ga is also segregated on the surface of the NPs. To understand this behavior, DFT calculations have been employed to estimate the relaxed atomic structures of ordered orthorhombic models, representing the bulk of wurtzite-phase CISe crystal and a thin film slab of it. The crystallographic directions of CISe corresponding to the two open surfaces of hexagonal NPs has been previously identified [20] (Figure 2.15a, e). The relaxed atomic structures of these surfaces are shown in the Figure 2.15c, g.

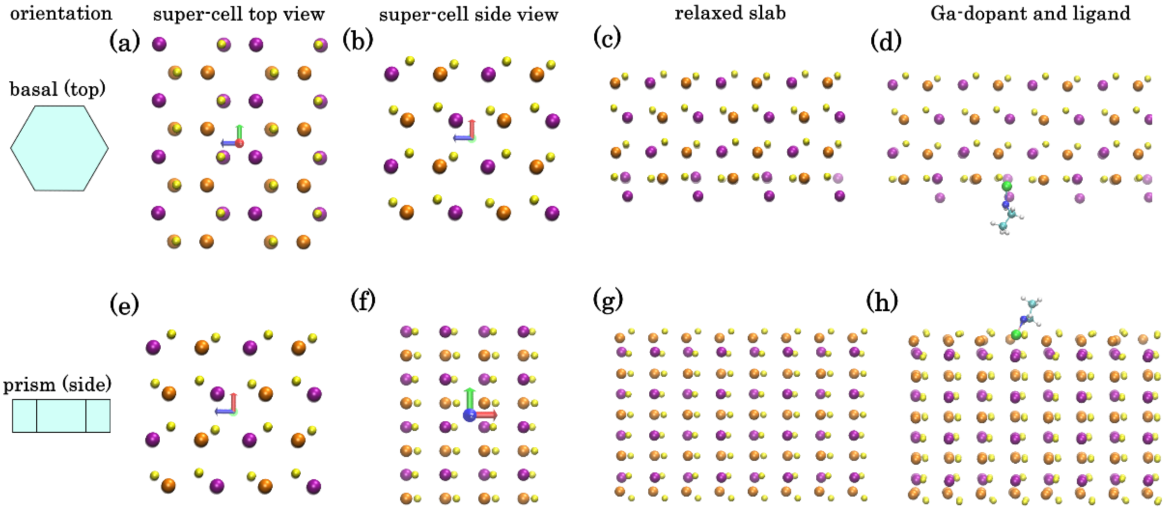

Figure 2.15. Ordered CISe orthorhombic model of the top or basal (a–d) and side or prism (e–h) surfaces of hexagonal nanoparticle: idealized super-cell top view (a, e) and side view (b, f) and density functional theory relaxed atomic structures of the pure surface slabs (c, g) and with Ga dopant and $-NH-C_2H_5$ passivating group (d, h). Legend: In (purple), Cu (orange), Se (yellow), Ga (green), N (deep blue), C (light blue), and H (white).

Top (basal-faceted) surface of a hexagonal NP (Figure 2.15a-d): DFT calculations show that a monocrystalline slab with such lattice has two unequal faces: Se-rich (top) and Cu/In-rich (bottom). In the absence of passivation, while the upper Se-face is stable, the bottom Cu/In-face is less so and undergoes significant restructure to minimize tension (Figure 2.15c). To assess the effect of Ga dopant on CISe crystal the calculations have been repeated by placing Ga instead of one of the In atoms in the bulk or on the exposed plane. The tendency of a dopant atom to segregate to the surface can be characterized through "segregation energy": $\Delta E_{seg} = (E_{slab[Ga-doped]} - E_{slab[pure]}) - (E_{bulk[Ga-doped]} - E_{bulk[pure]})$, where $E_{bulk/slab}$ represents the total (ionic + electronic energy as calculated by DFT) of a periodic unit of a bulk system or a surface slab [41]. In case of Ga dopant in the wurtzite CISe crystal the estimated segregation energy of $\sim$–3 $\mathrm{kcal\ mole^{-1}}$ per dopant atom is obtained, indicating that positioning of Ga on such surface is thermodynamically favorable.

Even more pronounced this effect is for the side (prism-faceted) surface (Figure 2.15e-h): DFT calculations show that for ideal lattice a minimal energy surface is Cu-rich plane with the formation enthalpy ($\sim$35 $\mathrm{kcal\ mole^{-1}}$ per 144 atom super-cell) lower than a similar In-rich surface. However, surface Cu atoms are prone to substitution by Ga: the segregation energy for a single Ga adatom from bulk to replace a surface Cu atom was estimated to be –20 $\mathrm{kcal\ mole^{-1}}$. Therefore, segregation of Ga adatom to Cu-rich side surfaces of hexagonal NPs is highly favorable, leading to a self-exclusion effect of Ga in the CIGSe NPs. This correlates with Ga concentration map in the Figure 2.4.

To assess the effect of passivating ligands, DFT calculations have been conducted for thin film slab surface with ethylamine group (imitating the effect of longer HDA) attached to a surface Ga, In or Cu atoms (Figure 2.15d, h). By analogy the gain from passivating either atom with ligand has been compared by calculating: $\Delta E_{passiv} = (E_{passiv[Ga]} - E_{free[Ga]}) - (E_{passiv[In]} - E_{free[In]})$. Again, a ΔE_{passiv} $\sim$–16.3 $\mathrm{kcal\ mole^{-1}}$ per Ga dopant for In-rich top surface and –28.5 $\mathrm{kcal\ mole^{-1}}$ for Cu-rich side, indicating that surface Ga atoms are energetically favorable in the presence of amine group ligands. These computational results explain the Ga segregation in the **Sample I** produced in this study. The adjustment of the metal ratios and introduction of Cu vacancies in **Sample II** may provide additional stabilization factor, preventing the Ga segregation.

With understanding of synthesis, structural and thermal stability of synthesized CIGSe NPs, a model of screen-printed photoabsorber layer was developed. The remotion of the surface ligands requires annealing temperatures higher than wurtzite-chalcopyrite transformation, thus the resulted film with homogenous thickness of $\sim$4.5 µm is composed by CIGSe chalcopyrite NPs. Despite the NPs' optimal structural properties, organic residues were detected, and the resulting film presented a porous layer with low grain size. Further optimization of the film with lower porosity and better electronic properties should be conducted. In summary, the herein synthesized NPs are suitable for printing deposition of the photoabsorber layer, opening ways for the roll-to-roll production of efficient CIGSe PV systems.

2.5 Conclusions

The herein presented large-scale heat-up synthesis delivered ~3.5 g of phase-pure wurtzite CIGSe NPs with 10–70 nm of size. The synthesized NPs with chemical composition of $\mathrm{Cu_{0.89}(In_{0.72}Ga_{0.28})Se_2}$, showed high crystallinity and wide absorption range from visible to near-infrared regions, well-matching with the properties of analogous NPs used in high efficiency PV systems. Moreover, it has been found that Ga, besides being distributed inside the CIGSe NPs, is also segregated at the surface of the synthesized NPs. *In silico* calculations support that it is thermodynamically favorable for Ga atoms to segregate onto the surface of wurtzite phase CISe NP both in case of non-passivated surface and in the presence of amine-based ligands. Finally, screen-printed thin films with homogenous thickness of ~4.5 μm have been produced by formulating a water-based ink with the synthesized NPs embedded, paving the way to the roll-to-roll production of CIGSe PV systems.

2.6 References

1. Feurer, T., et al., *Progress in thin film CIGS photovoltaics – Research and development, manufacturing, and applications.* Progress in Photovoltaics: Research and Applications, 2017. **25**(7): p. 645-667.
2. Lee, K., et al., *The Development of Transparent Photovoltaics.* Cell Reports Physical Science, 2020. **1**(8): p. 100143.
3. Banik, U., et al., *Enhancing passive radiative cooling properties of flexible CIGS solar cells for space applications using single layer silicon oxycarbonitride films.* Solar Energy Materials and Solar Cells, 2020. **209**: p. 110456.
4. Gulkowski, S. and E. Krawczak, *RF/DC Magnetron Sputtering Deposition of Thin Layers for Solar Cell Fabrication.* Coatings, 2020. **10**(8): p. 791.
5. Latha, M., R. Aruna Devi, and S. Velumani, *Hot injection synthesis of* $Cu(In, Ga)Se_2$ *nanocrystals with tunable bandgap.* Optical Materials, 2018. **79**: p. 450-456.
6. Faraj, M.G., K. Ibrahim, and A. Salhin, *Fabrication and characterization of thin-film* $Cu(In,Ga)Se_2$ *solar cells on a PET plastic substrate using screen printing.* Materials Science in Semiconductor Processing, 2012. **15**(2): p. 165-173.
7. Latha, M., et al., *Solution based synthesis of* $Cu(In,Ga)Se_2$ *microcrystals and thin films.* RSC Advances, 2019. **9**(60): p. 35197-35208.
8. Tang, J., et al., *Synthesis of Colloidal* $CuGaSe_2$, $CuInSe_2$, *and* $Cu(InGa)Se_2$ *Nanoparticles.* Chemistry of Materials, 2008. **20**(22): p. 6906-6910.
9. Chun, Y.G., K.H. Kim, and K.H. Yoon, *Synthesis of* $CuInGaSe_2$ *nanoparticles by solvothermal route.* Thin Solid Films, 2005. **480-481**: p. 46-49.
10. Liu, Y., et al., *Preparation of* $Cu(In,Ga)Se_2$ *Thin Film by Solvothermal and Spin-coating Process.* Energy Procedia, 2012. **16**: p. 217-222.
11. Saber, S.K.A.-H., et al. *Synthesis of* $Cu(In_xGa_{1-x})Se_2$ *Nanoparticles for Photovoltaic Applications*. in *International Renewable and Sustainable Energy Conference*. 2017.
12. Báez, Y.T.C., et al., *Hydrothermal synthesis of a photovoltaic material based on* $CuIn_{0.5}Ga_{0.5}Se_2$. Journal of Physics: Conference Series, 2017. **935**: p. 012004.

13. Vidhya, B., et al., *Structural studies of mechano-chemically synthesized CuIn$_{1-x}$Ga$_x$Se$_2$ nanoparticles.* Materials Science and Engineering: B, 2010. **174**(1): p. 216-221.
14. Rohini, M., et al., *Parametric optimization of mechanochemical process for synthesis of Cu(In,Ga)$_{0.5}$Se$_2$ nanoparticles.* Materials Science in Semiconductor Processing, 2015. **37**: p. 151-158.
15. Coughlan, C., et al., *Compound Copper Chalcogenide Nanocrystals.* Chemical Reviews, 2017. **117**(9): p. 5865-6109.
16. Norako, M.E. and R.L. Brutchey, *Synthesis of Metastable Wurtzite CuInSe$_2$ Nanocrystals.* Chemistry of Materials, 2010. **22**(5): p. 1613-1615.
17. Park, J.S., et al., *CuInSe$_2$ phase formation during Cu$_2$Se/In$_2$Se$_3$ interdiffusion reaction.* Journal of Applied Physics, 2000. **87**(8): p. 3683-3690.
18. Wang, J.-J., et al., *Synthesis of Monodispersed Wurtzite Structure CuInSe$_2$ Nanocrystals and Their Application in High-Performance Organic−Inorganic Hybrid Photodetectors.* Journal of the American Chemical Society, 2010. **132**(35): p. 12218-12221.
19. Tappan, B.A., et al., *Utilizing Diselenide Precursors toward Rationally Controlled Synthesis of Metastable CuInSe$_2$ Nanocrystals.* Chemistry of Materials, 2018. **30**(16): p. 5704-5713.
20. Sousa, V., et al., *Superstructural Ordering in Hexagonal CuInSe$_2$ Nanoparticles.* Chemistry of Materials, 2019. **31**(1): p. 260-267.
21. Brutchey, R.L., *Diorganyl Dichalcogenides as Useful Synthons for Colloidal Semiconductor Nanocrystals.* Accounts of Chemical Research, 2015. **48**(11): p. 2918-2926.
22. Wang, Y.-H.A., et al., *Synthesis of Shape-Controlled Monodisperse Wurtzite CuIn$_x$Ga$_{1-x}$S$_2$ Semiconductor Nanocrystals with Tunable Band Gap.* Journal of the American Chemical Society, 2011. **133**(29): p. 11072-11075.
23. Houck, D.W., et al., *CuGaSe$_2$ and CuIn$_x$Ga$_{1-x}$Se$_2$ Nanocrystals with Sphalerite or Wurtzite Phase for Optoelectronic Applications.* ACS Applied Nano Materials, 2019. **2**(7): p. 4673-4680.
24. Heinemann, M.D., et al., *Evolution of opto-electronic properties during film formation of complex semiconductors.* Scientific Reports, 2017. **7**(1): p. 45463.
25. Carron, R., et al., *Advanced Alkali Treatments for High-Efficiency Cu(In,Ga)Se$_2$ Solar Cells on Flexible Substrates.* Advanced Energy Materials, 2019. **9**(24): p. 1900408.
26. Brown, P.R., et al., *Energy Level Modification in Lead Sulfide Quantum Dot Thin Films through Ligand Exchange.* ACS Nano, 2014. **8**(6): p. 5863-5872.
27. Chupas, P.J., et al., *A versatile sample-environment cell for non-ambient X-ray scattering experiments.* Journal of Applied Crystallography, 2008. **41**(4): p. 822-824.
28. Chen, Q., et al., *Printed ethyl cellulose/CuInSe$_2$composite light absorber layer and its photovoltaic effect.* Journal of Physics D: Applied Physics, 2011. **44**(45): p. 455401.
29. Arias, M.M., *Vienna Ab-initio Simulation Package.* Univ. Edinburgh, 2009.
30. Soler, J.M., et al., *The SIESTA method forab initioorder-Nmaterials simulation.* Journal of Physics: Condensed Matter, 2002. **14**(11): p. 2745-2779.
31. Perdew, J.P., K. Burke, and M. Ernzerhof, *Generalized Gradient Approximation Made Simple.* Physical Review Letters, 1996. **77**(18): p. 3865-3868.
32. van Setten, M.J., et al., *The PseudoDojo: Training and grading a 85 element optimized norm-conserving pseudopotential table.* Computer Physics Communications, 2018. **226**: p. 39-54.
33. Pan, D., et al., *Synthesis of Cu−In−S Ternary Nanocrystals with Tunable Structure and Composition.* Journal of the American Chemical Society, 2008. **130**(17): p. 5620-5621.
34. Rincón, C. and F.J. Ramírez, *Lattice vibrations of CuInSe$_2$ and CuGaSe$_2$ by Raman microspectrometry.* Journal of Applied Physics, 1992. **72**(9): p. 4321-4324.
35. Choi, I.-H., *Raman spectroscopy of CuIn$_{1-x}$Ga$_x$Se$_2$ for in-situ monitoring of the composition ratio.* Thin Solid Films, 2011. **519**(13): p. 4390-4393.

36. Der Wu, J., L. Ting Wang, and C. Gau, *Synthesis of CuInGaSe$_2$ nanoparticles by modified polyol route.* Solar Energy Materials and Solar Cells, 2012. **98**: p. 404-408.
37. Witt, E. and J. Kolny-Olesiak, *Recent Developments in Colloidal Synthesis of CuInSe$_2$ Nanoparticles*. Chemistry – A European Journal, 2013. **19**(30): p. 9746-9753.
38. Fan, F.-J., L. Wu, and S.-H. Yu, *Energetic I–III–VI$_2$ and I$_2$–II–IV–VI$_4$ nanocrystals: synthesis, photovoltaic and thermoelectric applications*. Energy & Environmental Science, 2014. **7**(1): p. 190-208.
39. Mousavi, S.H., et al., *Faster synthesis of CIGS nanoparticles using a modified solvothermal method.* Journal of Alloys and Compounds, 2016. **659**: p. 178-183.
40. Chang, S.-H., et al., *Facile colloidal synthesis of quinary* $CuIn_{1-x}Ga_x(S_ySe_{1-y})_2$ *(CIGSSe) nanocrystal inks with tunable band gaps for use in low-cost photovoltaics.* Energy & Environmental Science, 2011. **4**(12): p. 4929-4932.
41. Zhevnenko, S.N., et al., *Surface and segregation energies of Ag based alloys with Ni, Co and Fe: Direct experimental measurement and DFT study.* Acta Materialia, 2021. **205**: p. 116565.

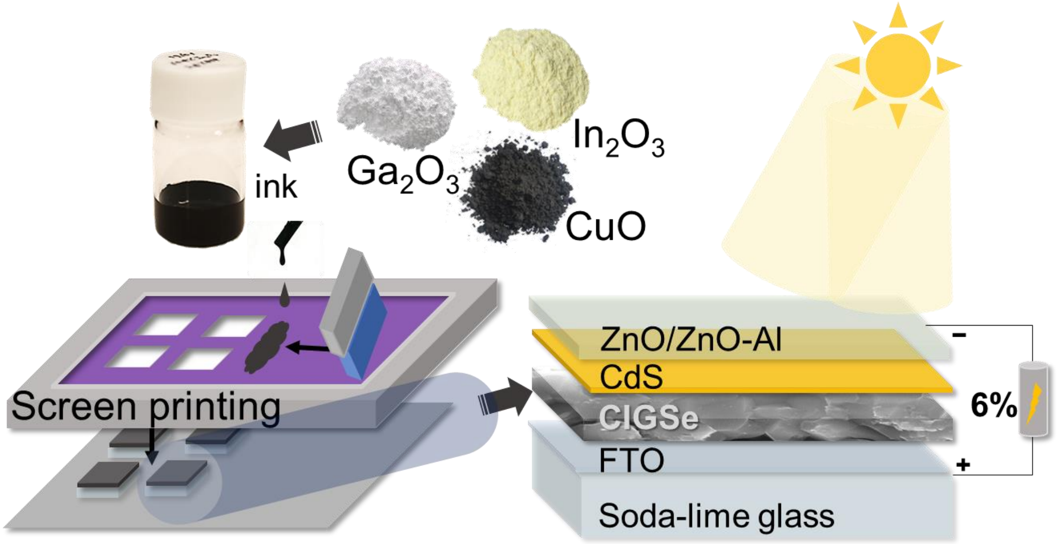

Chapter 3. Over 6% efficient $Cu(In,Ga)Se_2$ solar cell screen-printed from oxides on FTO

Printing and coating deposition processes are highly desirable for the industrial roll-to-roll production of cost-efficient photovoltaic devices. In this chapter, a new approach to produce $\mathrm{Cu(In,Ga)Se_2}$ photovoltaic cells on conductive fluorine-doped tin oxide is presented, resulting in a device with over six per cent of efficiency. To this end, commercial oxide nanoparticles have been dispersed into a high-quality screen printable ink based on ethyl cellulose solution in terpineol. The high homogeneity and good adhesion properties of the formulated oxide ink play an important role in obtaining dense and highly crystalline photoabsorber layers. These findings reveal that solution-based screen printing from readily available oxide precursors provide an interesting cost-effective alternative to current vacuum- and energy-demanding processes for the fabrication of $\mathrm{Cu(In,Ga)Se_2}$ photovoltaic devices.

This chapter is based on the following publication: V. Sousa, **B. F. Gonçalves**, Y. S. Rosen, J. Virtuoso, P. Anacleto, M. F. Cerqueira, E. Modin, P. Alpuim, O. I. Lebedev, S. Magdassi, S. Sadewasser, and Y. V. Kolen'ko, *Over 6% efficient Cu(In,Ga)Se₂ solar cell screen-printed from oxides on FTO,* ACS Applied Energy Materials, 3(4), 202, 3120-3126.

3.1 Introduction

The most efficient CIGSe PV devices are currently fabricated either by co-evaporation or sputtering, followed by a selenization step, delivering a maximum efficiency of 23.4% [1]. Both are expensive fabrication techniques based on vacuum processing. Interestingly, solution-based printing/coating technologies, compatible with roll-to-toll production, represent viable methods for reducing the energy demand of CIGSe fabrication [2]. Recently, solution-processed CIGSe PV cells have reached 17.3% of efficiency [3]. However, so far, most of the reported efforts are focused on using inks based on CIGSe NPs or metallic precursors for solution-processed CIGSe photoabsorber, while only few reports are available for oxide-based inks.

Thus, this chapter presents a facile screen printing approach to CIGSe PV cells using commercially available copper(II) oxide (CuO), indium(III) oxide ($\mathrm{In_2O_3}$), and gallium(III) oxide ($\mathrm{Ga_2O_3}$) as the key constitute starting materials. These oxides are easy to synthesize and sometimes they can be harvested directly from the earth's crust [4], and are therefore commercially readily available. Among the scarce reports on metal oxides as precursors for screen printing ink formulation [4-6], an intermediate thermal annealing step is typically required to reduce the pristine oxides into metals, followed by the selenization step to convert the metals into CIGSe phase. The herein presented work offers the practical advantage of omitting the reduction step, delivering a PV device with 6% of efficiency.

3.2 Experimental

3.2.1 Chemicals

The following reagents were purchased and used as received: copper oxide nanopowder (CuO, ≥99%, 30–50 nm, Alfa Aesar), indium oxide nanopowder ($\mathrm{In_2O_3}$, 99.9%, <100 nm, Sigma-Aldrich), gallium oxide ($\mathrm{Ga_2O_3}$, 99.999%, ≈325 mesh powder, Alfa Aesar), di(propylene glycol) methyl ether, (DPM, ≥99%, Sigma-Aldrich), oleic acid (OA, 90%, Sigma-Aldrich), terpineol (Sigma-Aldrich), ethyl cellulose (EC, 48% ethoxyl, Sigma-Aldrich), selenium shots (Se, amorphous, 99.999%, 2–6 mm, Alfa Aesar), potassium cyanide (KCN, ≥98.0%, Sigma-Aldrich), thiourea ($\mathrm{CS(NH_2)_2}$, ≥99.0%, Sigma-Aldrich), cadmium acetate ($\mathrm{Cd(ac)_2}$, 99.995%, Sigma-Aldrich), ammonium hydroxide aqueous solution (28–30%, Acros Organics), acetone (≥99.5%, Honeywell), IPA (≥99.8%, Honeywell) and ethanol (≥99.8%, Honewywell). Ultrapure water was produced by MQ Advantage A10 system (Millipore) with resistivity of 18.2 MΩ.cm.

3.2.2 Oxide ink formulation

For the precursor ink formulation, 1.684 g of CuO, 2.572 g of In_2O_3 and 0.744 g of Ga_2O_3 with nominal ratio of [Cu] / [In + Ga] $\approx$ 0.8 and [Ga] / [Ga + In] $\approx$ 0.3, were dispersed in 50 g of DPM, and 2 g of OA and then subjected to wet bead milling at 5000 rpm for 30 min using a Dyno Mill (WAB). Then, the oxide mixture was separated from DPM and OA by centrifugation at 1000 RPM for 30 min followed by 5000 RPM for 30 min, and the resultant wet paste was stored in a vial. A 5% solution of EC in terpineol was prepared by the dissolution of the appropriate amount of EC in terpineol at 70 °C under stirring. To prepare an ink with 50% weight content of the oxides, the appropriate amount of oxide wet paste was added into the 5% EC solution in terpineol. Finally, the ink was mixed first with a spatula and then let stir on magnetic stirring plate, at RT, overnight.

3.2.3 Oxide ink properties

The contact angle of the oxide ink on FTO substrate was measured to be 27° ± 2°, while the surface tension was calculated to be 32.9 $\mathrm{mN\ m^{-1}}$. Dynamic viscosity with non-Newtonian behavior was observed with a range of dynamic viscosity between 0.7–1.9 Pa s (Figure 3.1). Surface energy of the FTO substrate was determined to be 74.39 $\mathrm{mN\ m^{-1}}$.

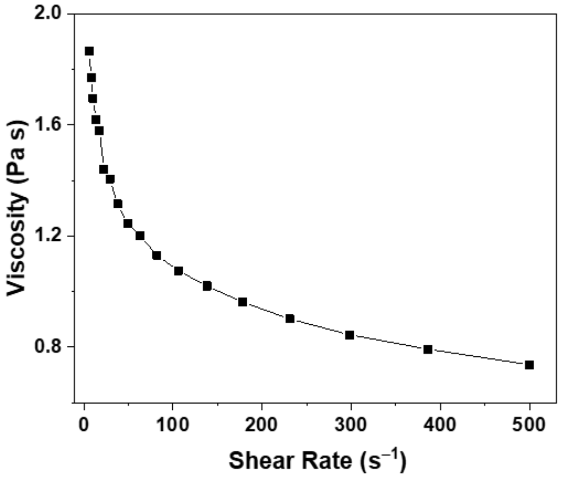

Figure 3.1. Dynamic viscosity of the as-formulated oxide ink with a non-Newtonian characteristic behavior of the ink.

3.2.4 Screen printing

For printing, 2.5 × 2.5 $\mathrm{cm^2}$ FTO coated SLG substrate (FTO/SLG, 7Ω sq Dyesol) with 2 mm of thickness was cleaned as described on Chapter 2 (section 2.2.4). Then, square patterns of

2.5×2.5 cm^2 were printed above the previously cleaned FTO/SLG substrates using a semi-automatic screen printer as described Chapter 2 (section 2.2.4).

3.2.5 Photovoltaic device fabrication

For the photoabsorber film deposition on FTO/SLG, the oxide ink was screen-printed twice using a 180 $\mathrm{threads\ cm^{-1}}$mesh screen printer and dried at 100 °C on a hot plate after both depositions for 3 min. Afterwards, the as-printed photoabsorber layer was calcined at 400 °C for 30 min to remove residual organics (DPM, OA, EC, terpineol), and subjected to the selenization procedure. The selenization was performed in a tubular furnace, where two film samples were placed inside a graphite box alongside with 0.3 g of elemental Se, and charged into a quartz tube. Prior to selenization, the tube was flushed with $5\%\mathrm{H_2/Ar}$ mixture at 100 sccm during 1 h. Then, under $5\%\mathrm{H_2/Ar}$ flow, the furnace was heated to 550 °C at 50 $°\mathrm{C\ min^{-1}}$, held at this temperature for 20 min, and then immediately opened to ensure rapid cooling. During cooling, the gas flow inside the quartz tube was changed to Ar.

The as-prepared film samples were etched by aqueous 5% KCN solution at RT for 30 s. To deposit ≈70 nm of CdS buffer layer, the CBD technique was employed. A water bath was heated to 60 °C and the deposition solution was prepared: 85 mL of MQ water, 15 mL of ammonium hydroxide, 0.13 g of cadmium acetate dissolved in 15 mL of MQ water, and 1.33 g of thiourea dissolved in 15 mL of MQ water. The film samples were then placed inside the deposition solution and let react for 7 minutes while mixing the solution for 10 s at the beginning of each minute by moving the sample up and down.

The window layers were deposited by sputtering at 160 W and 20 sccm of Ar flow. An *i*–ZnO resistive layer was first deposited during 4 min, followed by sputtering of AZO transparent conducting window layer for 14 min. This sputtering procedure provides 50 nm and 200 nm thick i-ZnO and AZO layers, respectively.

To finalize the PV device, one edge of the device was scratched with a scalpel to reach the back contact FTO, which was then filled-up with a thin layer of indium metal welded to ensure a good contact with the probes for the *J*–*V* measurements.

3.2.6 Characterization

Surface tension and rheological properties:

The contact angle, surface tension and surface energy were measured at 22 °C using DSA–CA as described on Chapter 2 (section 2.2.5). Water and diiodomethane were employed to determine the surface energy of the FTO substrate.

The RT ink dynamic viscosity measurements were performed on a rheometer as described on Chapter 2 (section 2.2.5).

X-ray diffraction:

The phase composition of the films was determined using XRD as described on Chapter 2 (section 2.2.5).

Raman spectroscopy:

To inspect the local structure of the CIGSe photoabsorber layer, Raman spectroscopy measurements were performed as described on Chapter 2 (section 2.2.5), using a laser beam power of 2 mW.

Electron microscopy:

The morphology of the photoabsorber layer and final PV device were analyzed by SEM using Quanta 650 FEG ESEM and Helios NanoLab 450S DualBeam microscopes (FEI), fitted with the spectrometers for EDX.

The focused ion beam (FIB) method was used to prepare the lamella for cross-sectional investigation. To investigate fine microstructure and the chemical composition of the final FTO/CIGSe/CdS/*i*-ZnO/AZO PV devices, HAADF–STEM, SAED, and STEM–EDX were performed using JEM-ARM200F cold FEG probe and image aberration-corrected microscope (JEOL), operated at 200 kV and equipped with large angle CENTURIO EDX detector and QUANTUM GIF.

Optical properties:

UV-Vis-NIR optical measurements and the band gap determination of the CIGSe photoabsorber films were carried out as described on Chapter 2 (section 2.2.5).

J–*V* characterization:

J–*V* curves of the PV cells were measured by a four-point probe system Oriel Sol3A Class AAA Solar Simulator (Newport), with $100\ \mathrm{mW\,cm^{-2}}$ illumination source using an AM 1.5 filter. Prior to all measurements, the confirmation of total illumination irradiance was conducted using a silicon reference cell, verifying an irradiance of 0.994 or 1.010 for different measurements, which is consistent with the 1 Sun ± 2% error for irradiance measured at the plane of the PV cell according to the Standard Testing Conditions. For each sample, ≈10 cells with an area of ≈0.28 cm^2 each were isolated and measured using a two-probe system, placed on the top contact active area cell of AZO, and on indium-welded back contact. Prior to measurement, the light intensity was calibrated by using a mono-silicon reference cell with a BK7 optical window calibrated by the National Renewable Energy Laboratory (NREL). A shadow mask was used to cover the active area to avoid the interference from both scattering light and adjacent current leakage.

3.3 Results and Discussion

3.3.1 Screen-printed CIGSe photoabsorber layer

The initial point of this work was the formulation of high-quality oxides-based ink for screen printing. For this purpose, the selected stoichiometric mixture of commercial Cu(II), In(III), and Ga(III) oxides was subjected to wet bead milling in the presence of DPM and OA. After this step, the resultant wet paste was dispersed in EC dissolved in terpineol solution. The EC acts both as a rheological agent to enable a high viscosity ink, and as a binder to improve the adhesion of the printed pattern to the substrate [7]. The ink was optimized to obtain a good stability, dispersion, wettability, and uniformity of the screen-printed pattern on the substrate. After successful screen printing of two layers of the as-formulated oxide ink on FTO/SLG substrate, the obtained film was calcined at 400 °C to remove carbon-based residues and subjected to rapid selenization at 550 °C under $5\%\mathrm{H_2/Ar}$ flow.

The phase composition of the resultant film was evaluated by XRD (Figure 3.2a). According to the results, the photoabsorber layer has a phase mixture of FTO substrate and tetragonal CIGSe with the chalcopyrite structure [6, 8, 9]. Furthermore, the phase analysis demonstrates no evidences of the presence of oxides or other phases, suggesting that the metal oxides react with selenium vapor under diluted hydrogen atmosphere, leading to the formation of CIGSe, as described by the following chemical reaction (Equation 3.1):

$$\mathrm{2CuO + In_2O_3 + Ga_2O_3 + 4Se + 8H_2 = 2Cu(In,Ga)Se_2 + 8H_2O} \quad (3.1)$$

The convenience of this synthetic protocol is that the conversion of the oxides into crystalline CIGSe is accomplished in a single step under reductive atmosphere of $\mathrm{H_2}$.

Notably, the Raman spectroscopy data (Figure 3.2b) revealed results consistent with those of the XRD, showing a major sharp peak at 173 cm^{-1} with full width at half maximum (FWHM) of $11\ \mathrm{cm}^{-1}$ corresponding to the A_1 vibrational mode of CIGSe [10, 11]. Moreover, the two broader peaks at 120 and 218 cm^{-1} are in good agreement with the B_1 and B_2/E modes of CIGSe, respectively [11, 12]. Interestingly, it was observed a shoulder peak at 188 cm^{-1}, which is not associated with any Cu–In–Ga–Se phases. Hence, the detected band is due to A_{1g} mode of SnSe_2 compound [10], suggesting an alloying of Sn from the FTO into the CIGSe layer.

Notably, SEM imaging data (Figure 3.2c, d) show the overall top-view morphology of the resultant photoabsorber deposited on FTO/SLG, where is detectable a uniform and reasonably dense appearance of μm-sized crystals, indicating significant grain growth of the CIGSe phase during selenization. However, the surface of the photoabsorber layer is quite rough, which is a result of the random orientation of the inter-grown CIGSe crystals. The chemical composition and stoichiometry results given by SEM-EDX analysis shows that the CIGSe phase is depleted in Ga in comparison to the initial oxide ratio of [Cu] / [In + Ga] = 0.8 and [Ga] / [In + Ga] = 0.3, exhibiting after selenization the following ratio: [Cu] / [In + Ga] = 1.0 and [Ga] / [In + Ga] = 0.23.

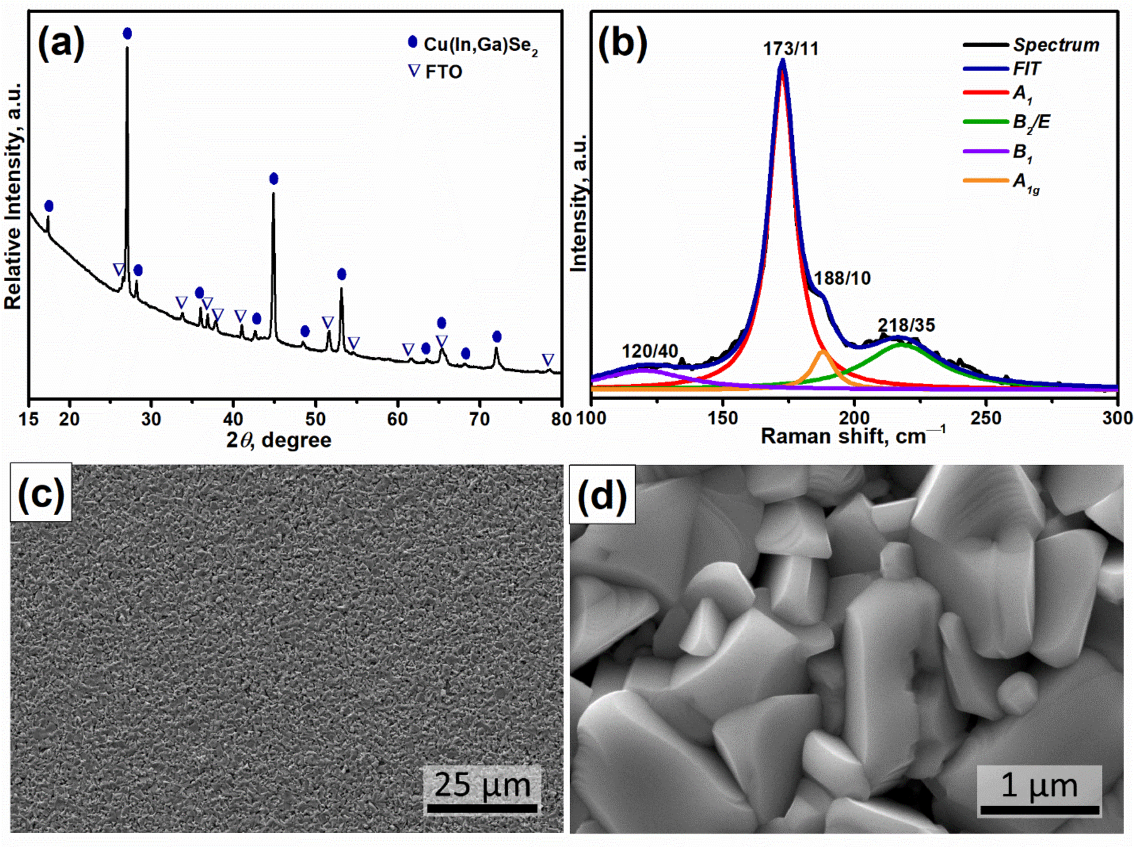

Figure 3.2. (a) XRD pattern of the CIGSe photoabsorber layer on FTO substrate. Ovals and triangles correspond to the positions of the most intense Bragg reflections expected for CIGSe (*hkl* peak assignment is based on ICDD No. 01-083-3357 for tetragonal CIGSe) and FTO, respectively. (b) Lorentzian fit (blue) of the experimental Raman data (black) for the CIGSe photoabsorber layer. The position/FWHM (in cm^{-1}) is provided for each component. Top surface low (c) and high (d) magnification SEM images of the as-fabricated CIGSe film.

To evaluate the optical properties of the resultant photoabsorber layer, UV–Vis–NIR spectroscopy was employed and the resultant absorption spectrum (Figure 3.3), shows that the produced CIGSe film strongly absorbs light from the visible to the near-infrared regions. The optical band gap of the resultant CIGSe layer was estimated to be 1.04±0.02 eV, which is slightly lower than the optimal values (1.1–1.14 eV) previously reported for bulk CIGSe chalcopyrite [2, 13].

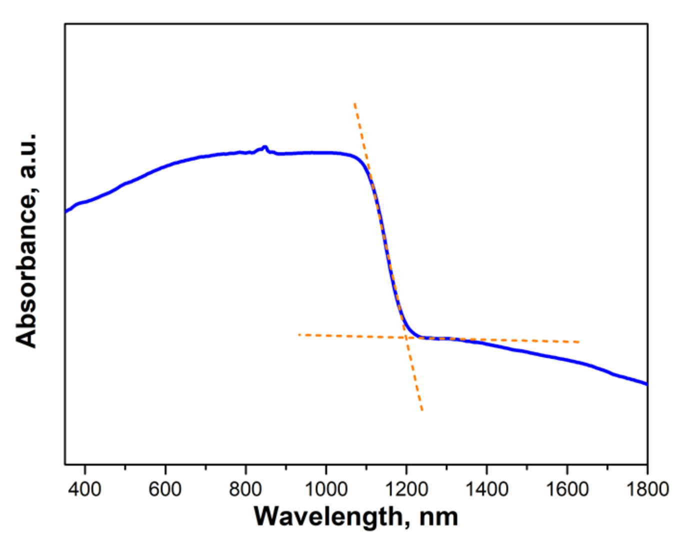

Figure 3.3. UV–Vis–NIR absorption spectrum of a representative CIGSe film.

3.3.2 CIGSe photovoltaic device

Notably, the presented results evidence that the screen-printed oxides ink with further selenization enables the formation of a high-quality CIGSe photoabsorber thin film. Hence, the fabrication of a CIGSe PV cell was conducted. Briefly, to create a heterojunction, a 70 nm of *n*-type CdS buffer layer was deposited by CBD on top of the *p*-type CIGSe photoabsorber. Next, 50 nm of *i*–ZnO layer was sputtered on top of CdS, followed by the sputtering of 200 nm of AZO as the top layer. This fabrication procedure enables a reliable process for the fabrication of SLG/FTO/CIGSe/CdS/*i*–ZnO/AZO PV devices.

In order to conduct a cross-sectional investigation of the resultant PV device by TEM, a FIB specimen preparation was employed. SEM imaging of the resultant lamella (Figure 3.4) and HAADF–STEM investigation conducted on the lamella together with ED studies are next summarized (Figures 3.5 and 3.6). A multilayered microstructure of the PV device is confirmed by the STEM observations (Figure 3.5 and 3.6a). Moreover, the presence of voids, which are microstructural defects at the interface between FTO substrate and CIGSe layer, can be clearly seen in Figures 3.4, 3.5 and 3.6a. Interestingly, similar microstructural defects have been reported in literature [14]. The grains of the photoabsorber CIGSe layer itself are highly crystalline and structurally defect-free, as seen in the HAADF-STEM images and the corresponding SAED patterns (Figures 3.6b–d). Regardless of the voids observed at the FTO/CIGSe interface, the HAADF–STEM imaging of the interface reveals nearly epitaxial growth of CIGSe on top of the FTO substrate (Figure 3.6e), suggesting the existence of a good electrical contact between the photoabsorber and the back contact.

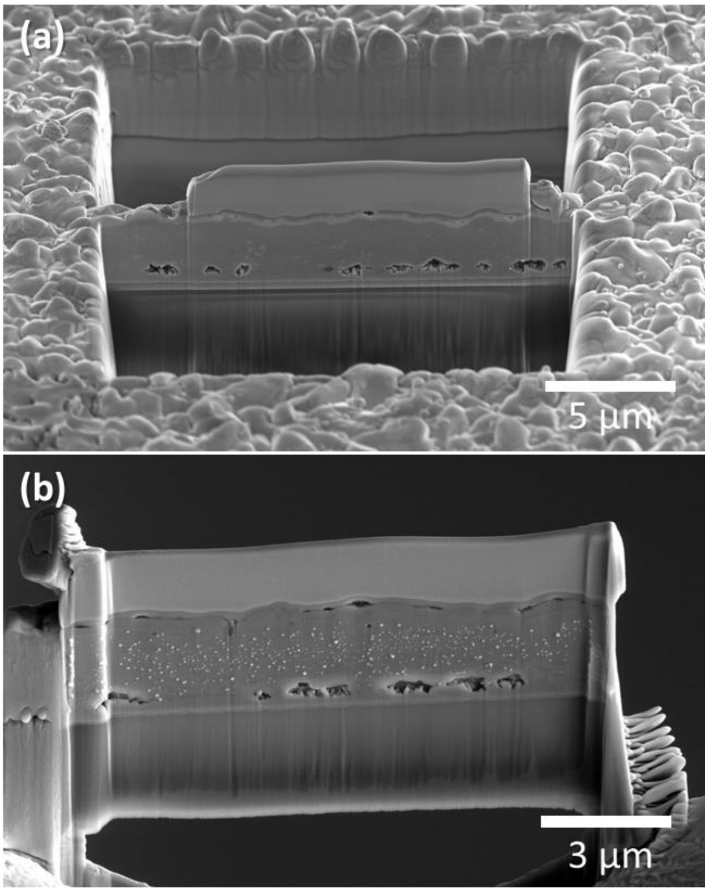

Figure 3.4. SEM imaging of the FIB prepared lamella comprising the SLG/FTO/CIGSe/CdS/*i*–ZnO/AZO PV cell.

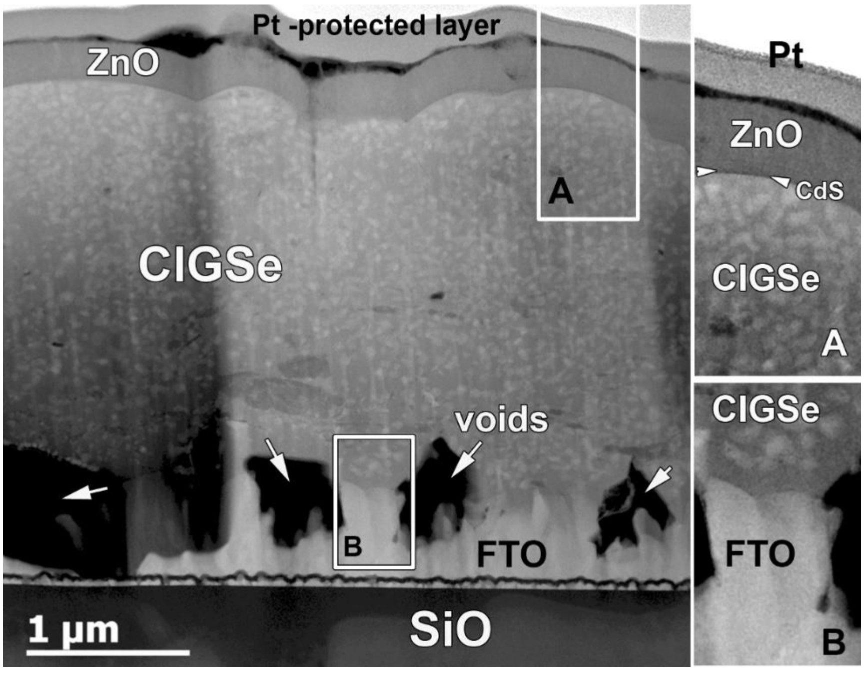

Figure 3.5. STEM imaging of the PV cell layers structure.

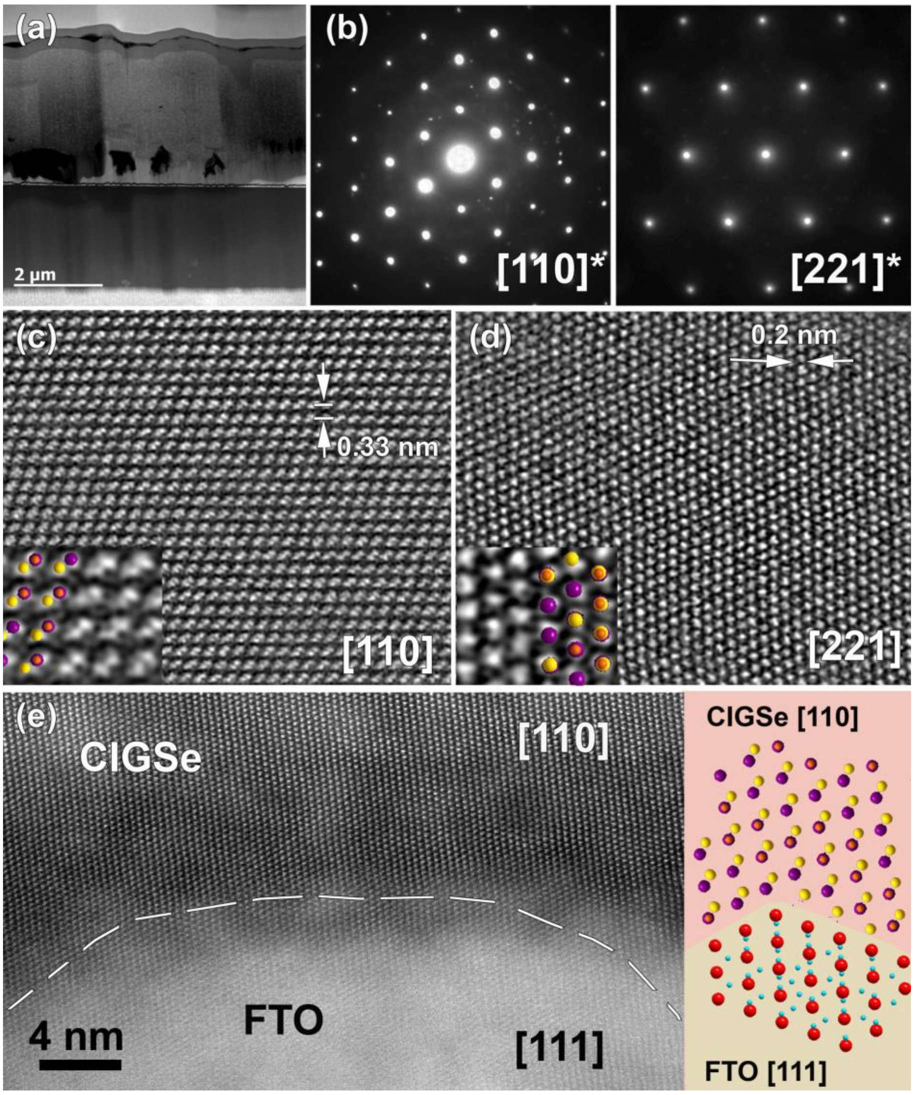

Figure 3.6. Cross-sectional HAADF–STEM image of the fabricated PV device (a). SAED patterns along the [110] and [221] zone axes of selected CIGSe grains (b) and the corresponding HAADF–STEM images along the [110] and [221] zone axes. Enlargement images with overlaid structural model are given as inset (purple atoms: In/Ga, orange: Cu and yellow: Se) (c, d). HAADF–STEM image of the interface between FTO and CIGSe, demonstrating nearly epitaxial growth of [110] CIGSe on [111] FTO together with the corresponding structural model (red: Sn, blue: O) (e).

Finally, the PV performance of the ten produced devices were evaluated through the obtained *J–V* curves (Figure 3.7 and Table 3.1). The champion PV cell exhibits an efficiency of 6.1%, a J_{sc} of 36.8 $\mathrm{mA\ cm^{-2}}$, V_{oc} of 0.31 V, and FF of 53.8%. Importantly, the *J–V* curves after few weeks gave nearly identical performance, marking the stability of the produced PV device (Figure 3.8). The resultant high J_{sc} of the device can be correlated with the low bandgap (1.04 eV) obtained for the CIGSe photoabsorber layer. As for V_{oc}, a significantly reduced value, comparing with high performance CIGSe [15] was measured, which was attributed to recombination losses and to the low bandgap. Regarding FF, it can be assumed that the series resistance is dominating the losses on this parameter, which could be related to interface problems between the back contact and the photoabsorber, such as the presence of voids.

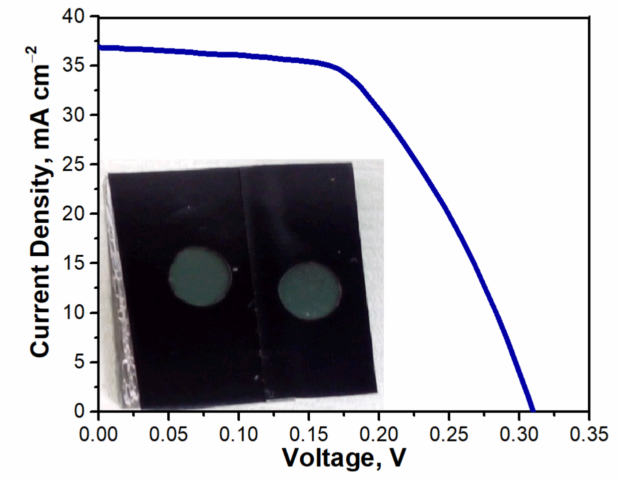

Figure 3.7. *J–V* curve of the as-fabricated champion PV device reaching 6.1% of efficiency, J_{sc} of 36.8 $mA\ cm^{-2}$, V_{oc} of 0.31 V and FF of 53.8% (on inset is a picture of PV device).

Table 3.1. Average and standard deviation of the obtained efficiency, FF, J_{sc} and V_{oc} of the ten produced PV cells.

Sample	Efficiency (%)	FF (%)	J_{sc} (mA cm^{-2})	V_{oc} (V)
1	1.8	31.9	32.9	0.23
2	1.7	28.9	27.5	0.22
3	1.9	35.2	18.9	0.27
4	1.8	33.4	20.5	0.25
5	1.5	27.2	17.3	0.30
6	2.2	34.4	21.2	0.31
7	3.0	33.0	29.6	0.31
8	3.2	32.4	32.8	0.30
9	5.5	46.4	35.2	0.34
10	6.1	53.8	36.8	0.31
Average	2.9	35.7	27.3	0.28
Standard Deviation	1.6	7.8	6.9	0.04

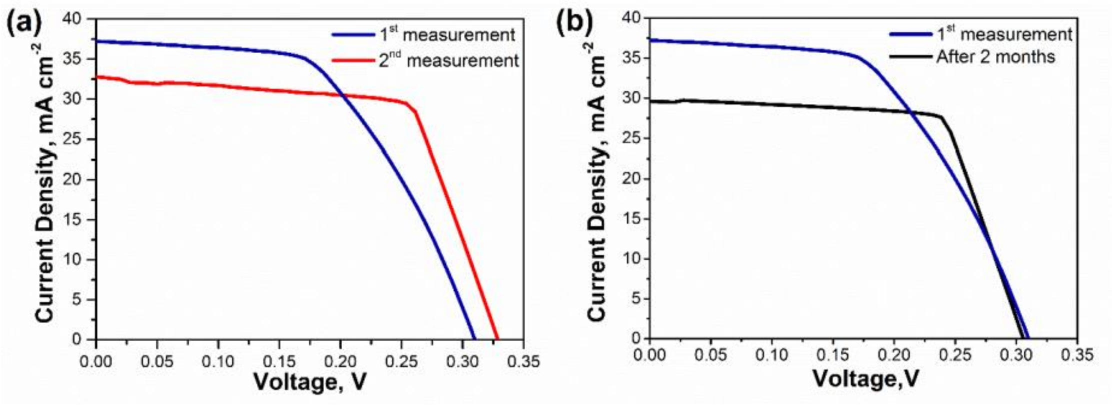

Figure 3.8. *J–V* curves of champion PV cell recorded on the same day (a). *J–V* curves of champion PV cell measured on the day of fabrication and after two months (b).

To better understand the arrangement of the layers inside the PV cell, the cross-sectional chemical composition and the distribution of all elements was analyzed by EDX mapping in STEM mode (Figure 3.9). STEM–EDX mapping confirms the stack of all layers in the produced PV cell, namely SLG/FTO/CIGSe/CdS/*i*-ZnO/AZO. Starting from the top, the presence of In is detected in the CdS layer, resulting on a buffer layer with CdS+In composition.

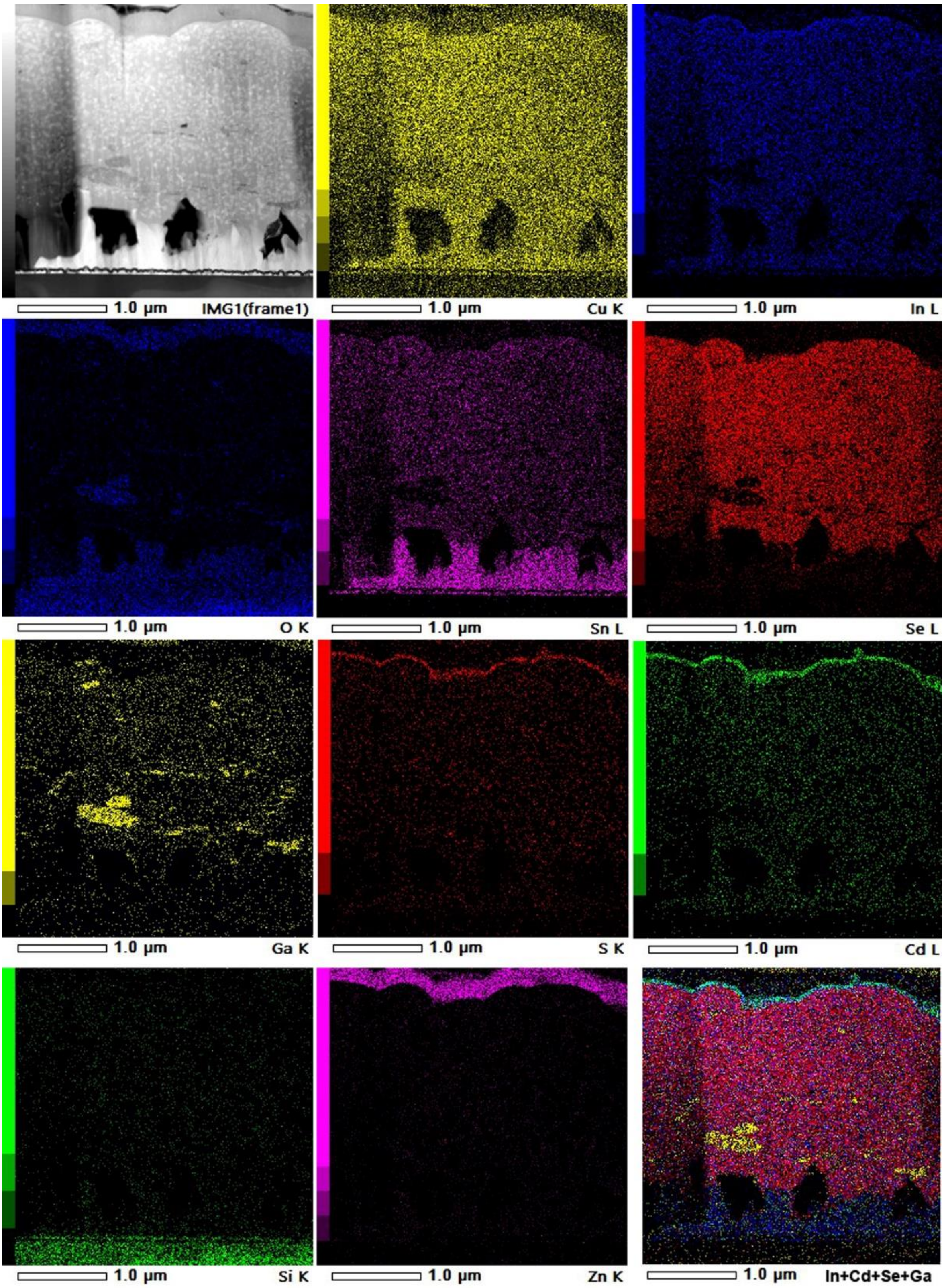

Figure 3.9. Cross-section HAADF–STEM imaging of the FTO/CIGSe/CdS/*i*–ZnO/AZO PV device, together with the simultaneously collected EDX maps of Cu, In, O, Sn, Se, Ga, S, Cd, Si and Zn, as well as In, Cd, Se and Ga mixture.

Furthermore, the distribution of Ga within the CIGSe photoabsorber was found to be markedly inhomogeneous, showing the existence of segregated Ga–O inclusions within the photoabsorber layer (Figure 3.10). Since the ink formulation comprises commercial CuO and $\mathrm{In_2O_3}$ nanopowders and polycrystalline $\mathrm{Ga_2O_3}$ as precursors ($\mathrm{Ga_2O_3}$ nanopowder is not commercially available), it seems that even after wet bead milling, the size of $\mathrm{Ga_2O_3}$ is not reduced down to nanometer size, thus resulting in the existence of not fully reacted Ga–O segregations in the CIGSe layer due to the low reactivity of the relatively large particles. Accordingly, the lack of a sufficient amount of Ga in the CIGSe layer could contribute to its reduced band gap value and accordingly low V_{oc} [16]. In addition, the presence of Ga–O phase inclusions in the CIGSe layer can be considered as recombination centers for holes and electrons, thus lowering the overall PV device performance.

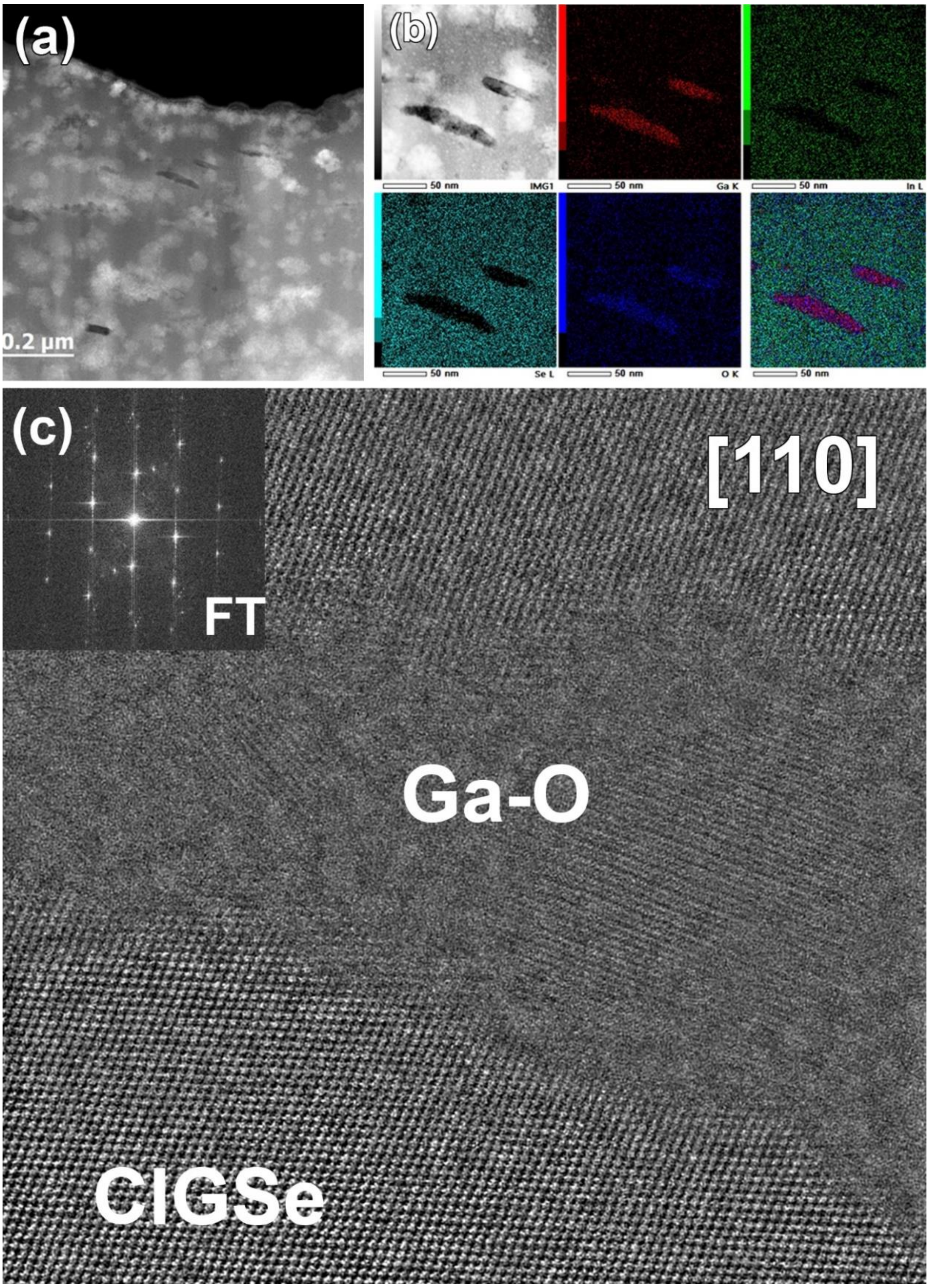

Figure 3.10. Cross-sectional low-magnification HAADF–STEM imaging of FTO/CIGSe/CdS/*i*–ZnO/AZO PV device, showing inclusions of unreacted Ga–O phase (a). Enlargement of the inclusions, together with the simultaneously collected EDX maps of Ga, In, Se and O elements and their mixture, confirming the existence of Ga–O inclusions within the CIGSe layer (b). High-resolution transmission electron microcopy (HRTEM) image of the CIGSe photoabsorber layer along the [110] zone axis, showing the presence of partially crystalline Ga–O phase (c).

Interestingly, from Figure 3.9, the migration of tin from FTO into the CIGSe layer is clearly observed, resulting in an intermixing of Sn, Cu, and In at the FTO/CIGSe interface. This migration most probably occurs during the selenization process and leads to the formation of the aforementioned void defects at the interface between the photoabsorber and back contact [14]. Such modification of the FTO back contact possibly gives rise to rear interface recombination, hence, lowering the V_{oc} and the device performance [4]. Moreover, the interface recombination also gives rise to moderate FF as a result of high series resistance, suggesting that further improvements of the photoabsorber-back contact interface should be conducted to avoid recombination losses and associated high series resistance [4, 17-19].

3.4 Conclusions

A robust printing-based method for the fabrication of CIGSe PV cells has been described. Notably, an oxide ink formulation screen-printed with further calcination and selenization gave access to ≈2 µm thick polycrystalline CIGSe photoabsorber layer grown on top of FTO/SLG substrates. One of the key points of this approach is that the oxide reduction and selenization have been conducted in a single step. After deposition of the buffer and window layers, the final SLG/FTO/CIGSe/CdS/*i*-ZnO/AZO PV cell exhibited 6.1% efficiency.

Moreover, the conducted research showed that the PV properties are strongly influenced by the interface recombination due to the compositional and microstructural variation within the PV device. This suggests that improvements should be performed to enhance the device performance, for instance by optimizing the photoabsorber-back contact interface, as well as, the chemical composition of the CIGSe phase.

Finally, the demonstrated feasibility of the screen printing process using oxides ink formulation will inspire new research efforts for the production of all-solution-processed CIGSe PV with cost-effective methodologies.

3.5 References

1. Nakamura, M., et al., *Cd-Free $Cu(In,Ga)(Se,S)_2$ Thin-Film Solar Cell With Record Efficiency of 23.35%.* IEEE Journal of Photovoltaics, 2019. **9**: p. 1863-1867.
2. Roux, F., et al., *Chalcopyrite thin-film solar cells by industry-compatible ink-based process.* Solar Energy Materials and Solar Cells, 2013. **115**: p. 86-92.
3. Zhang, T., et al., *High efficiency solution-processed thin-film $Cu(In,Ga)(Se,S)_2$ solar cells.* Energy & Environmental Science, 2016. **9**(12): p. 3674-3681.

4. Pulgarín-Agudelo, F.A., et al., *A thermal route to synthesize photovoltaic grade Cu$InSe_2$ films from printed CuO/In_2O_3 nanoparticle-based inks under Se atmosphere.* Journal of Renewable and Sustainable Energy, 2013. **5**(5): p. 053140.
5. Kapur, V.K., et al., *Non-vacuum processing of Cu$In_{1-x}Ga_xSe_2$ solar cells on rigid and flexible substrates using nanoparticle precursor inks.* Thin Solid Films, 2003. **431-432**: p. 53-57.
6. Lee, E., et al., *Nearly carbon-free printable CIGS thin films for solar cell applications.* Solar Energy Materials and Solar Cells, 2011. **95**(10): p. 2928-2932.
7. Rosen, Y., et al., *Thin Copper Flakes for Conductive Inks Prepared by Decomposition of Copper Formate and Ultrafine Wet Milling.* Advanced Materials Technologies, 2019. **4**(1): p. 1800426.
8. Zhang, C., et al., *Influence of heating temperature of Se effusion cell on Cu(In, Ga)Se_2 thin films and solar cells.* Vacuum, 2017. **141**: p. 89-96.
9. Cheng, K., et al., *Optimization of Post-selenization Process of Co-sputtered CuIn and CuGa Precursor for 11.19% Efficiency Cu(In, Ga)Se_2 Solar Cells.* Journal of Electronic Materials, 2017. **46**(4): p. 2512-2520.
10. Yan, Y., et al., *Cu(In,Ga)Se_2 thin films annealed with $SnSe_2$ for solar cell absorber fabricated by magnetron sputtering.* Solar Energy, 2017. **155**: p. 601-607.
11. Rincón, C. and F.J. Ramírez, *Lattice vibrations of Cu$InSe_2$ and Cu$GaSe_2$ by Raman microspectrometry.* Journal of Applied Physics, 1992. **72**(9): p. 4321-4324.
12. Witte, W., R. Kniese, and M. Powalla, *Raman investigations of Cu(In,Ga)Se_2 thin films with various copper contents.* Thin Solid Films, 2008. **517**(2): p. 867-869.
13. Ramanujam, J. and U.P. Singh, *Copper indium gallium selenide based solar cells – a review.* Energy & Environmental Science, 2017. **10**(6): p. 1306-1319.
14. Jiang, J., et al., *10.3% Efficient CuIn(S,Se)$_2$ Solar Cells from DMF Molecular Solution with the Absorber Selenized under High Argon Pressure.* Solar RRL, 2018. **2**(6): p. 1800044.
15. Kato, T., et al., *Record Efficiency for Thin-Film Polycrystalline Solar Cells Up to 22.9% Achieved by Cs-Treated Cu(In,Ga)(Se,S)$_2$.* IEEE Journal of Photovoltaics, 2019. **9**(1): p. 325-330.
16. Kim, B. and B.K. Min, *Strategies toward highly efficient CIGSe thin-film solar cells fabricated by sequential process.* Sustainable Energy & Fuels, 2018. **2**(8): p. 1671-1685.
17. López-García, J., et al., *Synthesis of CuIn(S,Se)$_2$ quaternary alloys by screen printing and selenization-sulfurization sequential steps: Development of composition graded absorbers for low cost photovoltaic devices.* Materials Chemistry and Physics, 2015. **160**: p. 237-243.
18. Nakane, A., et al., *Quantitative determination of optical and recombination losses in thin-film photovoltaic devices based on external quantum efficiency analysis.* Journal of Applied Physics, 2016. **120**(6): p. 064505.
19. Cui, Y., et al., *Efficient hybrid solution strategy to fabricate Cu(In,Ga)(S,Se)$_2$ solar cells.* Journal of Alloys and Compounds, 2017. **696**: p. 884-890.

Section II

Sustainable methodologies for solution-processed CIGSe photovoltaic systems

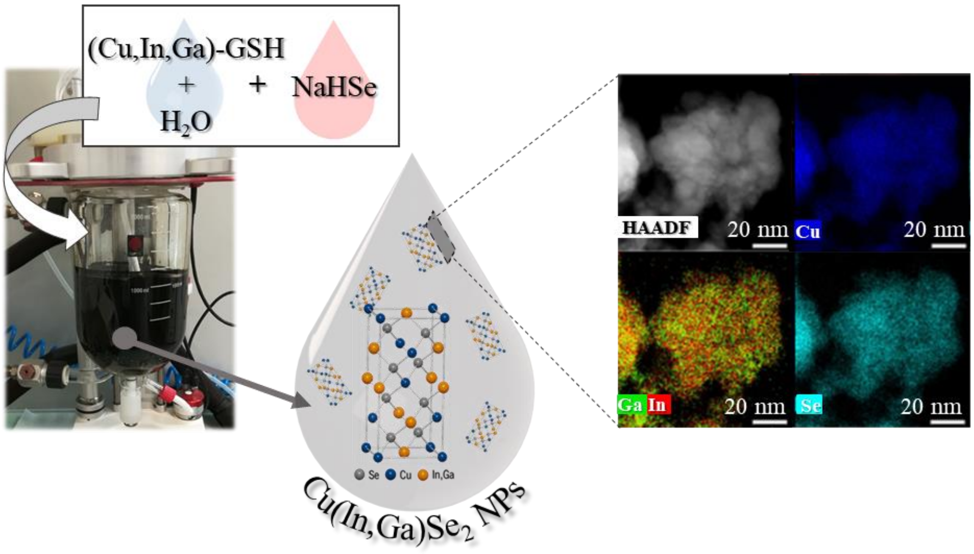

Chapter 4. Large-scale aqueous synthesis of $Cu(In,Ga)Se_2$ nanoparticles

Environmentally friendly, selenization-free synthesis of $\mathrm{Cu(In,Ga)Se_2}$ nanoparticles is pivotal to allow for a more sustainable production of the photovoltaic devices. To this end an aqueous synthesis of $\mathrm{Cu(In,Ga)Se_2}$ nanoparticles has been addressed, followed by annealing, to give access to phase-pure $\mathrm{Cu(In,Ga)Se_2}$ crystals with chalcopyrite tetragonal structure and no signs of secondary phases. Morphological and compositional characterization revealed nanoparticles with 10–35 nm of size and uniform distribution of Cu, In, Ga, and Se metals. In addition, the first aqueous large-scale synthesis of $\mathrm{Cu(In,Ga)Se_2}$ NPs has been successfully achieved by up-scaling the synthesis procedure, resulting in 5 g of nanoparticles with [Cu]/[In + Ga] ≈ 0.8 and [Ga]/[Ga + In] ≈ 0.3 metal ratio, with excellent crystallinity, and ideal optical band gap of ≈1.14 eV.

This chapter is based on the following publication: **B. F. Gonçalves**, A. P. LaGrow, G. Botelho, L. M. Salonen, S. Lanceros-Méndez, and Y. V. Kolen'ko, *Large-scale aqueous synthesis of* $Cu(In,Ga)Se_2$ *nanoparticles,* Submitted 2021.

4.1 Introduction

The unique structural and opto-electronic characteristics of CIGSe *p*-type semiconductor, render CIGSe PV devices highly promising and under constant optimization [1]. Recently, the preparation of CIGSe photoabsorber thin films by printing has been explored. However, successful procedures rely mainly on the use of toxic solvents during synthesis and/or ink formulation, and typically require a selenization treatment [2], which releases harmful $\mathrm{H_2Se}$ vapors.

The use of NPs to produce CIGSe thin films allows for both a higher control of the film quality and omission of the selenization treatment. These NPs are mostly synthesized using heat-up [3, 4], solvothermal [5, 6], or hot-injection [7] methods, which employ toxic organic solvents and capping ligands at elevated temperatures. Notably, a few sustainable approaches to produce quaternary CIGSe NPs have been reported, including microwave-assisted solvent-free synthesis [8] and sonochemical method using ethanol [9]. On the other hand, ternary CISe NPs [10, 11] and quantum dots [12] for PVs have been prepared by aqueous synthesis.

Notably, this work presents a novel water-based route to phase-pure CIGSe NPs. Scale-up of the synthesis protocol afforded 5 g of phase-pure NPs with [Cu] / [In + Ga] ≈ 0.8 and [Ga] / [Ga + In] ≈ 0.3 metal ratio and optimal optical band gap of 1.14 eV. The herein reported environmentally friendly synthesis provides easy access to chalcogenide NPs compatible with ink formulation for printing deposition processes.

4.2 Experimental

4.2.1 Chemicals

$\mathrm{Cu(NO_3)_2 \cdot 3H_2O}$ (99%, Acros Organics), $\mathrm{In(NO_3)_3 \cdot xH_2O}$ (99.99%, Sigma-Aldrich), $\mathrm{Ga(NO_3)_3 \cdot xH_2O}$ (99.99%, Sigma-Aldrich), L-glutathione reduced (GSH, ≥98.0%, Sigma-Aldrich), $\mathrm{NaBH_4}$ (99.99%, Sigma-Aldrich), selenium powder (100 mesh, ≥99.5%, Sigma-Aldrich), and IPA (≥99.8%, Honeywell) were purchased and used as received. Ultrapure water (MQ water) was obtained using a MQ Advantage A10 system (Millipore).

4.2.2 Aqueous synthesis of Cu(In,Ga)Se_2 nanoparticles

CIGSe NPs were prepared by modifying previously reported procedures [11, 12], targeting a nominal ratio of $\mathrm{Cu_{0.8}In_{0.7}Ga_{0.3}Se_2}$. The synthesis was conducted by first dissolving the metal precursors,

$\mathrm{Cu(NO_3)_2 \cdot 3H_2O}$ (1.65 mmol), $\mathrm{In(NO_3)_3 \cdot xH_2O}$ (1.89 mmol), and $\mathrm{Ga(NO_3)_3 \cdot xH_2O}$ (1.13 mmol) in 300 mL of MQ water at RT in a three-necked round-bottom flask. After complete dissolution, indicated by a light blue clear solution, GSH (1.65 mmol) was added and the solution was stirred under $\mathrm{N_2}$ at RT. Separately, and also under $\mathrm{N_2}$, $\mathrm{NaBH_4}$ (12.8 mmol) was dissolved in 50 mL of MQ water and added to a two-necked round-bottom flask containing Se powder (6.4 mmol) for NaHSe formation according to the following chemical reaction (Equation 4.1).

$$\mathrm{4NaBH_4 + 2Se + 7H_2O = 2NaHSe + N_2B_4O_7 + 14H_2} \tag{4.1}$$

Then, the temperature of the solution was raised to 80 °C and the mixture was stirred for 30 min. The final clear red solution was cooled to RT and rapidly injected to the Cu/In/Ga-GSH aqueous solution, producing an immediate change of color to brown. After agitation at RT for 10 min, the reaction mixture was heated to 90 °C and stirred at this temperature for 2 h. The resulting colloidal dark solution was let for natural cooling to RT, followed by the addition of IPA (100 mL) to precipitate the NPs. Finally, the NPs were collected and washed several times with IPA by centrifugation (9000 rpm, 10 min) followed by drying under vacuum for 24 h.

The as-synthesized product was annealed inside a quartz tubular furnace (Lenton, Eurotherm) at 500 °C using a heating rate of 10 $\mathrm{°C\ min^{-1}}$ and held at this temperature for 1 h under $\mathrm{N_2}$ flow for a complete crystallization.

4.2.3 Upscaled synthesis of Cu(In,Ga)Se$_2$ nanoparticles

The large-scale synthesis was conducted in an automated synthesis system (Atlas Potassium, Syrris). $\mathrm{Cu(NO_3)_2 \cdot 3H_2O}$ (8.26 mmol), $\mathrm{In(NO_3)_3 \cdot xH_2O}$ (9.46 mmol), and $\mathrm{Ga(NO_3)_3 \cdot xH_2O}$ (5.63 mmol) precursors were dissolved in 1 L of MQ water under mechanical stirring at 200 rpm in the glass reaction vessel, and followed by the addition of GSH (8.26 mmol). In a separate two-necked round-bottom flask, NaHSe precursor solution was prepared by reacting $\mathrm{NaBH_4}$ (64.1 mmol) with Se powder (32.1 mmol) in 100 mL of water. Next, NaHSe was rapidly injected into Cu/In/Ga–GSH aqueous solution and, after 10 min of agitation, the reaction mixture was heated to 90 °C and stirred at this temperature for 2 h. Precipitation of the product was conducted using 300 mL of IPA and the NPs were collected and washed using the above-mentioned procedure.

4.2.4 Characterization

X-ray diffraction:

The phase composition of the synthesized NPs was analyzed by XRD and the average crystallite size was estimated as described on Chapter 2 (section 2.2.5).

Thermogravimetric analysis:

The thermal behavior of the aqueous-synthesized NPs was studied by TGA as described on Chapter 2 (section 2.2.5).

Electron microscopy:

The morphology, microstructure and chemical composition of the NPs was analyzed by SEM as described on Chapter 2 (section 2.2.5).

Optical properties:

UV-Vis-NIR optical measurements and the band gap determination were carried out as described on Chapter 2 (section 2.2.5).

4.3 Results and Discussion

4.3.1 Aqueous synthesis of $Cu(In,Ga)Se_2$ nanoparticles

Aqueous syntheses have major advantages from the industrial point of view since water is abundant, safe, non-expensive, non-flammable, and requires low energy amount to conduct reactions, due its boiling point. However, when conducting syntheses in water, the amount of available oxygen in the aqueous medium can induce oxidation of metals. In the case of CIGSe, the presence of Cu^{+} ions is more desirable than that of Cu^{2+}, since CuSe intermediate phases have higher mobility and require lower energy for the conversion into CIGSe end product [13]. Therefore, this CIGSe NP synthesis comprises the dissolution of Cu^{2+}, In^{3+}, and Ga^{3+} precursors in water in the presence of natural antioxidant GSH as complexing agent for Cu^{2+} to reduce it to Cu^{+}, which was found to be essential to obtain phase-pure CIGSe. Reaction between the freshly prepared Se^{2-} precursor NaHSe (Equation 4.2) and the solution of metal salts (Equation 4.3) delivered 1 g of CIGSe NPs with 87% yield.

$$\mathrm{4NaBH_4 + 2Se + 7H_2O = 2NaHSe + N_2B_4O_7 + 14H_2} \tag{1}$$

$$\mathrm{0.83Cu(NO_3)_2{\bullet}3H_2O + 0.7In(NO_3)_3{\bullet}xH_2O + 0.3Ga(NO_3)_3{\bullet}xH_2O + GSH + 2NaHSe + H_2O = Cu_{0.83}(In_{0.7}Ga_{0.3})Se_2} \tag{2}$$

Due to an incomplete crystallization detected by XRD analysis of the as-synthesized product (Figure 4.1a), subsequent annealing at 500 °C under $\mathrm{N_2}$ was employed, resulting in highly crystalline CIGSe NPs (Figure 4.1a). The annealing temperature selection was based on the TG curve of the NPs from aqueous synthesis (Figure 4.2), which reveals a multi-stage decomposition process with 35% weight loss mostly stemming from side-products and GSH degradation [14] below 500 °C.

The resultant annealed product correspond to phase-pure CIGSe with tetragonal chalcopyrite structure (space group *I*–42*d*) with no signs of undesirable secondary phases (Figure 4.1a). Prominent peaks found at 26.8, 44.6, and 52.8° correspond to the (112), (204/220), and (312/116) planes of the CIGSe phase [15, 16], respectively. The crystallite size of the NPs was estimated using Scherrer formula, revealing an average size of 23±9 nm. The phase purity was further confirmed by Raman spectroscopy (Figure 4.1b), with a spectrum showing no signs of typical $\mathrm{CuSe_2}$ secondary phase, usually emerging at 260 $\mathrm{cm^{-1}}$. This admixture phase is detrimental for PVs, since it functions as a recombination center for charge carriers [17]. Importantly, the presence of a sharp band at 174 $\mathrm{cm^{-1}}$ and two broader bands at 127 and 213 $\mathrm{cm^{-1}}$ was identified, corresponding to A_1, B_2, and B_2/E vibrational modes of CIGSe [17, 18], respectively. EDX spectroscopy on SEM imaging revealed chemical composition of $\mathrm{Cu_{0.86}(In_{0.73})Ga_{0.33}Se_2}$ (Figure 4.1c, d), which agrees fairly well with the initial targeted ratio and the metal ratio used in high-efficiency PVs.

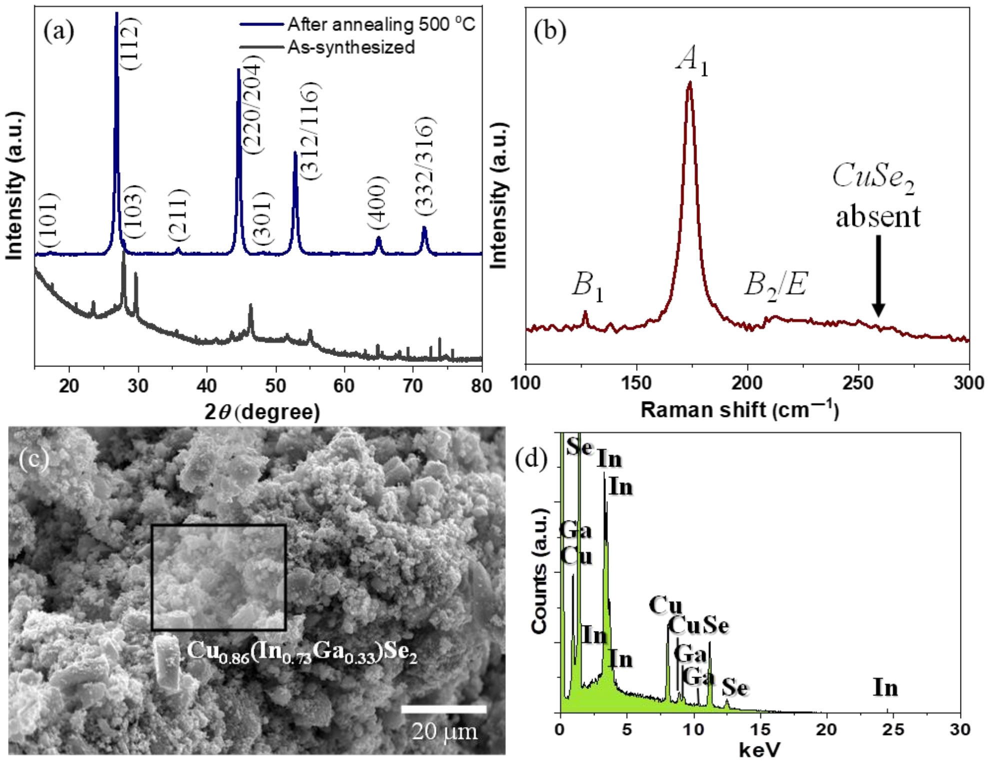

Figure 4.1. Structural and compositional characterization of the synthesized CIGSe NPs as-synthesized (gray line) and after annealing (blue line): XRD patterns (*hkl* peak assignment is based on ICDD card no. 00-066-0140 for tetragonal CIGSe) (a), Raman spectrum of the CIGSe NPs obtained after annealing (b), as well as SEM image (c) together with the corresponding EDX spectrum from the annealed product (d).

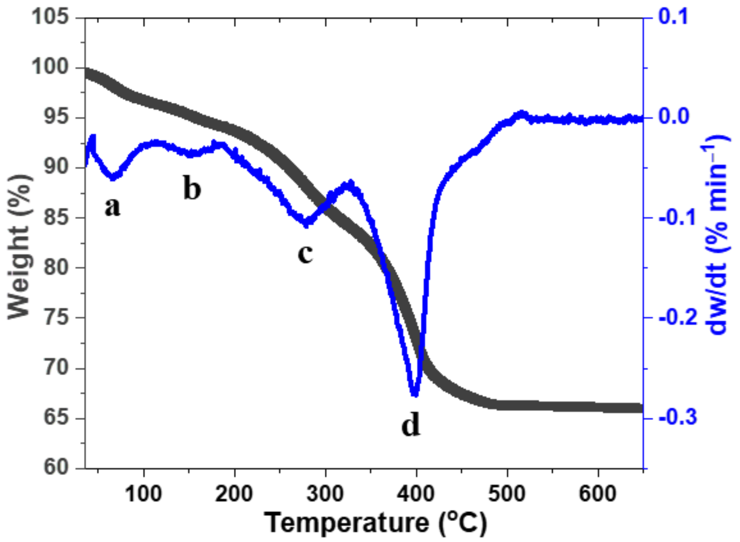

Figure 4.2. TGA with the respective derivative curve for the aqueously synthesized NPs under Ar, a: 66 °C, b: 151 °C, c: 278 °C, and d: 399 °C.

HAADF–STEM imaging (Figure 4.3a, b) of the NPs viewed along the [111] zone axis confirmed the CIGSe chalcopyrite crystal structure, with the respective 3.3 Å (112) and 2.0 Å (220) lattice spacings evident (Figure 4.3c). Moreover, the observed STEM–EDX maps (Figure 4.3d) revealed a uniform distribution of Cu, In, Ga, and Se through the NPs and the presence of NP agglomeration with heterogeneous size distribution, stemming from the aggregation during annealing. Importantly, no secondary phases were detected, confirming the phase purity of these NPs.

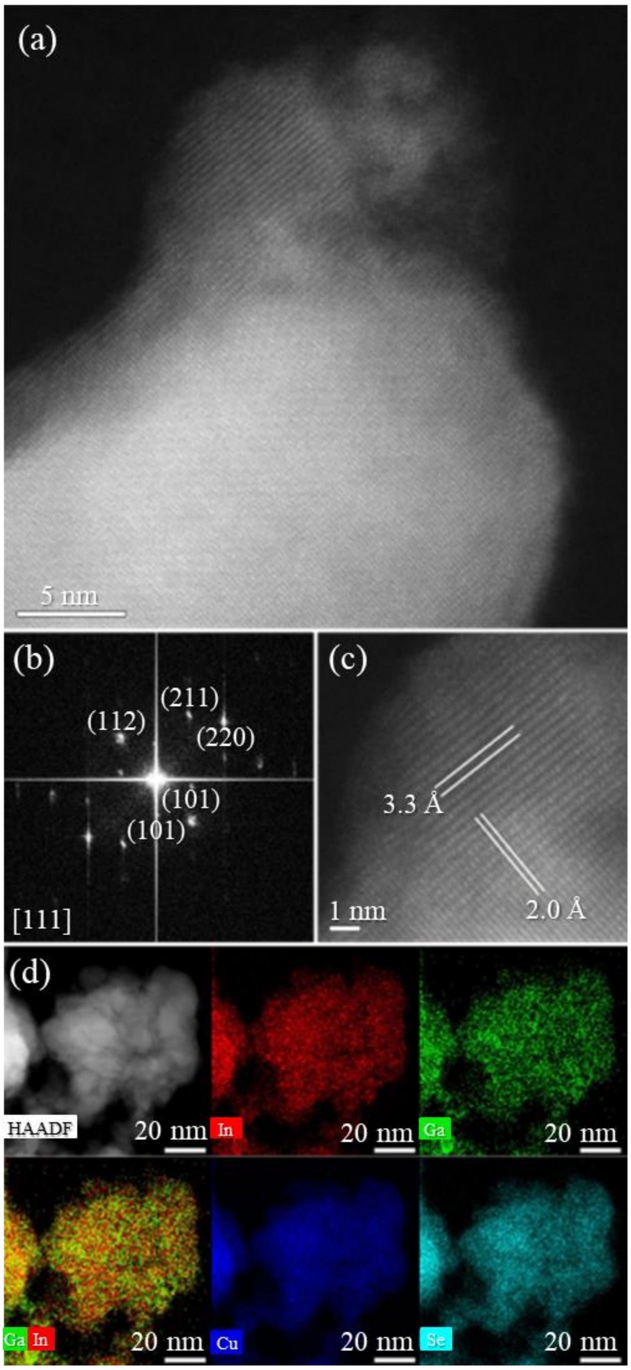

Figure 4.3. HAADF–STEM images (a, c), fast Fourier transform pattern (b) and STEM–EDX maps (d) for CIGSe NPs aqueously synthesized followed by annealing.

4.3.2 Upscaled synthesis of Cu(In,Ga)Se$_2$ nanoparticles

The printing of photoabsorber thin films requires a considerable amount of NPs, and therefore, the development of robust scale-up synthesis procedures is essential. Accordingly, the aqueous CIGSe NP synthesis was successfully up-scaled (Figure 4.4a, inset), rendering 5 g of high-quality NPs after annealing with an excellent yield of 90%. Notably, the corresponding XRD analysis (Figure 4.4a) confirmed phase-pure CIGSe with a chalcopyrite structure, as observed for the small-scale synthesis. The crystallite size of the large-scale synthesized NPs, estimated using Scherrer formula, revealed an average of 24±11 nm. The band gap measurements (Figure 4.4b) revealed a band gap of 1.13±0.02 and 1.14±0.02 eV for the material obtained by the 1 g and 5 g synthesis, respectively. Notably, these band gap values are close to the optimum required for PV systems, showing that the NPs synthesized herein can contribute towards the production of high-efficiency PV devices. Similarly to the 1 g scale synthesis, the scale-up procedure gave access to NPs with chemical composition of $\mathrm{Cu_{0.79}(In_{0.74}Ga_{0.33})Se_2}$ as estimated by EDX (Figure 4.4c,d).

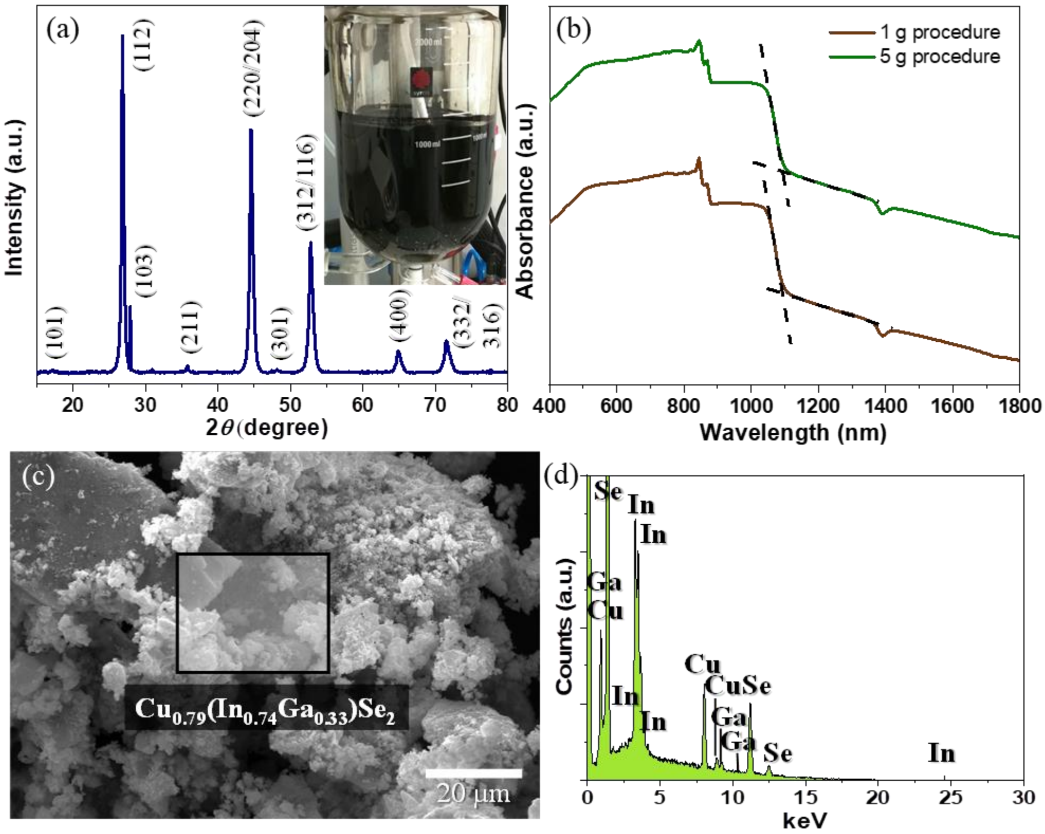

Figure 4.4. XRD pattern of the NPs (*hkl* peak assignment is based on ICDD card no. 00-066-0140 for tetragonal CIGSe) and the automated reactor vessel as inset (a), UV–Vis–NIR absorption spectra of the NPs from 1 g and 5 g syntheses (b), SEM image of the NPs (c) and corresponding EDX spectrum (d) for annealed CIGSe obtained by the large-scale synthesis.

Notably, this is the first aqueous large-scale synthesis of CIGSe NPs. The high-quality NPs synthesized have great potential to produce high-performance CIGSe PV devices. For that purpose, the dispersion of these NPs in water-based solutions is recommended for ink formulation followed by deposition of thin films on top of conductive substrates through printing processes. To improve the crystallinity of the films an annealing treatment is also strongly recommended.

4.4 Conclusions

An environmentally friendly aqueous synthesis delivered phase-pure chalcopyrite CIGSe NPs with 10–35 nm of size. Moreover, a scale-up procedure successfully delivered 5 g of NPs with equally high crystallinity, chemical composition of $\mathrm{Cu_{0.79}(In_{0.74}Ga_{0.33})Se_2}$, and band gap of 1.14 eV, ideal to be employed in the printing of CIGSe photoabsorber thin films. These findings contribute to the development of solution-processed CIGSe PVs, providing a sustainable approach to substitute inconvenient selenization procedures usually required for these devices.

4.5 References

1. Ramanujam, J. and U.P. Singh, *Copper indium gallium selenide based solar cells – a review.* Energy & Environmental Science, 2017. **10**(6): p. 1306-1319.
2. Liang, H., et al., *CIGS formation by high temperature selenization of metal precursors in* H_2Se *atmosphere.* Solid-State Electronics, 2012. **76**: p. 95-100.
3. Jia, G., et al., *Cation exchange synthesis of* $CuIn_xGa_{1-x}Se_2$ *nanowires and their implementation in photovoltaic devices.* RSC Advances, 2019. **9**(61): p. 35780-35785.
4. Yang, C.-T. and H.-I. Hsiang, *Different ligand exchange solvents effect on the densification of* $CuIn_{0.7}Ga_{0.3}Se_2$ *prepared using the heating-up method.* Applied Surface Science, 2017. **426**: p. 1148-1157.
5. Ghanbari, E., M. Zahedifar, and O. Amiri, *Optimal conditions for fabricating CIGS nanoparticles by solvothermal method.* Journal of Materials Science: Materials in Electronics, 2018. **29**(9): p. 7068-7076.
6. Huang, F., et al., *CIS and CIGS nanomaterials prepared by solvothermal method and their spectral properties.* Crystal Research and Technology, 2014. **49**(12): p. 953-958.
7. Latha, M., R. Aruna Devi, and S. Velumani, *Hot injection synthesis of* $Cu(In, Ga)Se_2$ *nanocrystals with tunable bandgap.* Optical Materials, 2018. **79**: p. 450-456.
8. Al Juhaiman, L., et al., *Green synthesis of tunable* $Cu(In_{1-x}Ga_x)Se_2$ *nanoparticles using non-organic solvents.* Green Chemistry, 2010. **12**(7): p. 1248-1252.
9. Le, T.T.T., et al., *Green and low-cost preparation of CIGSe thin film by a nanocrystals ink based spin-coating method.* Korean Journal of Chemical Engineering, 2019. **36**(12): p. 2110-2117.
10. Li, S.-n., et al., *Synthesis of chalcopyrite-type* $CuInSe_2$ *nanoparticles from aqueous solution at room temperature.* Materials Letters, 2013. **101**: p. 51-53.

11. Shim, J., et al., *Synthesis and Characterization of CIS Nanoparticle Ink for Low-Cost Thin Film Solar Cells.* Journal of Nanoscience and Nanotechnology, 2014. **14**(12): p. 9279-9284.
12. Fan, X.-B., et al., *Nonstoichiometric* Cu_xIn_yS *Quantum Dots for Efficient Photocatalytic Hydrogen Evolution.* ChemSusChem, 2017. **10**(24): p. 4833-4838.
13. Latha, M., et al., *Solution based synthesis of* $Cu(In,Ga)Se_2$ *microcrystals and thin films.* RSC Advances, 2019. **9**(60): p. 35197-35208.
14. Farrag, M., *Preparation, characterization and photocatalytic activity of size selected platinum nanoclusters.* Journal of Photochemistry and Photobiology A: Chemistry, 2016. **318**: p. 42-50.
15. Der Wu, J., L. Ting Wang, and C. Gau, *Synthesis of* $CuInGaSe_2$ *nanoparticles by modified polyol route.* Solar Energy Materials and Solar Cells, 2012. **98**: p. 404-408.
16. Chun, Y.G., K.H. Kim, and K.H. Yoon, *Synthesis of* $CuInGaSe_2$ *nanoparticles by solvothermal route.* Thin Solid Films, 2005. **480-481**: p. 46-49.
17. Choi, I.-H., *Raman spectroscopy of* $CuIn_{1-x}Ga_xSe_2$ *for in-situ monitoring of the composition ratio.* Thin Solid Films, 2011. **519**(13): p. 4390-4393.
18. Rincón, C. and F.J. Ramírez, *Lattice vibrations of* $CuInSe_2$ *and* $CuGaSe_2$ *by Raman microspectrometry.* Journal of Applied Physics, 1992. **72**(9): p. 4321-4324.

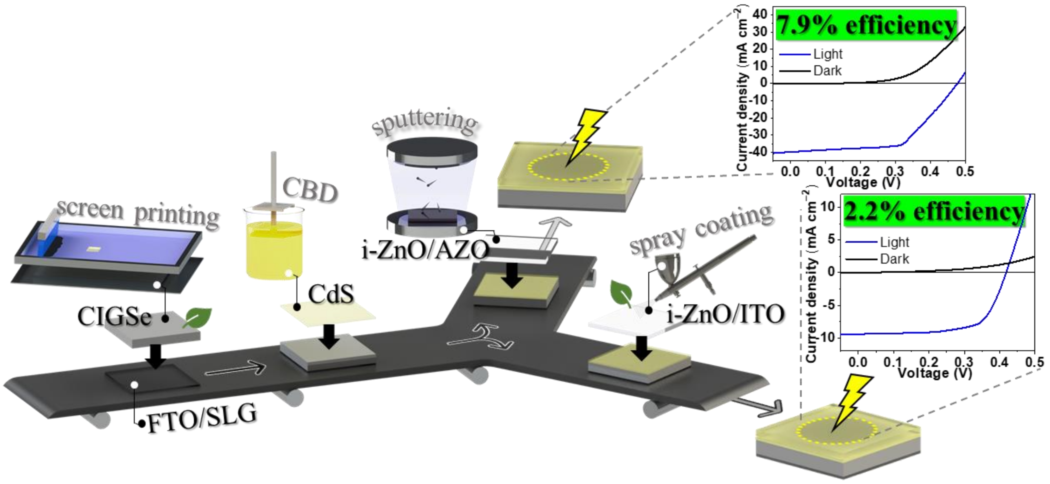

Chapter 5. Towards all-non-vacuum processed photovoltaic systems: water-based screen-printed $Cu(In,Ga)Se_2$ photoabsorber with 7.9% of efficiency

During the last decades, major advances have been made in photovoltaic systems based on $\mathrm{Cu(In,Ga)Se_2}$ chalcopyrite. However, the most efficient photovoltaic cells are processed with high-energy-demanding vacuum conditions. To lower the costs of high throughput production, printing/coating processes are proving to be effective solutions. However, given the societal concerns about the use of toxic chemicals and costly fabrication of functional materials and devices for photovoltaic applications, it is important to develop alternative sustainable methodologies. Thus, to enrich the field of printed $\mathrm{Cu(In,Ga)Se_2}$ photovoltaics, this chapter presents a combination of printing, coating, and chemical bath deposition processes for the fabrication of photoabsorber, buffer, and transparent conductive layers. In a sustainable approach, all inks have been formulated using water and ethanol as solvents. Screen printing of the photoabsorber on fluorine-doped tin oxide coated glass followed by selenization, further chemical bath deposition of cadmium sulfide buffer, and final sputtering of intrinsic zinc oxide and aluminum-doped zinc oxide top conductive layers delivered a 7.9% maximum efficiency device, a record for screen-printed $\mathrm{Cu(In,Ga)Se_2}$ photovoltaic cells. On the other hand, an all-non-vacuum processed device with spray-coated intrinsic zinc oxide and tin-doped indium oxide top conductive layers delivered 2.2% of efficiency. The given approaches represent a relevant step towards the fabrication of sustainable and efficient $\mathrm{Cu(In,Ga)Se_2}$ photovoltaic systems.

This chapter is based on the following publication: **B. F. Gonçalves**, G. Botelho, S. Lanceros-Méndez, and Y. V. Kolen'ko, *Eco-friendly and Cost-efficient Inks for Screen-printed Fabrication of Copper Indium Gallium Diselenide Photoabsorber Thin Films,* Journal of Colloid & Interface Science, 598, 388-397, 2021, and **B. F. Gonçalves**, V. Sousa, J. Virtuoso, E. Modin, O. I. Lebedev, G. Botelho, S. Sadewasser, L. M. Salonen, S. Lanceros-Méndez, and Y. V. Kolen'ko, *Towards All-non-vacuum Processed Photovoltaic Systems: Water-based Screen-printed Cu(In,Ga)Se$_2$ Photoabsorber with 7.9% Efficiency,* Submitted 2021.

5.1 Introduction

Up to date, CIGSe PV cells with efficiencies up to 17.3% have been produced using printing/coating [1] processes for the photoabsorber deposition. The faster, more practical, and in some cases easily scalable printing/coating processes, such as spin coating [1, 2], blade coating [3, 4], inkjet printing [5, 6], spray coating [7, 8], and screen printing [9] have been successfully employed in PV cell fabrication. Despite the high efficiencies obtained, ranging from 2.4% [9] to 17.3% [1], environmentally friendly photoabsorber ink formulation would improve the processes from the sustainability point of view. To this end, toxic solvents, such as hydrazine [1, 2], hexanethiol [3], ethanolamine [6] and ethylenediamine [8] have been replaced by non-toxic water and ethanol [7, 10-12] albeit with concomitant reduction in device efficiencies. On the other hand, printable transparent top conductive layers are also raising increasing interest. However, only few reports have emerged on the production of all-non-vacuum processed CIGSe PVs. The spin coating of the photoabsorber followed by CBD of the CdS layer and spin coating of the top conductive layers *i*–ZnO, AZO, and AgNW delivered PV cells with efficiencies from 1.6% [13] to 7.7% [14]. However, sustainability from the point of view of solvent toxicity has not been addressed.

This work presents the formulation of two novel and environmentally friendly inks based on commercial CuO, In_2O_3, and Ga_2O_3. Importantly, these inks display excellent dispersion of raw oxide solids and good rheological properties. The screen printing of the as-developed inks followed by the thermal treatments afford compact and phase-pure CIGSe photoabsorber thin films. Notably, the films exhibit semiconducting behavior with optical band gaps of 0.97 and 1.08 eV. Moreover, two procedures for the development of environmentally friendly CIGSe PVs comprising one of the developed high-quality photoabsorbers is also addressed. A device based on screen-printed photoabsorber layer, CBD of CdS, and vacuum-deposited top conductive layers presents a reliable performance with 7.9% of efficiency for the champion cell. The all-non-vacuum processed device featuring spray-coated *i*–ZnO and ITO top contacts delivered 2.2% of efficiency.

5.2 Experimental

5.2.1 Chemicals

Copper oxide nanopowder (CuO, ≥99%, 30–50 nm, Alfa Aesar), indium oxide nanopowder (In_2O_3, 99.9%, <100 nm, Sigma-Aldrich), gallium oxide nanopowder (Ga_2O_3, 99.9%, 80–100 nm, Nanoshel), selenium shots (Se, 99.999%, 2–6 mm, Alfa Aesar), polyvinyl alcohol polymer (PVA, 98% hydrolyzed, M_w = 13 000–23 000, Sigma-Aldrich), HPMC (2% aqueous solution, viscosity 80–120 cP, Sigma-Aldrich), 4,5-dihydroxy-1,3-benzenedisulfonic acid disodium salt monohydrate (Tiron, 97%, Sigma-Aldrich), hexadecyltrimethylammonium bromide (CTAB, ≥99%, Sigma-Aldrich), polyethylene glycol sorbitan monostearate (Tween 60, stearic acid 40–60%, Sigma-Aldrich), Disperbyk-180 (BYK180, BYK), Disperbyk-199 (BYK199, BYK), Disperbyk-2013 (BYK2013, BYK), Rheobyk-7420 ES (BYK7420 ES, BYK), BYK28 (BYK), carbon graphene paste (graphene paste, <7.5 $\Omega\ \mathrm{sq}^{-1}$, SunChemical), graphite/carbon-black paste (carbon paste, ≤25 $\Omega\ \mathrm{sq}^{-1}$, Solaronix), potassium cyanide (KCN, ≥98.0%, Sigma-Aldrich), thiourea ($\mathrm{CS(NH_2)_2}$, ≥99.0%, Sigma-Aldrich), cadmium acetate ($\mathrm{Cd(ac)_2}$, 99.995%, Sigma-Aldrich), aqueous ammonium hydroxide solution (28–30%, Acros Organics), tin-doped indium oxide 20% suspension in water (ITO, 18 nm with $\mathrm{In_2O_3/SnO_2}$ 90:10%, ≥99.0%, Sigma-Aldrich), ethanol (≥99.8%, Honeywell), acetone (≥99.5%, Honeywell), and IPA (≥99.8%, Honeywell) were used as received. Ultrapure water (18.2 MΩ cm) was generated using MQ Advantage A10 Millipore system.

5.2.2 Photoabsorber layer development

The commercial nanosized $\mathrm{Ga_2O_3}$ appeared as highly agglomerated powder and to obtain a finer $\mathrm{Ga_2O_3}$ powder, this oxide was subjected to WBM. For this purpose, 0.5 g of $\mathrm{Ga_2O_3}$ was added to a solution of Tiron (10 mg) dissolved in water (1.5 mL), and the resultant slurry was ball-milled as described on Chapter 2 (section 2.2.3). After WBM, the $\mathrm{Ga_2O_3}$ suspension was collected and filtered using a 1 µm syringe filter to narrow the size distribution. Finally, the resultant suspension was dried at 80 °C and ground in mortar. The as-prepared $\mathrm{Ga_2O_3}$ was used in the following studies.

5.2.2.1 PVA oxide ink formulation

In a 10 mL glass vial equipped with a stir bar, 12.2 mg of Tiron (2% related to the oxide solids) was dissolved in 1.5 mL of water under magnetic stirring for 20 min at RT. Then, 0.21 g of CuO, 0.31 g of $\mathrm{In_2O_3}$, and 0.09 g of $\mathrm{Ga_2O_3}$ (metal ratios: [Cu / In + Ga] = 0.83, [Ga / In + Ga] = 0.3 [15]) were added to the Tiron solution and the suspension was allowed to stir for 24 h at RT. Thereafter, 0.5 g of PVA were added to the suspension and the system was subjected to stirring at 90 °C for 12 h, followed by natural cooling to RT and subsequent addition of a drop of BYK28 defoamer to the ink. This protocol affords a homogenous and viscous PVA-based ink with 23% oxide solid content. Analysis of the surface tension and rheological properties of the ink revealed that it shows non-Newtonian behavior with a range of dynamic viscosity between 1.3–2.8 Pa s (Figure 5.1a) and a surface tension of 29±2 $\mathrm{mN\ m^{-1}}$.

5.2.2.2 HPMC oxide ink formulation

A slurry consisting of Tiron (8.1 mg), water (1.5 mL), CuO (0.14 g), In_2O_3 (0.21 g), and Ga_2O_3 (0.06 g) was subjected to WBM for 24 h. The product was collected, dried at 80 °C, and ground in a mortar. Separately, in a 10 mL glass vial equipped with a stir bar, 45 mg of HPMC were dissolved in a 1:2 solvent mixture of water (0.33 mL) and ethanol (0.66 mL) by stirring for 4 h at RT resulting in a viscous 5% HPMC solution. To formulate the ink, the Tiron-functionalized oxides were added to the HPMC solution and the suspension was allowed to stir for 12 h, thus affording a homogeneous HPMC-based ink with 30% oxide solid content. The metal ratio was the same as in the case of PVA oxide ink. A non-Newtonian behavior was observed for the HPMC oxide ink, exhibiting a range of dynamic viscosity between 1.8–3.2 Pa s (Figure 5.1b). The surface tension was measured to be 44±2 $\mathrm{mN\ m^{-1}}$.

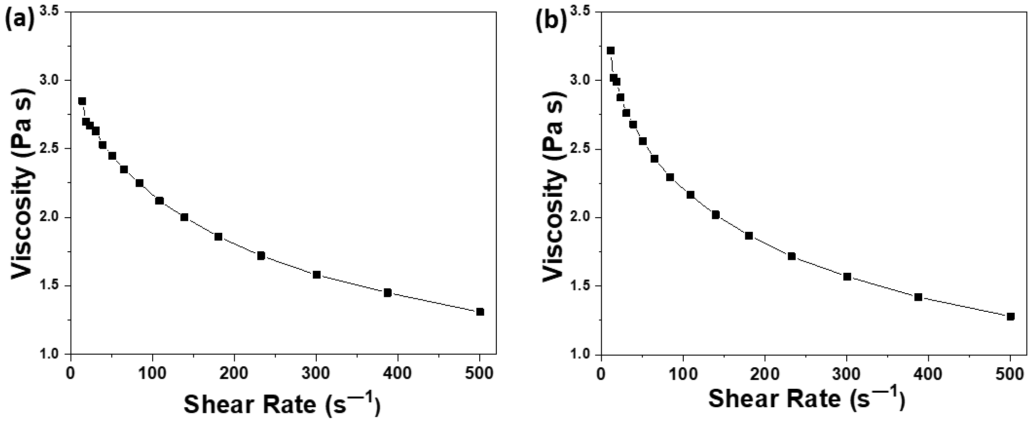

Figure 5.1. Dynamic viscosity of the formulated (a) PVA oxide ink and (b) HPMC oxide ink suggesting a non-Newtonian behavior.

5.2.2.3 Substrates

The 2.6 cm × 2.6 cm SLG substrates with 1 mm thickness (Fisher Scientific), 2.5 cm × 2.5 cm FTO/SLG substrates with 2 mm thickness (7 $\Omega\ \mathrm{sq^{-1}}$, Dyesol), and 2.6 cm × 2.6 cm Mo-coated SLG (Mo/SLG) substrates with 1 mm thickness were cleaned as described on Chapter 2 (section 2.2.4).

The 2.5 cm × 2.5 cm graphite sheets with 2 mm thickness (density = 1.3 $\mathrm{g\ cm^{-3}}$, SIGRAFLEX) and 7.5 cm × 2.5 cm stainless steel plates with 1 mm thickness were cleaned by rinsing with ethanol and water, followed by drying under N_2 flow.

5.2.2.4 Screen printing

Square-shape patterns of 2.5 cm × 2.5 cm were printed on different substrates using the as-formulated oxide inks and the graphene/carbon pastes, as described on Chapter 2 (section 2.2.4). For the photoabsorber film deposition, a 180 $\mathrm{threads\ cm^{-1}}$ mesh count with 27 µm of thread diameter and 24 µm of mesh opening was employed. The films were screen-printed three and two times for PVA and HPMC oxides inks, respectively. After each printing step, the films were immediately dried at 90 °C for 5 minutes on a hot plate to evaporate the solvent of the ink. Graphene and carbon pastes were screen printed on the substrates using a 120 $\mathrm{threads\ cm^{-1}}$ mesh count with 30 µm of thread diameter and 53 µm of mesh opening. Two- and ten-step printing were used for graphene and carbon pastes, respectively. The screen printing conditions used are described on Chapter 2 (section 2.2.4).

5.2.2.5 Calcination and selenization

Prior to selenization, the screen-printed thin films from PVA oxide ink were subjected to calcination (Lenton, Eurotherm) at 500 °C for 3 min under air (heating ramp: $1\ \mathrm{°C\ min^{-1}}$) in order to remove organic matter. To convert mixed oxide patterns into the desired CIGSe phase, the patterns were subjected to a selenization procedure as described on Chapter 3 (section 3.2.5) using 550 °C at $55\ \mathrm{°C\ min^{-1}}$, and held at this temperature for 30 min and 5 min in the case of the thin films printed from PVA and HPMC oxide inks, respectively.

5.2.3 Top conductive layer development

For *i*-ZnO ink formulation, 0.85 g of ZnO particles synthesized using a reported method [16] were dispersed in 10 mL of ethanol using ultrasonication at RT during 6 h. For ITO ink formulation, 2.5 mL of the commercial dispersion in water were mixed with 2.5 mL of ethanol using vortex and ultrasonication at RT during 20 min.

5.2.4 Photovoltaic cells fabrication

The CIGSe photoabsorber deposition was performed using two-step printing of HPMC oxide ink formulation on FTO/SLG substrates as described on section 5.2.2.4. Then, the thin films were selenized using the conditions described on section 5.2.2.6. Finally, the prepared films were etched and CdS buffer layer was deposited by CBD as described on Chapter 3 (section 3.2.5). Next, *i*-ZnO window layer was sputtered using a rotating stage at 10 rpm with 20 sccm of Ar flow at 60 W during 50 min, providing a final layer thickness of 50 nm. The AZO transparent conductive layer was sputtered under Ar flow of 20 sccm and 60 W during 42 min, providing a final thickness of 200 nm. The fabricated PV cell was finalized by scratching the edge of the cells with a scalpel down to the FTO back contact. Next, a thin layer of metallic indium was welded on the scratched place to improve the electric contact between the cell and the probes used for photovoltaic performance measurements.

All-non-vacuum processed PV cells were produced as described above up to and including the CdS layer. The top conductive layers used for this cell were *i*–ZnO and ITO. The *i*–ZnO layer was deposited by one-step spray coating and dried at 120 °C for 1 h to improve the crystallinity. ITO layer was spray-coated using two steps followed by drying at 100 °C to ensure solvent evaporation. The spray coating process was performed manually using an airbrush gun (Dexter) powered by compressed air, vertically positioned 20 cm above a hotplate at 90 °C using a zig-zag coating direction. As comparison for the spray-coated device, sputtering of ITO was also performed using a rotating stage at 10 rpm with 20 sccm of Ar flow at 60 W during 4 h, providing a final layer thickness of 200 nm.

5.2.5 Characterization

Surface tension and rheological properties:

The RT surface tension and ink dynamic viscosity measurements were performed using DSA–CA and a rheometer, respectively, as described on Chapter 2 (section 2.2.5).

Optical microscopy (OM):

Optical microscopy imaging of the oxides dispersion was performed using an Eclipse LV100 ND microscope (Nikon) with x10 and x20 ocular and objective lenses, respectively.

X-ray diffraction:

The phase composition of the films was determined using XRD as described on Chapter 2 (section 2.2.5).

Raman spectroscopy:

To inspect the local structure of the CIGSe photoabsorber layer, Raman spectroscopy measurements were performed as described on Chapter 2 (section 2.2.5), using a laser beam power of 1.5 mW.

Electron microscopy:

The evaluation of the surface and cross-sectional morphologies as well as chemical composition of the photoabsorber and top conductive thin films and the cross-sectional evaluation of the produced PV cells were performed using SEM as described on Chapter 2 (section 2.2.5).

FIB method was used to prepare the lamella for cross-sectional investigation. The investigation of fine microstructure and the chemical composition of the final PV cells was performed using HAADF–STEM, SAED, and STEM–EDX as described on Chapter 3 (section 3.2.6).

Optical properties:

UV-Vis-NIR optical measurements and the band gap determination of the CIGSe photoabsorber films were carried out as described on Chapter 2 (section 2.2.5).

Thermographic analysis:

UV-Vis-NIR optical measurements and the band gap determination of the CIGSe photoabsorber films were carried out as described on Chapter 2 (section 2.2.5).

J–*V* characterization:

J–*V* curves of the PV cells were measured by a four-point probe as described on Chapter 3 (section 3.2.6). For each sample, ≈10 cells with an area of ≈$0.16\ \mathrm{cm}^2$ each were isolated and measured using a two-probe system, placed on the top contact active area cell of AZO/ITO, and on indium-welded back contact.

5.3 Results

5.3.1 Screen-printed CIGSe photoabsorber layers

The replacement of energy-demanding vacuum-deposition processes for CIGSe PV fabrication by more sustainable screen printing approaches is associated with the important challenge of the design and development of affordable and non-toxic inks. To produce such inks, commercially available CuO, $\mathrm{In_2O_3}$, and $\mathrm{Ga_2O_3}$ were evaluated as starting materials to be dispersed on water and ethanol solvents to formulate eco-friendly non-toxic oxide inks. To this end, PVA and HPMC polymers were selected as thickeners due to their low environmental impact, good solubility in the selected solvents, appropriate rheological properties, and good adhesion properties. This would enable the development of inks with high viscosity for screen printing deposition of thin mixed oxide layers with good adhesion to the substrate of interest.

5.3.1.1 PVA oxide ink formulation

For PVA-based ink formulation, appropriate amounts of the three oxides, targeting the ratio of $\mathrm{Cu_{0.83}(In_{0.7}Ga_{0.3})Se_2}$, were initially simply mixed in 25% aqueous solution of PVA. Although the resultant ink had a smooth visual appearance, after screen printing the ink over SLG substrate followed by selenization, the obtained thin film did not. A dispersion problem leading to the formation of a non-homogenous and non-compact CIGSe photoabsorber layer was detected by SEM imaging (Figure 5.2).

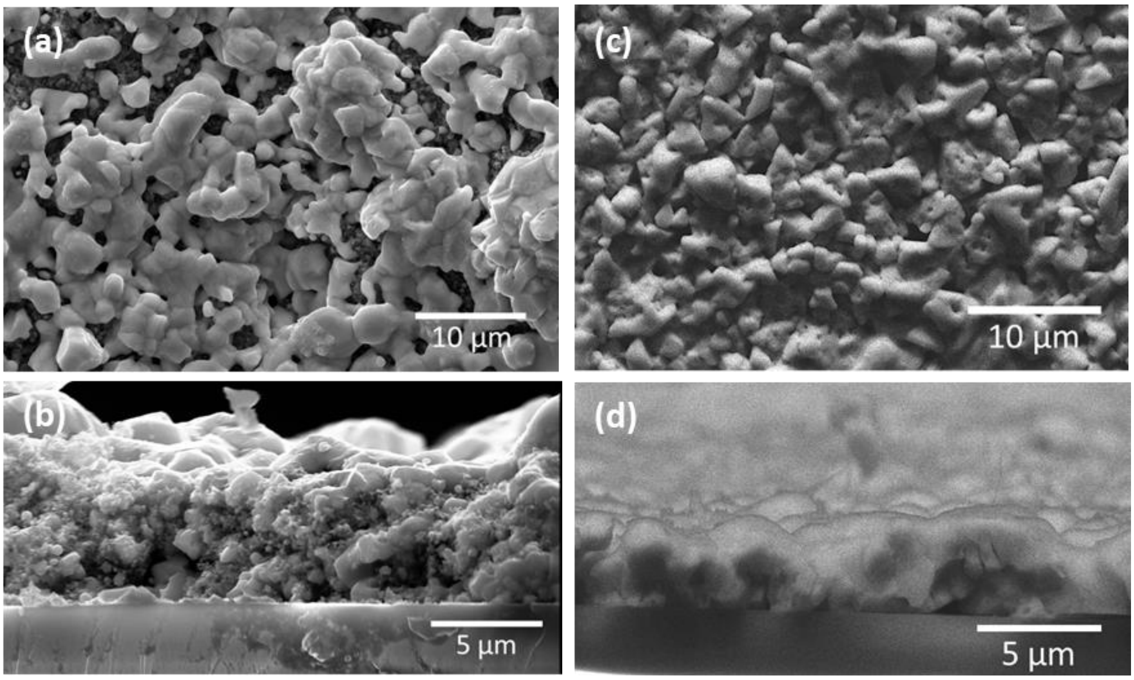

Figure 5.2. SEM images for the comparison of the surface (a,c) and cross-sectional (b,d) morphologies of the resultant CIGSe photoabsorber layers before (a,b) and after (c,d) PVA oxide ink optimization.

To improve the dispersion of the oxides in the PVA solution, seven water-soluble surfactants (CTAB, Tiron, Tween 60, BYK180, BYK199, BYK2013, BYK7420 ES) were selected to be tested as dispersion additives (2% relative to oxide solids). Based on the results of the OM imaging of the dispersions (Figure 5.3), Tiron was established to provide the best dispersion of the oxides in water. This was mainly attributed to the decreased surface tension of water induced by Tiron and the good chelating properties of this compound [17].

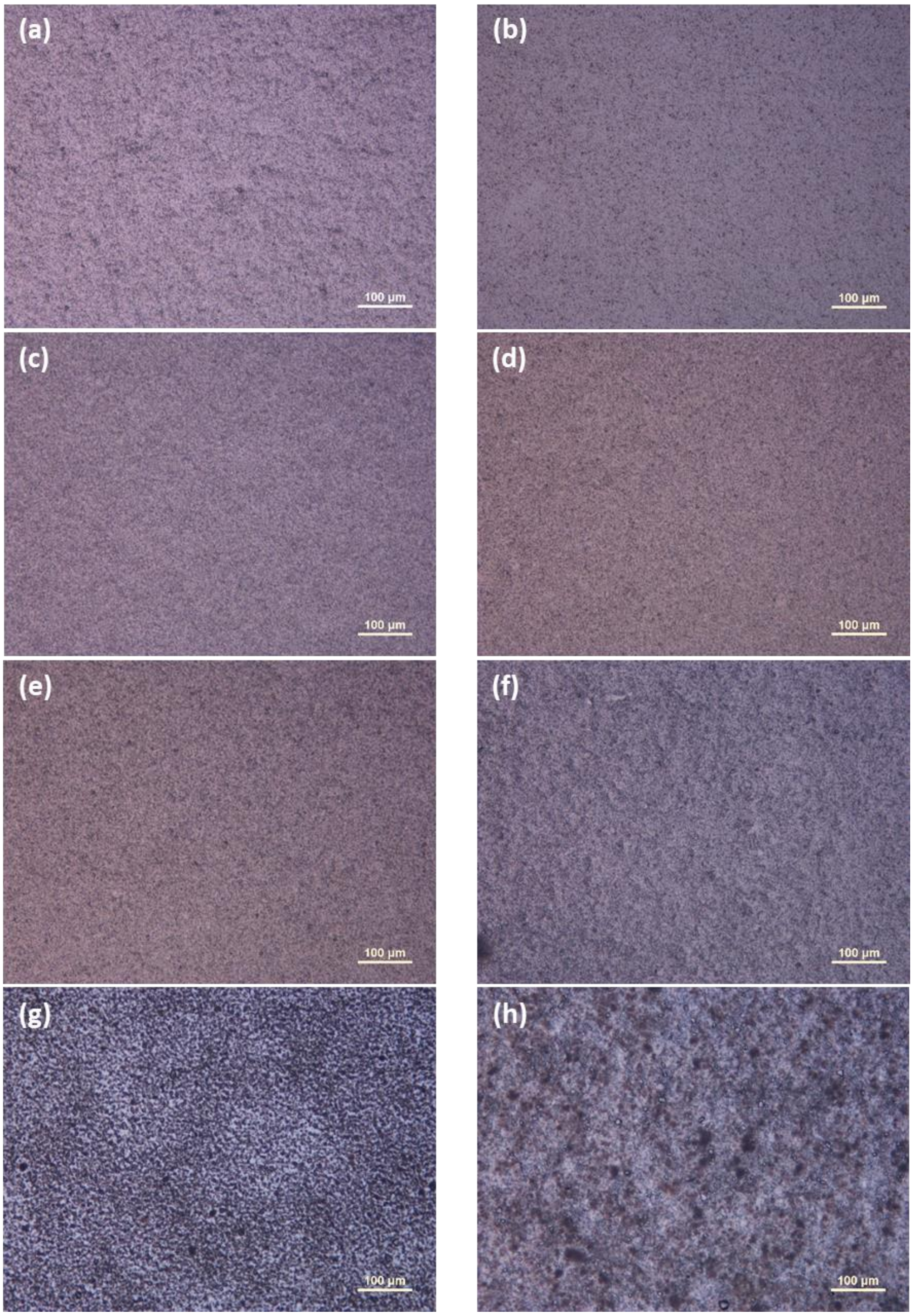

Figure 5.3. Optical microscopy images showing oxide dispersion in water without surfactant (a) and with CTAB (b); Tiron (c); Tween 60 (d); BYK180 (e); BYK199 (f); BYK2013 (g), and BYK7420 ES (h).

Nevertheless, despite achieving good oxide dispersion, the appearance of bubbles was observed upon introduction of Tiron into the PVA ink (Figure 5.4a). To overcome this, silicone-based defoamer BYK28 was added into the ink, which effectively solved the bubbling problem, resulting in a smooth thin film (Figure 5.4b).

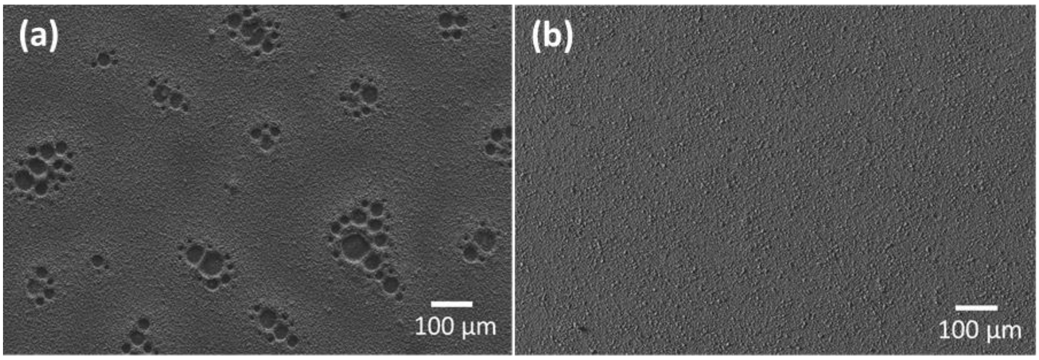

Figure 5.4. SEM images of CIGSe thin films obtained without (a) and with (b) the addition of BYK28 defoamer.

To convert the mixed oxide thin films into CIGSe photoabsorber layers, selenization under $\mathrm{H_2}$ atmosphere was carried out. After this procedure, the formation of carbon inclusions in the resultant CIGSe layer was observed as a result of carbonization of the organic matter of the ink, mainly PVA (Figure 5.5a). The presence of carbon in the CIGSe photoabsorber is undesired [18], since such impurities will affect the electrical properties of the films, thus significantly lowering the efficiency of the PV cell. Hence, a calcination step was introduced prior to selenization in order to remove the main part of the organic matter of the ink. Based on the TGA results of the PVA oxide ink, it was established that, upon calcination under air, PVA degrades entirely at ca. 500 °C (Figure 5.5b). This was further confirmed by the absence of the PVA stretching vibration mode at ≈2900 $\mathrm{cm^{-1}}$ [19] in the Raman spectra of the calcined thin films (Figure 5.5a).

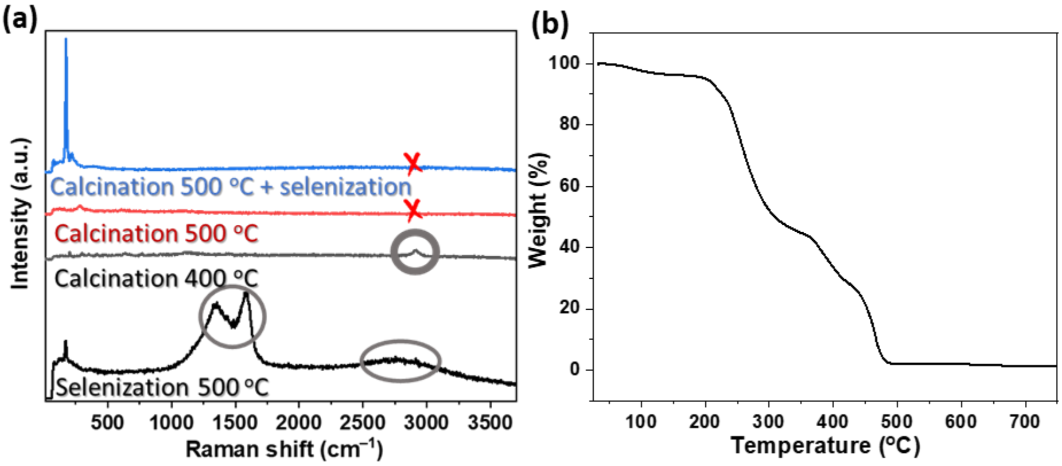

Figure 5.5. Raman spectra of the thin films after different heat treatment procedures, where the circles indicate the carbon inclusions (a). TG characteristic curve of PVA oxides ink under air (b).

After the introduction of the calcination step at 500 °C followed by selenization, a compact and dense CIGSe photoabsorber layer with nearly uniform film thickness of ≈3.5 µm was achieved (Figures 5.2c, d). According to the XRD analysis, the resultant thin film is phase-pure CIGSe with tetragonal chalcopyrite structure, without oxides or other secondary phases present (Figure 5.6a). The phase purity was further confirmed by Raman spectroscopy, which shows a sharp peak at 174 cm^{-1} and two broader bands at 120 and 218 cm^{-1} corresponding to A_1, B_1, and B_2/E vibrational modes of CIGSe [20, 21], respectively (Figure 5.6b). Notably, no band at ≈260 cm^{-1} associated with the common CuSe secondary phase was detected by Raman spectroscopy. According to the SEM–EDX analysis, the chemical composition of the CIGSe thin film was estimated to be $\mathrm{Cu_{0.9}(In_{0.74}Ga_{0.25})Se_2}$ (Figures 5.6c, d), which agrees fairly well with the targeted composition in the as-formulated novel PVA ink.

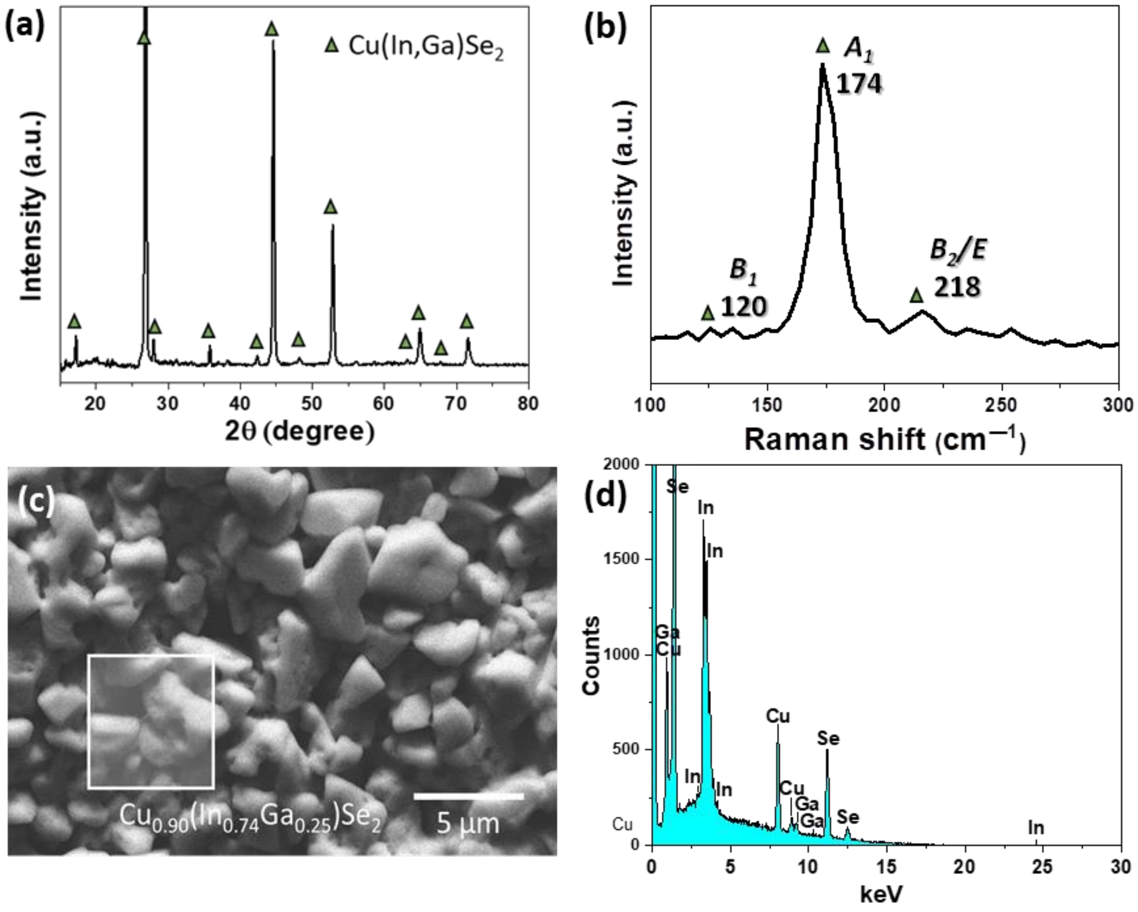

Figure 5.6. Structural and compositional characterization of the CIGSe photoabsorber layer obtained by screen printing of PVA oxide ink on SLG followed by calcination and selenization: XRD diffractogram (*hkl* peak assignment is based on ICDD card no. 00-066-0140 for tetragonal CIGSe) (a), Raman spectrum (b), and the SEM image (c) together with the corresponding EDX spectrum (d).

5.3.1.2 Selection of the conductive substrate

The developed eco-friendly PVA oxide ink successfully afforded a high-quality CIGSe photoabsorber layer on SLG substrate. However, to produce a CIGSe PV cell, the thin film must be deposited on a conductive substrate, which works as a back contact for the current collection. To this end, several potential conductive substrates were investigated.

Mo-coated SLG is a common substrate for CIGSe PVs [22], and therefore, the as-developed PVA oxide ink was initially deposited on Mo/SLG by screen printing followed by the established calcination and selenization procedures. Unfortunately, the Mo/SLG substrate did not withstand the selenization conditions, and after exposure to 550 °C for 30 min under a reductive atmosphere of $5\%\mathrm{H_2/Ar}$ in the presence of Se vapor, the resultant CIGSe thin film peels due to the transformation of metallic Mo into $\mathrm{MoSe_2}$ with concomitant loss of adhesion to the SLG substrate, accordingly to the following chemical reactions (Equation 5.1 and 5.2).

$$\mathrm{H_{2(g)} + Se_{(g)} = H_2Se_{(g)}} \tag{5.1}$$

$$\mathrm{Mo_{(s)} + 2H_2Se_{(g)} = MoSe_{2(s)} + 2H_{2(g)}} \tag{5.2}$$

Therefore, other conductive substrates were investigated taking into account the necessary high electrical conductivity and thermal stability [22]. First, a bare graphite sheet was studied, but its high surface roughness did not allow to obtain a compact CIGSe thin film (Figure 5.7a). To overcome this issue, the graphite sheet was coated by a graphene paste using a screen printer equipped with a 120 mesh count. Although this coating route afforded the formation of the desired CIGSe thin film (Figure 5.7b), the observed adhesion problems and graphite delamination during the thermal treatments (Figure 5.8) hampered this approach. Next, bare stainless steel was established to allow a very good adhesion of the CIGSe photoabsorber layer to the substrate (Figures 5.7c and 5.9a, b). However, the formation of a large quantity of a secondary $\mathrm{Fe_3Se_4}$ phase underneath the CIGSe thin film was detected by XRD (Figure 5.9c, d), which was attributed to selenization of the stainless-steel substrate (Equation 5.3).

$$\mathrm{3Fe_{(s)} + 4H_2Se_{(g)} = Fe_3Se_{4(s)} + 4H_{2(g)}} \tag{5.3}$$

This phase was found to intermix well with the CIGSe phase induced by the diffusion of Fe, thus turning the CIGSe semiconducting layer into a conductive one, which is not suitable for PV cell development. To avoid such intermixing/diffusion, a conductive carbon buffer layer was deposited by screen printing, using a 120 mesh count, over the stainless-steel substrate before printing the oxide ink. However, this approach led to the appearance of cracks in the resultant photoabsorber CIGSe thin film and its peeling (Figure 5.7d), most likely due to the mismatch of the thermal expansion coefficients of stainless steel, C, and CIGSe [15].

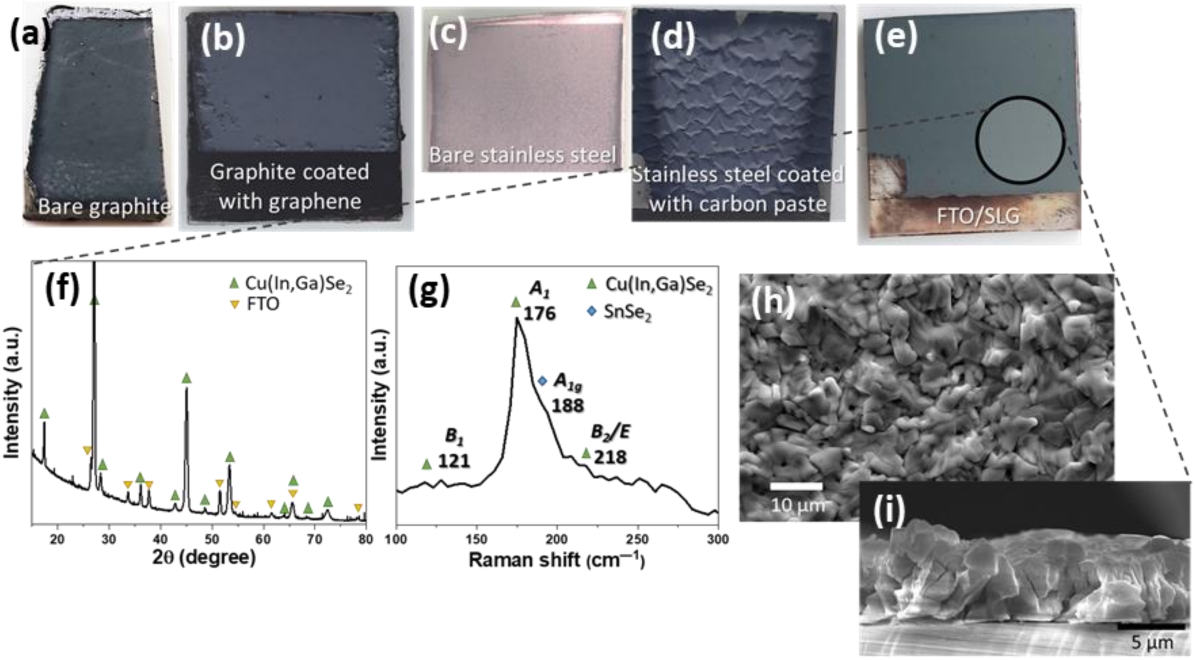

Figure 5.7. Appearance of the CIGSe photoabsorber layers deposited on graphite (a), graphene-coated graphite (b), stainless steel (c), carbon-coated stainless steel (d), and FTO/SLG (e). Structural and morphological characterization of the CIGSe thin films screen printed on FTO/SLG using PVA oxide ink, followed by calcination and selenization: XRD pattern (*hkl* peak assignment are based on ICDD card no. 01-082-9226 for tetragonal CIGSe and no. 04-003-5853 for tetragonal SnO_2 from FTO) (f), Raman spectrum (g), surface (h) and cross-sectional (i) SEM images.

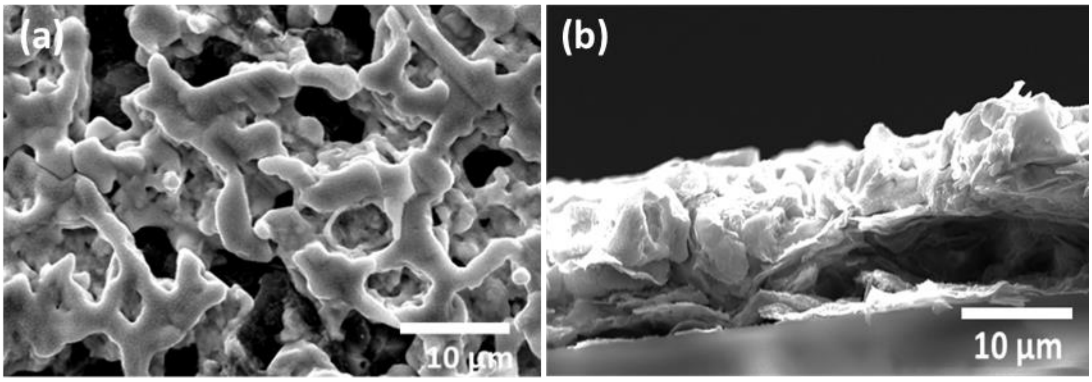

Figure 5.8. Representative SEM surface (a) and cross-sectional (b) images of the CIGSe photoabsorber deposited on graphite coated with graphene.

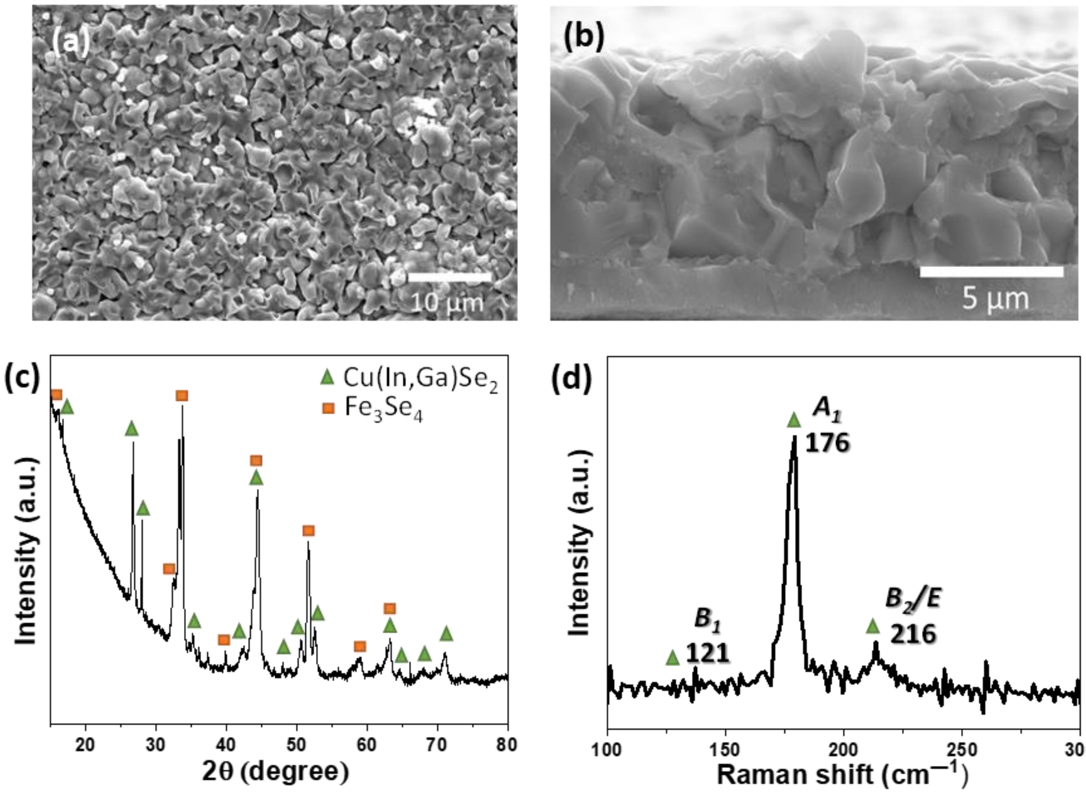

Figure 5.9. Characterization of CIGSe photoabsorber layer deposited on bare stainless-steel substrate: surface (a) and cross-sectional (b) SEM images, XRD pattern (*hkl* peak assignment are based on ICDD card no. 01-079-7081 for tetragonal CIGSe and no. 04-007-8080 for monoclinic Fe_3Se_4 from stainless steel) (c) and Raman spectrum (d).

After ruling out the conductive Mo/SLG substrate, uncoated and coated graphite, and stainless-steel substrates, FTO/SLG was next investigated. As illustrated (Figure 5.7e), a high-quality compact thin film with uniform thickness of ≈4 µm was observed over FTO/SLG (Figures 5.7h, i). XRD analysis confirmed the phase purity of the resultant CIGSe layer (Figure 5.7f). By Raman spectroscopy (Figure 5.7g), a shoulder band was detected at 188 cm^{-1}, which most likely corresponds to the A_{1g} mode of the secondary $\mathrm{SnSe_2}$ phase [23], suggesting a partial transformation of the $\mathrm{SnO_2}$ of FTO into $\mathrm{SnSe_2}$ during selenization (Equation 5.4) due to the harsh conditions of this fabrication step.

$$\mathrm{SnO_{2(s)} + 2H_2Se_{(g)} = SnSe_{2(s)} + 2H_2O_{(g)}} \tag{5.4}$$

Importantly, the electrical characteristics of the FTO back contact and CIGSe photoabsorber layer were found to be preserved, indicating that FTO/SLG is the most suitable conductive substrate for the screen printing deposition of the CIGSe thin film when using the PVA oxide ink.

5.3.1.3 HPMC oxide ink formulation

Screen printing of the PVA oxide ink over conductive FTO/SLG followed by calcination and selenization provided a high-quality CIGSe photoabsorber thin film. Nevertheless, in order to reduce the number of fabrication steps, another eco-friendly oxide ink was formulated using water-soluble HPMC as a thickener: due to its lower degradation temperature of ≈250 °C and higher viscosity than PVA, the HPMC ink features a lower content of organic matter, thus potentially eliminating the calcination step.

In contrast to the PVA oxide ink above, where Tiron was directly added to the ink solution, in the case of the HPMC-based ink formulation, the oxides were functionalized by Tiron in advance. Then, a mixture of Tiron-functionalized CuO, $\mathrm{In_2O_3}$, and $\mathrm{Ga_2O_3}$ was dispersed in 1:2 water/ethanol solution containing 5% of HPMC. TGA of the ink under Ar atmosphere suggests that the organic matter should entirely degrade during the selenization procedure (Figure 5.10), thus allowing for omission of the calcination step.

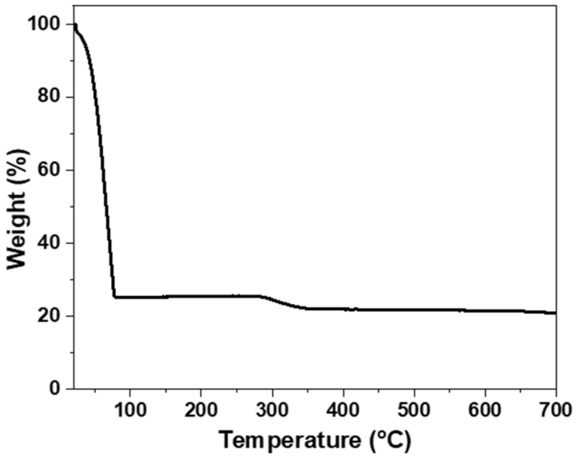

Figure 5.10. TG characteristic curve of the HPMC oxide ink under Ar.

After screen printing the ink over FTO/SLG and subsequent selenization, the formation of a compact thin film with uniform thickness of ≈2.5 µm was observed (Figure 5.11).

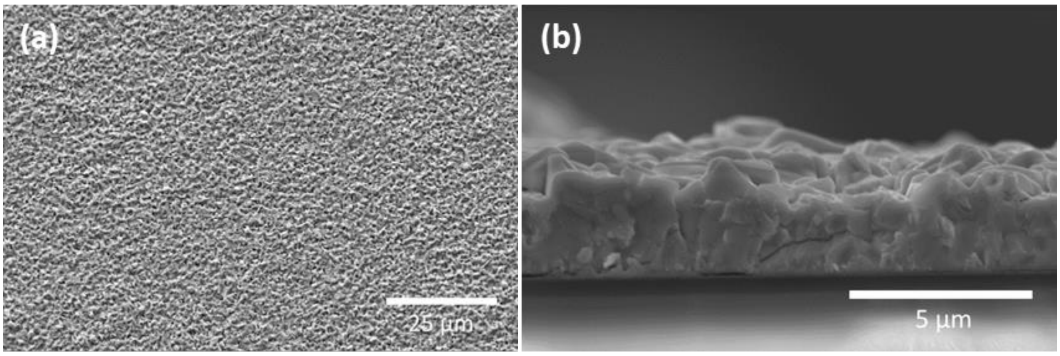

Figure 5.11. Surface (a) and cross-sectional (b) SEM images of the resultant CIGSe photoabsorber layer deposited from the HPMC oxide ink.

The XRD and Raman spectroscopy analyses of the thin film revealed the main characteristic peaks of the CIGSe phase (Figure 5.12a, b) with a minor admixture of a $\mathrm{SnSe_2}$ phase detected by Raman spectroscopy (Figure 5.12b). SEM–EDX analysis revealed that the chemical composition of the CIGSe phase is $\mathrm{Cu_{0.92}(In_{0.77}Ga_{0.31})Se_2}$ (Figure 5.12c, d), which is consistent with the nominal ratio of the metals in the HPMC oxide ink.

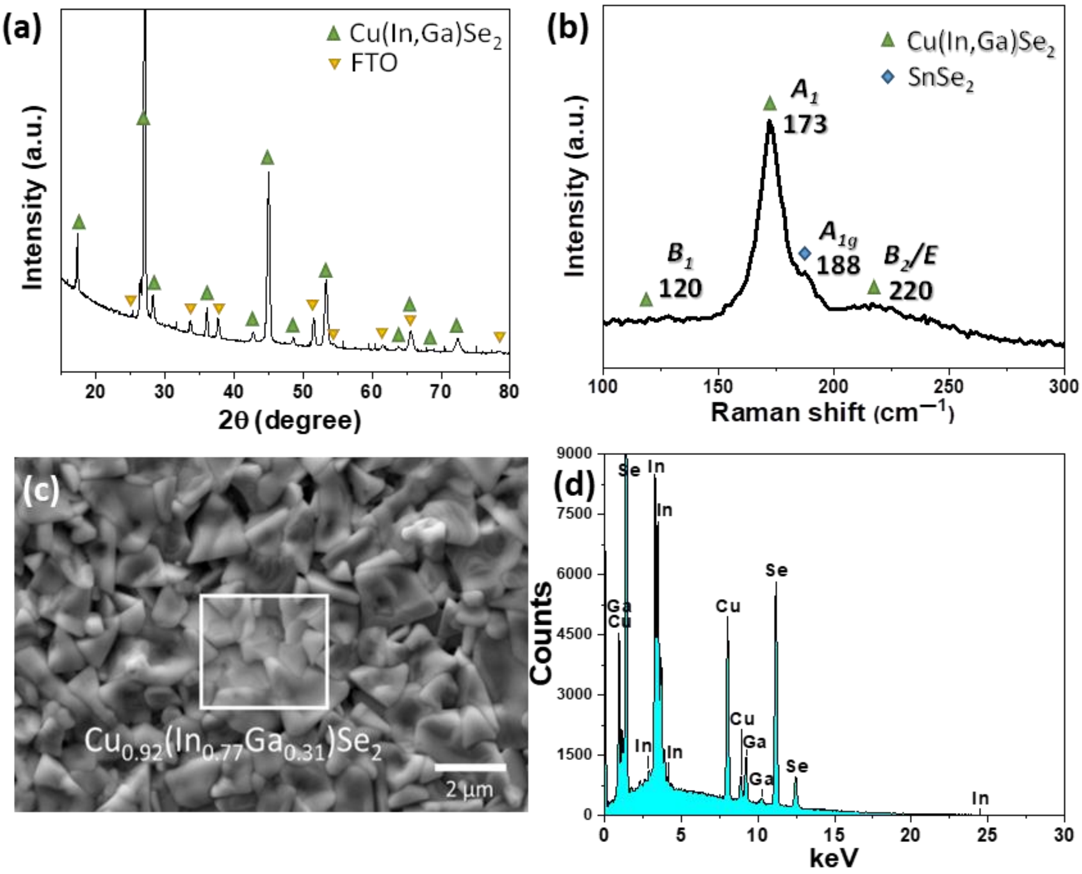

Figure 5.12. Structural and compositional characterization of the resultant CIGSe photoabsorber layer deposited onto FTO/SLG substrate using the HPMC oxide ink: XRD pattern (*hkl* peak assignment are based on ICDD card no. 01-082-9226 for tetragonal CIGSe and no. 04-003-5853 for tetragonal SnO_2 from FTO) (a), Raman spectrum (b), and SEM image (c), together with the corresponding EXD spectrum (d).

5.3.1.4 Optical properties of the photoabsorber thin films

The experimental band gap evaluation of the as-fabricated photoabsorber thin films produced from PVA and HPMC oxide inks was performed by optical characterization (Figure 5.13). The absorption spectra showed that both thin films strongly absorb light from the visible and near-infrared regions. The band gap energy for the $\mathrm{Cu_{0.9}(In_{0.74}Ga_{0.25})Se_2}$ thin film obtained by screen printing of the PVA oxide ink followed by calcination and selenization was estimated to be 0.97±0.02 eV. On the other hand, the HPMC oxide ink offers $\mathrm{Cu_{0.92}(In_{0.77}Ga_{0.31})Se_2}$ photoabsorber with increased band gap energy of 1.08±0.02 eV, which is slightly lower than the reported optimal band gap of ≈1.14 eV for CIGSe PVs [24, 25].

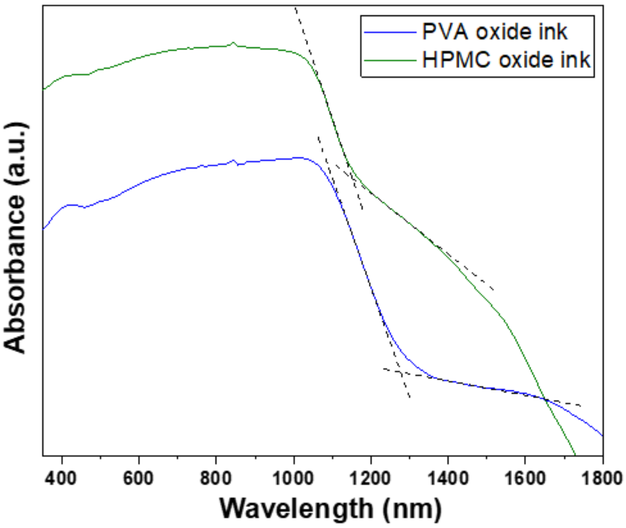

Figure 5.13. UV-Vis-NIR absorption spectra of the resultant CIGSe thin films fabricated from PVA and HPMC oxide inks.

5.3.2 CIGSe photovoltaic devices

5.3.2.1 Screen-printed CIGSe device

The excellent results presented for the screen printable HPMC oxide ink has driven to choose it to continue the study for the production of a CIGSe PV cell. A PV cell containing the screen-printed CIGSe thin film was finished by first depositing a CdS layer of ≈70 nm thickness through CBD to complete the *p*–*n* junction and to function as a buffer for the correct deposition of the upper layers. Then, a 50 nm *i*–ZnO layer followed by a 200 nm transparent conductive oxide layer of AZO were sputtered on top for the charge carrier collection. A cross-sectional analysis of the device with the stack SLG/FTO/CIGSe/CdS/*i*–ZnO/AZO was performed using a FIB SEM specimen preparation (Figure 5.14), revealing a PV cell with a thickness of ≈3 μm with well-stacked layers.

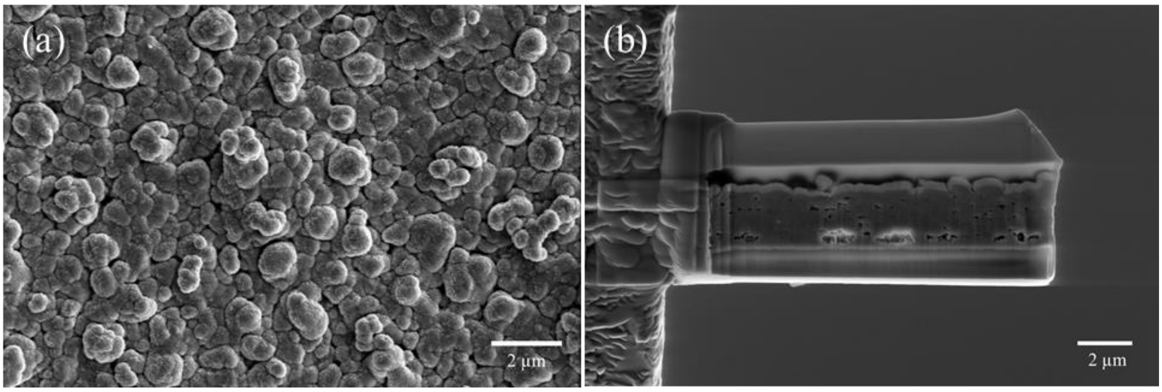

Figure 5.14. SEM images of SLG/FTO/CIGSe/CdS/*i*–ZnO/AZO PV cell: top surface (a) and FIB lamella preparation for cross-sectional imaging (b).

The chemical composition was further analyzed by EDX mapping in STEM mode (Figure 5.15). Starting from the top layers, a small intermixing of CdS with the CIGSe photoabsorber was found with a presence of Cd and S elements in some of the pores throughout the photoabsorber. Nevertheless, CdS was found to accomplish its function as a buffer layer, preventing the penetration of Zn and O elements from the top conductive layers to the photoabsorber. Notably, a uniform distribution of Cu, In, Ga, and Se was found through the photoabsorber with no signs of the presence of unreacted metal oxides, suggesting a complete conversion of Cu, In, and Ga oxides into the CIGSe crystal. Nevertheless, due to a small grain size of the particles the photoabsorber layer was found to be porous.

In the chemical composition analysis of the device, a migration of Sn from the FTO back contact into the CIGSe layer was also detected as the presence of voids at the FTO–CIGSe interface, similarly to the fabricated CIGSe PV cell presented on Chapter 3. This migration is attributed to the unavoidable reaction of Sn with Se during selenization, which gives rise to the aforementioned voids at the interface. Comparing with the previous cell from Chapter 3, a lower amount of such defects were found in the present device, which is most likely due to the elimination of the calcination step used in the previous procedure.

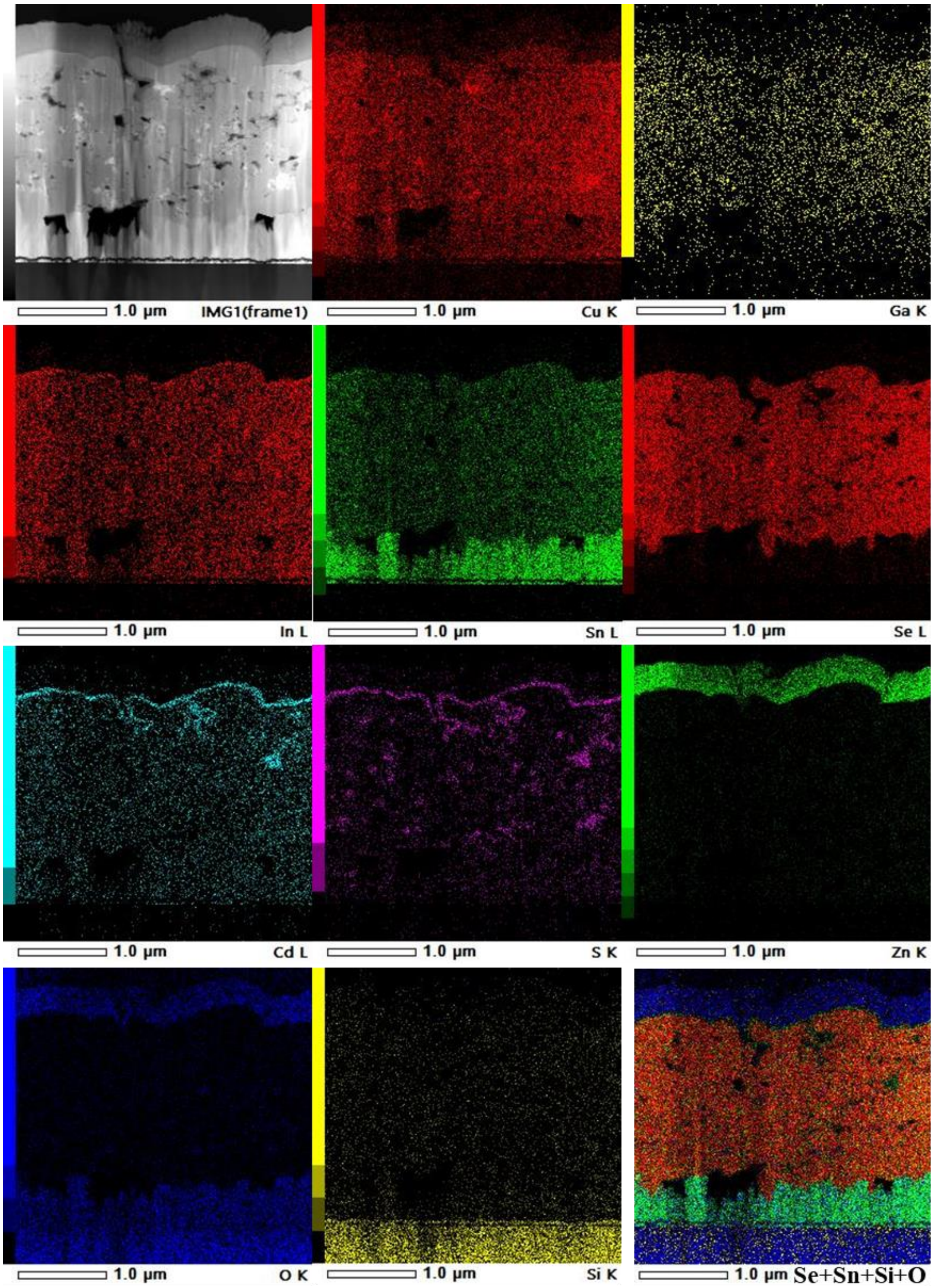

Figure 5.15. Cross-section HAADF–STEM image of the champion PV cell: SLG/FTO/CIGSe/CdS/*i*–ZnO/AZO, with the collected EDX maps of Cu K, Ga K, In L, Sn L, Se L, Cd L, S K, Zn K, O K, Si K elements and Se+Sn+Si+O mixture color image.

The photovoltaic performance of the device was measured by acquiring *J–V* curves on ten PV cells in total with an area of 0.16 cm^2 each, under light and dark (Table 5.1), evidencing that a reliable and promising CIGSe PV cell has been produced with an average efficiency of ≈4.6±1.2%. The champion PV cell exhibited a remarkable efficiency of 7.9%, J_{SC} of 39.5 $\mathrm{mA\ cm^{-2}}$, V_{OC} of 0.33 V, and FF of 57.8% (Figure 5.16). The high J_{SC} can be associated with the low band gap of the photoabsorber CIGSe thin film of 1.08 eV. Similarly, the low V_{OC} is related to recombination losses and the low bandgap. Similar photovoltaic behavior has been observed in the literature for CIGSe photoabsorber layers prepared employing a selenization procedure [10, 26-28]. The achieved moderate FF is attributed to losses stemming from the series resistance.

Table 5.1. Photovoltaic parameters of PV cells fabricated from screen-printed photoabsorber layer and sputtered *i*–ZnO and AZO layers.

PV cell	**Efficiency (%)**	**FF (%)**	J_{SC} ($\mathrm{mA\ cm^{-2}}$)	V_{OC} **(V)**
1	4.9	39.2	36.0	0.33
2	3.6	52.1	18.4	0.36
3	3.6	50.8	19.7	0.34
4	7.9	57.8	39.5	0.33
5	4.3	49.5	24.0	0.35
6	4.5	44.5	28.6	0.34
7	4.8	37.8	36.5	0.33
8	3.8	39.2	28.5	0.33
9	4.1	34.0	33.8	0.34
10	4.6	35.3	36.6	0.34
Average	4.6	44.0	30.2	0.34
Standard Deviation	1.2	8.1	7.5	0.01

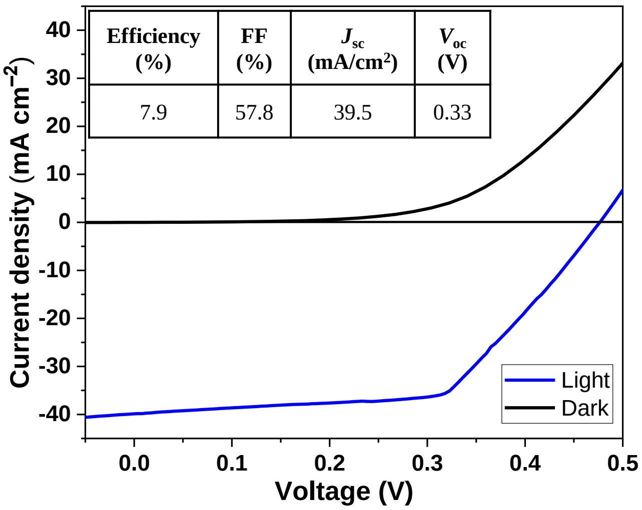

Efficiency (%)	FF (%)	J_{sc} (mA/cm^2)	V_{oc} (V)
7.9	57.8	39.5	0.33

Figure 5.16. The light and dark *J–V* curves of the champion CIGSe PV cell with screen-printed photoabsorber.

Despite the promising results, the PV performance of the presented device would be further improved by additional optimization. Importantly, the aforementioned porous photoabsorber and the voids in the FTO–CIGSe interface are recombination spots of charge carriers resulting in low V_{OC}, thus impacting negatively on the PV performance of the device. Furthermore, these also give rise to high series resistance and therefore moderate FF. To eliminate the recombination spots resulting from the porosity of the photoabsorber, a longer selenization procedure or further sulfurization may increase the grain size and therefore result in a densely packed photoabsorber layer, increasing V_{OC} and concomitantly the PV performance [29]. Regarding the voids in the FTO–CIGSe interface, the back contact–photoabsorber interface should be improved. Notably, this study has demonstrated that among Mo/SLG, bare stainless steel, carbon-coated stainless steel, bare graphite, graphene-coated graphite, and FTO/SLG, the last is the most suitable back contact to be used with the herein presented deposition methodologies. Therefore, the implementation of a passivation layer above the FTO back contact may provide a solution to prevent $\mathrm{SnSe_2}$ formation and the resulting voids, thus improving the PV performance of the device.

5.3.2.2 All-non-vacuum processed device

To further increase the sustainability of the CIGSe PV cells, the replacement of the vacuum-based processes used in the deposition of the top conductive layers *i*–ZnO/AZO by non-vacuum-based ones has been targeted. Spray coating was the chosen technique for the deposition due to its simplicity and the absence of thickener additives in the ink formulation. To this end, *i*–ZnO NPs were synthesized following a reported procedure [16] and dispersed in ethanol using ultrasonication.

ITO is the most commonly used TCO in the industry due to its convenient processability and good optical and electrical properties, both desirable characteristics for cost-effective industrial production of PVs [30, 31]. Thus, ITO was selected as the window layer for the CIGSe PV cell under development. For the *i*–ZnO and ITO inks, one- and two-step coating, respectively, was found to be sufficient to achieve a full coverage of the layers below. Cross-sectional images of the spray-coated *i*–ZnO layer revealed a thickness of ≈100 nm (Figure 5.17).

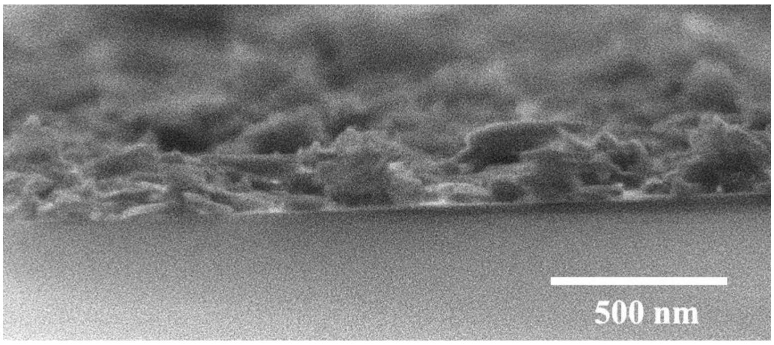

Figure 5.17. Cross-sectional image of spray-coated *i*–ZnO layer.

The top conductive layers of PV cells greatly impact their performance, and in order to allow for efficient absorption of photons by the *p*–*n* junction, these layers should feature high transparency in the visible region (>80%) and good electrical properties [32]. By cross-sectional SEM imaging (Figure 5.18a), the ITO layer was found to be a compact film with a thickness of ≈340 nm. UV–Vis–NIR measurements revealed that the range of highest optical transmittance for the spray-coated ITO layer matches well with the range of highest absorption of photons by the CIGSe photoabsorber thin films (400–1100 nm) (Figure 5.18b). Moreover, the observed optical transmittance in the visible region (λ = 550 nm) was found to be around ≈70%, which is slightly lower than the reported optimal value (>80%).

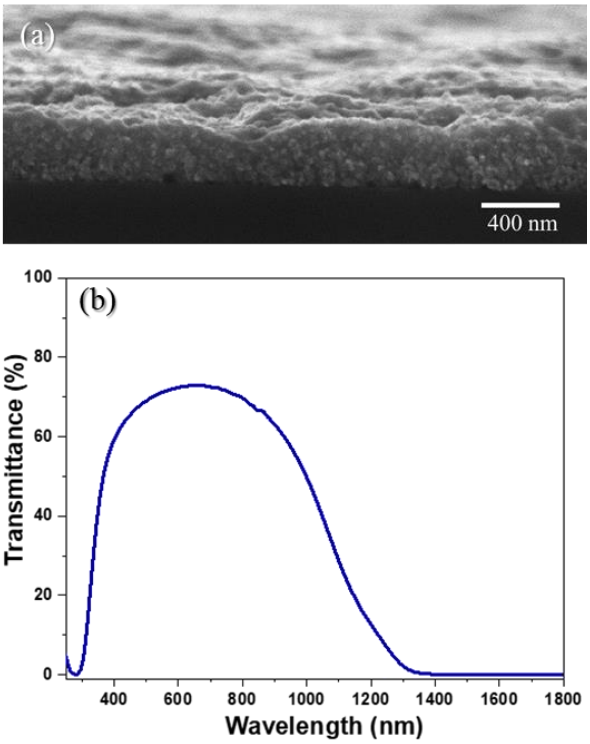

Figure 5.18. Cross-sectional SEM imaging of the ITO layer coated on SLG (a), together with the respective transmittance UV–Vis–NIR spectra (b).

The impact of the replacement of the sputtering procedure of ITO by spray coating on the performance was studied by measuring the *J*–*V* curves of the PV cells with screen-printed photoabsorber, chemical-bath-deposited CdS, and spray-coated *i*–ZnO (Figure 5.19). In total, 20 PV cells were evaluated with an area of 0.16 cm^2 each under light and dark (Tables 5.2 and 5.3). The highest photovoltaic performance was found for the cell with the sputtered ITO layer (Figure 5.19a), with 5.6% of efficiency for the champion device and an average efficiency of 4.7±0.6%, which was attributed to the good deposition uniformity provided by this technique. The use of the spray-coated ITO layer (Figure 5.19b) resulted in an average efficiency of 1.6±0.2% and a 2.2% efficiency for the champion device, with J_{sc} of 9.4 $\mathrm{mA\ cm^{-2}}$, V_{oc} of 0.34 V, and FF of 67.5%. Cross-sectional SEM imaging shows the stack of all-non-vacuum processed CIGSe PV cell with spray-coated *i*–ZnO and ITO layers with a proper stacking of all layers (Figure 5.20).

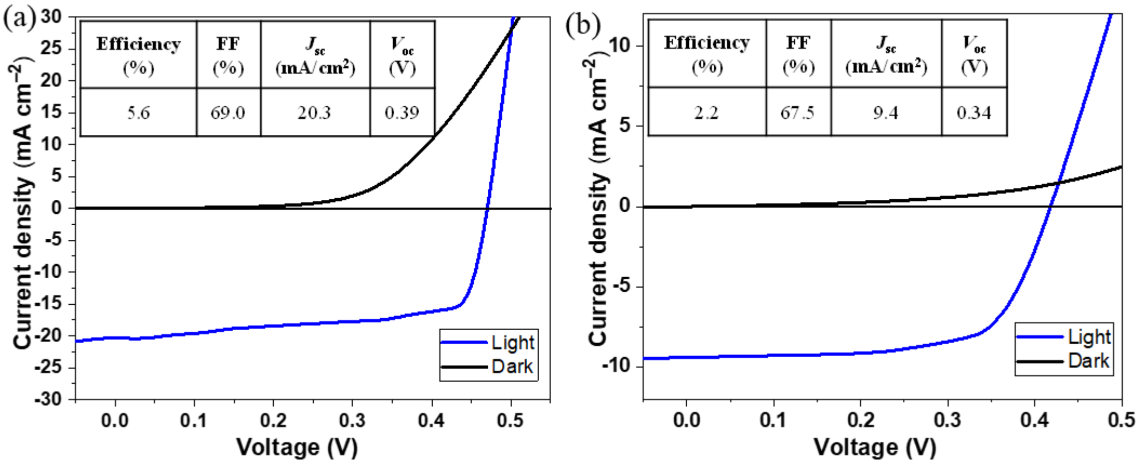

Figure 5.19. The *J–V* curves of champion CIGSe PV cells developed with sputtered ITO (a), and spray-coated ITO (b).

Table 5.2. Photovoltaic parameters of the PV cells fabricated by screen printing of photoabsorber layer, spray-coated *i*–ZnO, and sputtered ITO layer.

PV cell	Efficiency (%)	FF (%)	J_{SC} (mA cm^{-2})	V_{OC} (V)
1	5.6	69.0	20.3	0.39
2	4.2	62.3	17.5	0.38
3	5.3	56.7	24.5	0.37
4	5.5	57.2	23.9	0.39
5	4.1	61.9	16.7	0.39
6	4.5	54.6	20.6	0.39
7	4.3	52.3	20.4	0.39
8	4.5	56.5	20.3	0.38
9	4.3	50.9	20.6	0.40
10	4.5	55.0	20.0	0.39
Average	4.7	57.6	20.5	0.39
Standard Deviation	0.6	5.4	2.4	0.01

Table 5.3. Photovoltaic parameters of PV cells fabricated by screen printing of photoabsorber layer, and spray-coated *i*–ZnO and ITO layers.

PV cell	**Efficiency (%)**	**FF (%)**	J_{SC} (mA cm^{-2})	V_{OC} **(V)**
1	1.6	71.9	6.6	0.34
2	1.5	78.1	5.2	0.36
3	1.4	76.8	5.2	0.33
4	1.4	77.8	5.0	0.36
5	1.6	79.9	5.3	0.36
6	1.7	70.6	7.2	0.32
7	1.5	72.5	6.6	0.31
8	1.7	71.4	7.4	0.31
9	1.8	73.8	7.6	0.32
10	2.2	67.5	9.4	0.34
Average	1.6	74.0	6.6	0.34
Standard Deviation	0.2	4.0	1.4	0.02

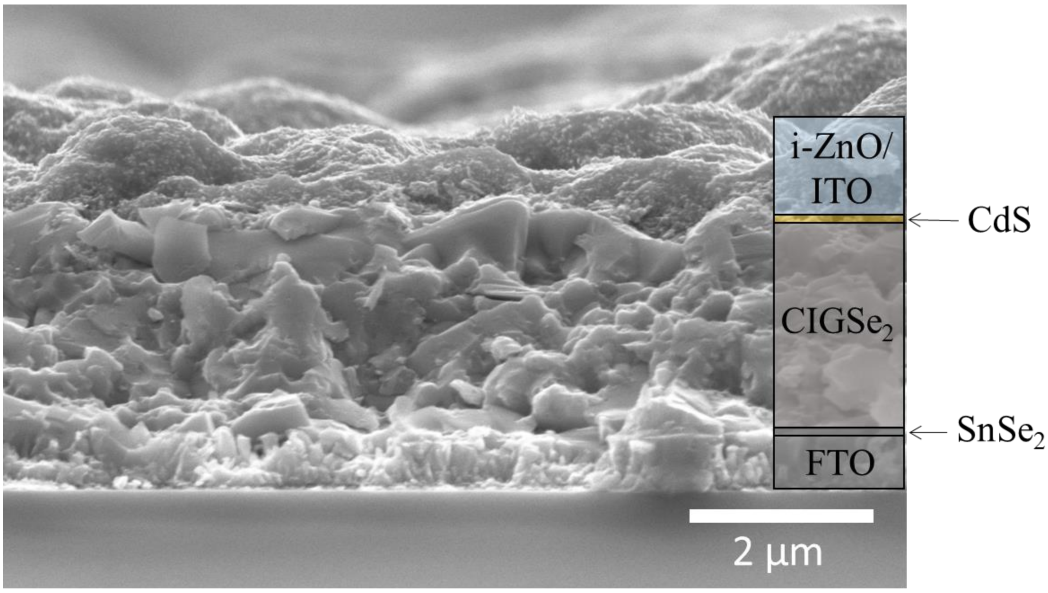

Figure 5.20. Cross-sectional SEM imaging of the all-non-vacuum processed CIGSe PV cell.

Sputtering of ITO gives rise to films with higher conductivity than those obtained by non-vacuum deposition processes [33, 34]. Thus, a lower series resistance is expected for the sputtered ITO layer than the spray-coated one, which is reflected in the resultant *J–V* curves. On the other hand, the device with sputtered ITO layer revealed a lower shunt resistance due to manufacturing defects, which mainly resulted in a lower average FF obtained for the ten PV cells measured: 57.6% and 74.0% for sputtering and spray-coated ITO, respectively. The excellent optical and electrical characteristics of the sputtered ITO layer gave rise to a higher transmittance of photons that can be absorbed by the CIGSe layer and higher extraction of charge carriers by the top conductive layer itself, explaining the higher J_{sc} of 20.3 $\mathrm{mA\ cm^{-2}}$ when compared to 9.4 $\mathrm{mA\ cm^{-2}}$ obtained using spray-coated ITO. Previous studies have revealed that due to differences in ITO crystallinity, higher bandgaps are obtained when using sputtering as compared to non-vacuum processes [35]. Moreover, controlling In doping is difficult with non-vacuum deposition, contributing to slightly different V_{oc} values of 0.39 V, and 0.34 V from sputtering and spray coating, respectively.

5.4 Discussion

5.4.1 Photoabsorber oxide inks

It was found that the primary challenge to obtain an eco-friendly ink for screen printing is the achievement of a uniform dispersion of raw oxide materials in the solvent and additive mixture. Experimental efforts showed that the functionalization of the oxides by Tiron surfactant produces well-dispersed ink mixtures, as has been reported in the literature for several oxide materials in aqueous medium (e.g., CuO [17], $\mathrm{Al_2O_3}$ [36], $\mathrm{TiO_2}$ [37], $\mathrm{ZrO_2}$ [37], $\mathrm{Fe_2O_3}$ [38]). Tiron complexes with the metal sites on the oxide surface, thus capping the material. The hydroxyl and sulfonate groups of the compound result in negatively charged particles with high repulsion, thus improving the dispersion of the particles in water.

Having well-dispersible oxides in hands, two novel PVA- and HPMC-based inks were successfully formulated. Notably, this is the first time that eco-friendly and affordable inks, free of expensive and toxic components, are established for the fabrication of the CIGSe photoabsorber layer. The experimentally optimized first ink consists of oxides (23%), Tiron (0.5%), BYK28 defoamer (0.5%), PVA thickener (19%), and water. Screen printing of this ink with moderate calcination of the resultant oxide film to remove organic matter, and subsequent selenization to convert the oxides into quaternary metal selenide, render phase-pure $\mathrm{Cu_{0.9}(In_{0.74}Ga_{0.25})Se_2}$ thin films with compact morphology and uniform thickness of ≈3.5 μm. The second ink is composed of Tiron-functionalized oxides (30%), HPMC thickener (3.6%), and water/ethanol (1:2). Based on the low degradation temperature and high viscosity of HPMC, the calcination step required for the PVA oxide ink could be omitted. Accordingly, screen printing of the ink followed by selenization provided highly compact and phase-pure $\mathrm{Cu_{0.92}(In_{0.77}Ga_{0.31})Se_2}$

photoabsorber layer with uniform thickness of ≈2.5 µm. The differences in the chemical composition of the films obtained with both PVA and HPMC oxide inks, mainly in the Ga composition, may arise from the inferior dispersion of the oxides in the PVA ink as compared to HPMC, leading to the presence of GaO that has not been entirely converted into CIGSe and therefore a lower amount of Ga in the final CIGSe crystals.

Non-vacuum fabrication of CIGSe photoabsorber thin films from mixed oxide precursors has been previously reported [10]. Typically, a coating containing well-mixed CuO, In_2O_3, and Ga_2O_3 is applied on Mo-coated SLG to form a thin film. After drying, the film is reduced under H_2 atmosphere to obtain a smooth Cu–In–Ga alloy coating. Finally, the resultant thin film is subjected to a selenization procedure, thus affording the desired CIGSe photoabsorber layer as a result of the chemical reaction between Se or H_2Se, supplied by the gas phase, and the Cu–In–Ga alloy. For a low-cost, fast and less energy-demanding fabrication of CIGSe PVs, it would be beneficial to reduce the number of the processing steps. To achieve this, the present study successfully combines the oxide reduction with selenization, thereby eliminating one processing step.

A notable experimental observation is that the selenization has to be conducted in the presence of a reductive 5%H_2/Ar atmosphere in order to entirely convert the commercial oxides into the desired CIGSe phase, following the next chemical reaction (Equation 5.5).

$$2CuO_{(s)} + In_2O_{3(s)} + Ga_2O_{3(s)} + 4H_2Se_{(g)} + 4H_2 = 2Cu(In,Ga)Se_{2(s)} + 8H_2O_{(g)} \quad (5.5)$$

A systematic comparison of the results obtained for the different conductive back contact substrates (viz. Mo-coated SLG, graphite, graphene-coated graphite, stainless steel, carbon-coated stainless steel, FTO/SLG) allows to identify that, in nearly all aspects, only FTO/SLG remains stable during the harsh selenization treatment. Although the formation of a very small $SnSe_2$ admixture was observed, the conductivity of the FTO was found to be largely preserved. In contrast, the metal back contacts (Mo, Fe) were observed to suffer from severe formation of selenide phases ($MoSe_2$, Fe_3Se_4) during the selenization in 5%H_2/Ar. In the case of Mo, its entire conversion into $MoSe_2$ leads to peeling of the film, while Fe diffusion into the CIGSe layer poisons the semiconducting characteristics of the phase, turning it into a conductive one. A similar situation was found in the case of carbon-based back contacts, which were found to be unsuitable for the screen printing fabrication of the CIGSe photoabsorber layer, mainly due to the detrimental morphological issues associated with the delamination and cracking of the resultant films. Accordingly, the use of chemically resistant and thermally stable back contact substrates (e.g., FTO/SLG) is essential when fabricating CIGSe from oxides via direct selenization under reductive $\mathrm{H_2}$ atmosphere [22].

As stated earlier, the printing method is an interesting process to access CIGSe PVs, with the exclusion of energy-demanding vacuum deposition, thus lowering the cost and environmental impact of the solar cell fabrication. Consequently, the PV-relevant band gap energies were studied for the obtained CIGSe photoabsorber thin films. The obtained band gap values were estimated to be 0.97 and 1.08 eV for the CIGSe layers screen-printed from PVA and HPMC oxide inks, respectively. These results highlight the potential of thin films for PV device fabrication, indicating that the presented screen printing approach provides a sustainable alternative to vacuum-based fabrication methods. Although the observed band gap energies are slightly lower than the suggested optimal band gap of 1.14 eV, they are comparable to those reported for CIGSe with similar metal ratios [39, 40]. The variation in chemical composition and possible internal strain effects could be the reasons for the observed red-shift in the absorption spectra for the resultant CIGSe thin films [40].

5.4.2 Photovoltaic devices

To date, few PV cells have been fabricated using screen printing despite its great promise for the deposition of large-dimension layers with low cost, good uniformity, and high resolution, characteristics that are very attractive for industrial production. Furthermore, this technique allows to print layers with few micrometers of thickness on any kind of substrate, from flexible polymers to rigid glasses.

Herein, the combination of screen-printed water-based CIGSe photoabsorber with chemical-bath-deposited *n*-type CdS and sputtered *i*–ZnO/AZO layers led to a reliable CIGSe PV cell with an average efficiency of ≈4.6±1.2% and a maximum efficiency of 7.9% with J_{sc} of 39.5 $\mathrm{mA\ cm^{-2}}$, V_{oc} of 0.33 V, and FF of 57.8%. However, the detected voids in the interface between the back contact and the photoabsorber negatively impacted the performance of the device and need to be addressed in the future by introducing a passivation layer above the FTO back contact or by softening the selenization conditions. Nevertheless, this device sets the record efficiency for CIGSe PV cells with screen-printed photoabsorbers.

Recently, in addition to coating/printing of the CIGSe photoabsorber layer, there has been increasing interest in non-vacuum processed upper layers to give access to all-non-vacuum processed CIGSe PVs [13, 14]. This pathway would result in CIGSe PVs with lower costs and allow for high throughput production.

The CBD of the CdS layer is a very well-established non-vacuum-based process used in most CIGSe PV cells. On the other hand, the TCOs used on top conductive layers are under extensive investigation due to their utility in devices of different natures, such as displays and smart windows [41]. The upper layers of vacuum processed CIGSe PVs have been replaced by spray and spin-coated carbon allotropes [42], AgNW [43], ITO NPs [44], PEDOT:PSS [45], and AZO [30], all in combination with *i*–ZnO or similar semiconductors. Herein, the sputtering of *i*–ZnO/AZO layers has been replaced by spray-coated *i*–ZnO/ITO layers, resulting in a device with 7.9% of efficiency. In line with a sustainable approach, both inks were developed using ethanol and water as solvents. A single layer of spray-coated *i*–ZnO ink with 100 nm of thickness was used for all PVs. On top of it, the effect of the ITO layer on the PV performance was studied by comparing the spray-coated ITO layer with a sputtered one. The CIGSe PV cell with the sputtered layer was found to outperform the spray-coated one with 5.6% of efficiency as compared to 2.2%.

The few existing studies on all-non-vacuum processed CIGSe PVs comprising printed CIGSe photoabsorber have reported efficiencies of 7.7% [14] and 1.6% [13]. The former was produced by Nagino et al. by spin coating the FTO back contact on glass substrate [14]. A CIGSe precursor layer was then spin-coated and selenized, albeit without specifying the nature of the precursors or the ink formulation. To finalize the cell, CBD of CdS and spin coating of *i*–ZnO/AgNW layers was performed. The lower efficiency CIGSe PV cell was produced by spin coating all the layers [13]. First, CIGSe precursor ink comprising synthesized CIGSe NPs suspended in *o*-dichlorobenzene was deposited on commercial MO/SLG followed by calcination to remove organic matter, without the need of a selenization step. Then, CdS, ZnO, AgNW, and ZnO layers were spin-coated consecutively followed by a final annealing at 200 °C. The ZnO precursor solution was developed using 2-methoxyethanol and monoethanolamine solvents.

Herein, an all-non-vacuum processed CIGSe PV cell was fabricated resulting in a maximum efficiency of 2.2%, J_{sc} of 9.4 $\mathrm{mA\ cm^{-2}}$, V_{oc} of 0.34 V, and FF of 67.5%. With a screen-printed water-based CIGSe layer and subsequent selenization above commercial FTO/SLG substrate, followed by CBD of the CdS layer and spray coating of water-based *i*–ZnO and ITO inks, it has been achieved an environmentally friendly all-non-vacuum processed CIGSe PV cell with the highest efficiency reported.

5.5 Conclusion

Two novel environmentally friendly screen printable inks have been successfully designed, formulated, and optimized to access phase-pure and compact $\mathrm{Cu(In,Ga)Se_2}$ photoabsorber layers with few μm of thickness exhibiting required semiconducting properties. Of particular interest is that by using readily available starting oxide materials as metal source, it has been possible to access the $\mathrm{Cu(In,Ga)Se_2}$ phase through the direct selenization under reductive hydrogen atmosphere, without the use of the commonly reported oxide reduction step. Moreover, the films printed with the HPMC ink allowed the omission of a calcination step, requiring just a short selenization procedure. At the same time, the selenization approach was found to place some constraints on the selection of the conductive substrates, and fluorine-doped tin oxide coated glass has been established to be a suitable candidate.

The selection of HPMC oxide ink with following selenization as the photoabsorber layer, chemical bath deposition of CdS buffer and sputtering of top conductive layers to produce a CIGSe PV cell resulted in a 7.9% of efficiency record-breaking device with the following stack SLG/FTO/CIGSe/CdS/*i*–ZnO/AZO.

To further minimize the environmental impact of the PV cell production, the upper layers have been deposited by spray coating of water/ethanol-formulated *i*–ZnO and ITO inks. The resulting CIGSe PV cell featured 2.2% of efficiency, the highest reported using an environmentally friendly all-non-vacuum processed approach. This work encourages the use of a combination of printing/coating technologies with sustainable inks to lower the production costs, allowing for high throughput, and in general to give access to more sustainable CIGSe PV cells.

5.6 References

1. Zhang, T., et al., *High efficiency solution-processed thin-film $Cu(In,Ga)(Se,S)_2$ solar cells.* Energy & Environmental Science, 2016. **9**(12): p. 3674-3681.
2. Todorov, T.K., et al., *Solution-processed $Cu(In,Ga)(S,Se)_2$ absorber yielding a 15.2% efficient solar cell.* Progress in Photovoltaics: Research and Applications, 2013. **21**(1): p. 82-87.
3. McLeod, S.M., et al., *Synthesis and characterization of 15% efficient CIGSSe solar cells from nanoparticle inks.* Progress in Photovoltaics: Research and Applications, 2015. **23**(11): p. 1550-1556.
4. Berner, U., et al., *13.3% efficient solution deposited $Cu(In,Ga)Se_2$ solar cells processed with different sodium salt sources.* Progress in Photovoltaics: Research and Applications, 2016. **24**(6): p. 749-759.
5. Lin, X., et al., *11.3% efficiency $Cu(In,Ga)(S,Se)_2$ thin film solar cells via drop-on-demand inkjet printing.* Energy & Environmental Science, 2016. **9**(6): p. 2037-2043.
6. Wang, W., Y.-W. Su, and C.-h. Chang, *Inkjet printed chalcopyrite $CuIn_xGa_{1-x}Se_2$ thin film solar cells.* Solar Energy Materials and Solar Cells, 2011. **95**(9): p. 2616-2620.
7. Septina, W., et al., *$Cu(In,Ga)(S,Se)_2$ Thin Film Solar Cell with 10.7% Conversion Efficiency Obtained by Selenization of the Na-Doped Spray-Pyrolyzed Sulfide Precursor Film.* ACS Applied Materials & Interfaces, 2015. **7**(12): p. 6472-6479.
8. Arnou, P., et al., *Solution processing of $CuIn(S,Se)_2$ and $Cu(In,Ga)(S,Se)_2$ thin film solar cells using metal chalcogenide precursors.* Thin Solid Films, 2017. **633**: p. 76-80.

9. Pulgarín-Agudelo, F.A., et al., *A thermal route to synthesize photovoltaic grade CuInSe$_2$ films from printed CuO/In$_2$O$_3$ nanoparticle-based inks under Se atmosphere.* Journal of Renewable and Sustainable Energy, 2013. **5**(5): p. 053140.
10. Kapur, V.K., et al., *Non-vacuum processing of CuIn$_{1-x}$Ga$_x$Se$_2$ solar cells on rigid and flexible substrates using nanoparticle precursor inks.* Thin Solid Films, 2003. **431-432**: p. 53-57.
11. Londhe, P.U., A.B. Rohom, and N.B. Chaure, *Solar cell studies on CuIn$_{1-x}$Ga$_x$Se$_2$ nanoparticles derived from chemical reduction process.* Solar Energy, 2020. **206**: p. 18-26.
12. Lu, C.-H., et al., *Solution-processed Cu(In,Ga)(Se,S)$_2$ solar cells prepared via a surface sulfurization process.* Journal of the Taiwan Institute of Chemical Engineers, 2020. **110**: p. 41-50.
13. Singh, M., et al., *Thin-Film Copper Indium Gallium Selenide Solar Cell Based on Low-Temperature All-Printing Process.* ACS Applied Materials & Interfaces, 2014. **6**(18): p. 16297-16303.
14. Nagino, S., H. Suzuki, and S. Ueno. *Substrate-type Cu(In,Ga)Se$_2$ solar cells with all layers deposited by non-vacuum solution-based methods*. in *2013 IEEE 39th Photovoltaic Specialists Conference*. 2013. Tampa, FL, USA.
15. Kemell, M., M. Ritala, and M. Leskelä, *Thin Film Deposition Methods for CuInSe$_2$ Solar Cells.* Critical Reviews in Solid State and Materials Sciences, 2005. **30**(1): p. 1-31.
16. Baskaran, D., K. Chinnappan, and R. Manivasagam, *Chemical Synthesis of Zinc Oxide Nanoparticles and Its Application of Dye Decolourization.* International Journal of Nanoscience and Nanotechnology, 2018. **14**: p. 267-275.
17. Guedes, M., J.M.F. Ferreira, and A.C. Ferro, *Dispersion of Cu$_2$O particles in aqueous suspensions containing 4,5-dihydroxy-1,3-benzenedisulfonic acid disodium salt.* Ceramics International, 2009. **35**(5): p. 1939-1945.
18. Zhao, D., et al., *Solution-deposited pure selenide CIGSe solar cells from elemental Cu, In, Ga, and Se.* Journal of Materials Chemistry A, 2015. **3**(38): p. 19263-19267.
19. Shi, Y., et al., *In situ repair of graphene defects and enhancement of its reinforcement effect in polyvinyl alcohol hydrogels.* RSC Advances, 2017. **7**(2): p. 1045-1055.
20. Witte, W., R. Kniese, and M. Powalla, *Raman investigations of Cu(In,Ga)Se$_2$ thin films with various copper contents.* Thin Solid Films, 2008. **517**(2): p. 867-869.
21. Rincón, C. and F.J. Ramírez, *Lattice vibrations of CuInSe$_2$ and CuGaSe$_2$ by Raman microspectrometry.* Journal of Applied Physics, 1992. **72**(9): p. 4321-4324.
22. Kessler, F. and D. Rudmann, *Technological aspects of flexible CIGS solar cells and modules.* Solar Energy, 2004. **77**(6): p. 685-695.
23. Yan, Y., et al., *Cu(In,Ga)Se$_2$ thin films annealed with SnSe$_2$ for solar cell absorber fabricated by magnetron sputtering.* Solar Energy, 2017. **155**: p. 601-607.
24. Morales-Acevedo, A., *A simple model of graded band-gap CuInGaSe$_2$ solar cells.* Energy Procedia, 2010. **2**(1): p. 169-176.
25. Ramanujam, J. and U.P. Singh, *Copper indium gallium selenide based solar cells – a review.* Energy & Environmental Science, 2017. **10**(6): p. 1306-1319.
26. Huang, C.-H., et al., *Deposition Technologies of High-Efficiency CIGS Solar Cells: Development of Two-Step and Co-Evaporation Processes.* Crystals, 2018. **8**(7): p. 296.
27. Kamada, R., W.N. Shafarman, and R.W. Birkmire, *Cu(In,Ga)Se$_2$ film formation from selenization of mixed metal/metal–selenide precursors.* Solar Energy Materials and Solar Cells, 2010. **94**(3): p. 451-456.
28. Kim, B. and B.K. Min, *Strategies toward highly efficient CIGSe thin-film solar cells fabricated by sequential process.* Sustainable Energy & Fuels, 2018. **2**(8): p. 1671-1685.
29. Lee, E., et al., *Nearly carbon-free printable CIGS thin films for solar cell applications.* Solar Energy Materials and Solar Cells, 2011. **95**(10): p. 2928-2932.

30. Wang, M. and K.-L. Choy, *All-Nonvacuum-Processed CIGS Solar Cells Using Scalable Ag NWs/AZO-Based Transparent Electrodes.* ACS Applied Materials & Interfaces, 2016. **8**(26): p. 16640-16648.
31. Serkov, A.A., et al., *Laser sintering of gravure printed indium tin oxide films on polyethylene terephthalate for flexible electronics.* Scientific Reports, 2019. **9**(1): p. 1773.
32. Kang, S., et al., *Characteristics of an oxide/metal/oxide transparent conducting electrode fabricated with an intermediate Cu–Mo metal composite layer for application in efficient CIGS solar cell.* RSC Advances, 2017. **7**(76): p. 48113-48119.
33. Kurdesau, F., et al., *Comparative study of ITO layers deposited by DC and RF magnetron sputtering at room temperature.* Journal of Non-Crystalline Solids, 2006. **352**(9): p. 1466-1470.
34. Alsaid, D.A., et al., *Gravure Printing of ITO Transparent Electrodes for Applications in Flexible Electronics.* Journal of Display Technology, 2012. **8**(7): p. 391-396.
35. Jeong, J.-A., et al., *Ink-jet printed transparent electrode using nano-size indium tin oxide particles for organic photovoltaics.* Solar Energy Materials and Solar Cells, 2010. **94**(10): p. 1840-1844.
36. Tarì, G., J.M.F. Ferreira, and O. Lyckfeldt, *Influence of the stabilising mechanism and solid loading on slip casting of alumina.* Journal of the European Ceramic Society, 1998. **18**(5): p. 479-486.
37. Pagnoux, C., *Suspension systems for coagulation processing.* Journal of Ceramic Processing Research, 2002. **3**: p. 10-14.
38. Korpany, K.V., et al., *Stable water-soluble iron oxide nanoparticles using Tiron.* Materials Chemistry and Physics, 2013. **138**(1): p. 29-37.
39. Roux, F., et al., *Chalcopyrite thin-film solar cells by industry-compatible ink-based process.* Solar Energy Materials and Solar Cells, 2013. **115**: p. 86-92.
40. Yang, J., et al., *Effects of hydrogen peroxide on electrodeposition of Cu(In,Ga)Se$_2$ thin films and band gap controlling.* Electrochimica Acta, 2014. **142**: p. 208-214.
41. Brunin, G., et al., *Transparent conducting materials discovery using high-throughput computing.* npj Computational Materials, 2019. **5**(1): p. 63.
42. Contreras, M.A., et al., *Replacement of Transparent Conductive Oxides by Single-Wall Carbon Nanotubes in Cu(In,Ga)Se$_2$-Based Solar Cells.* The Journal of Physical Chemistry C, 2007. **111**(38): p. 14045-14048.
43. Kim, A., et al., *All-Solution-Processed Indium-Free Transparent Composite Electrodes based on Ag Nanowire and Metal Oxide for Thin-Film Solar Cells.* Advanced Functional Materials, 2014. **24**(17): p. 2462-2471.
44. Xiao-Hui Tan, Y.C., and Ye-Xiang Liu, *Silver nanowire composite thin films as transparent electrodes for Cu(In,Ga)Se$_2$/ZnS thin film solar cells.* Applied Optics, 2014. **53**(15): p. 3273-3277.
45. Shin, D., et al., *Solution-Processed Ag Nanowires + PEDOT:PSS Hybrid Electrode for Cu(In,Ga)Se$_2$ Thin-Film Solar Cells.* ACS Applied Materials & Interfaces, 2015. **7**(24): p. 13557-13563.

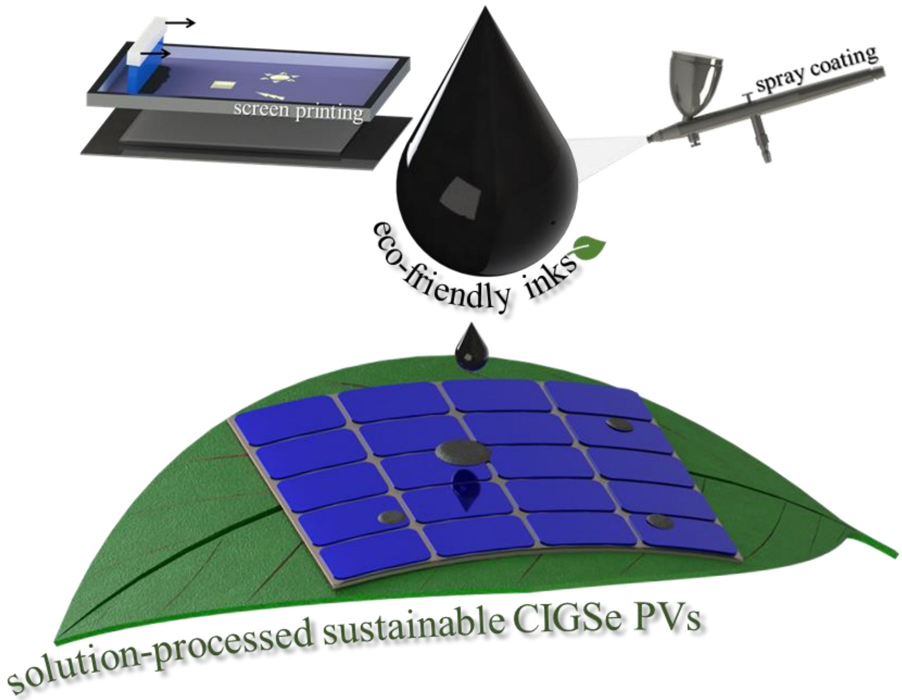

Chapter 6. Conclusions and future work

This chapter presents the main conclusions of this work which was mainly devoted to the development of solution-processed CIGSe PVs using conventional and more sustainable methodologies. Moreover, suggestions for future work are also provided.

6.1 Conclusions

The PV market has been growing and providing solutions beyond the stablished silicon technology. Second generation thin film PV cells have been attracting increasing attention and important advances have been achieved in CIGSe, which recently reached 23.4% of efficiency. In industry, this type of PV cells are currently fabricated by vacuum-based deposition processes. Despite affording high-performing CIGSe PV modules, the processes used in vacuum-based fabrication are complex, expensive, energy demanding and with relevant environmental impact.

The high demand for sustainable and environmentally benign fabrication methods of CIGSe PVs has prompted an active search for low-cost alternatives to vacuum-deposition processes. To address this need, this work was focused on printed/solution-processed CIGSe PVs. To this end, phase-pure CIGSe NPs were synthesized and photoabsorber thin films with high crystallinity and excellent optical properties were screen-printed to be further used on the fabrication of PV devices. Moreover, environmentally friendly alternative methodologies were addressed, and as a result, an environmental friendlier PV cell with screen-printed photoabsorber was developed. Furthermore, by addressing the top conductive layers' deposition by spray coating of environmentally friendly inks, a sustainable all-solution processed CIGSe PV cell was produced.

6.1.1 Conventional methodologies for solution-processed CIGSe photovoltaic systems

Starting with the conventional methodologies, a large-scale heat-up synthesis was developed, delivering phase-pure CIGSe NPs with hexagonal wurtzite structure. Importantly, wurtzite-type CIGSe is a very uncommon structure, difficult to obtain. This synthesis delivered NPs with a chemical composition of $\mathrm{Cu_{0.89}(In_{0.72}Ga_{0.28})Se_2}$ which is the ratio used in high efficiency devices, and with Ga not only distributed inside the NPs but also at their surface, due to a self-exclusion behavior of the NPs. Moreover, the synthesized NPs were embedded into an ink formulation for screen printing deposition on SLG, delivering a photoabsorber layer with ~4.5 µm of homogeneous thickness, after annealing, and a crystal structure change from wurtzite to chalcopyrite.

Besides the use of synthesized CIGSe NPs for photoabsorber layer deposition, commercial oxides precursors were used as well. To this end, Cu, In and Ga oxides were well-dispersed in a high viscosity ink based on terpineol solvent for screen printing deposition over FTO/SLG substrate followed by calcination and selenization. A photoabsorber layer was obtained characterized by high crystallinity and phase-pure CIGSe with tetragonal chalcopyrite structure and an homogenous thickness of ~2 µm.

Notably, by depositing the upper layers CdS by CBD and top conductive *i*–ZnO/AZO by sputtering, a reliable CIGSe PV with 6.1% of efficiency cell was fabricated.

6.1.2 Sustainable methodologies for solution-processed CIGSe photovoltaic systems

In order to develop more sustainable methodologies, a large-scale aqueous synthesis of CIGSe NPs was developed. Importantly, due to the oxidative nature of water, phase-pure CIGSe NPs are difficult to address. To this end, the use of a nature-derived stabilizer (GSH) for Cu complexation, afforded the synthesis of ≈5 g of NPs which with further annealing treatment delivered phase-pure CIGSe NPs with tetragonal chalcopyrite structure. Moreover, the NPs presented a nominal metals ratio of $\mathrm{Cu_{0.79}(In_{0.74}Ga_{0.33})Se_2}$ and an ideal optical band gap of 1.14 eV.

Furthermore, the use of sustainable methodologies for the development of CIGSe photoabsorber layers from commercial oxides was also achieved. Accordingly, two novel water-based inks with well-dispersed oxides were formulated and screen-printed over several conductive substrates. A photoabsorber layer was thus obtained with phase-pure CIGSe with tetragonal chalcopyrite structure by avoiding the commonly used calcination and oxide reduction steps. Notably, a fast selenization treatment was enough to deliver a photoabsorber layer with nominal ratio of $\mathrm{Cu_{0.92}(In_{0.77}Ga_{0.31})Se_2}$ and homogeneous thickness of ≈2.5 μm. The fabrication of a CIGSe PV device with the screen-printed photoabsorber, CBD of CdS and sputtering of *i*–ZnO/AZO delivered a robust record-breaking CIGSe PV cell with 7.9% of efficiency.

Finally, the top conductive layers vacuum-deposition were replaced by spray coating of water-based inks for *i*–ZnO/ITO layers, allowing the fabrication of a reliable and novel sustainable all-non-vacuum processed CIGSe PV cell with 2.2% of efficiency.

Looking forward, the continuous search for efficient “green” and printable CIGSe, as for all-printed/solution processed PVs, is essential and will lead these PVs to a more competitive path, as they present advantages in terms of price, miniaturization, flexibility, weight, and especially with respect to expanded fields of application, such as windows and textiles.

6.2 Future work

The presented work represents a contribution to the development of solution-processed CIGSe PVs, providing also environmentally friendly approaches to replace inconvenient procedures usually required for this technology. Moreover, it was demonstrated that environmentally friendly alternatives do not always mean lower performance. However, there are still needs for improvement with respect to the inks and fabrication methodologies used for CIGSe PVs.

- Improve the synthesized CIGSe wurtzite NPs dispersion on the ink formulation in order to deliver a thin film with lower thickness to further fabricate PV devices. Moreover, the ink could be optimized to avoid the use of an annealing treatment at high temperatures so that wurtzite phase could be preserved and therefore its effects on the PV cell performance could be evaluated and compared with chalcopyrite one.
- Formulate inks with the aqueously synthesized CIGSe chalcopyrite NPs to further fabricate CIGSe PV cells.
- Deposit the HPMC water-based oxide inks into an FTO/SLG substrate with a passivation layer so that the photoabsorber-back contact interface problems could be solved, and the PV cell efficiency optimized.
- Improve the spray coating deposition of *i*–ZnO/ITO top conductive layers so that a higher amount of photons can be absorbed by the CIGSe layer and therefore a higher efficiency device could be achieved.
- Replace the CdS layer by another non-toxic compound to increase the sustainability of the PV cell fabrication.
- Implement the methodologies used in the all-non-vacuum processed CIGSe PV cell in roll-to-roll industrial production.
- Perform a life-cycle assessment of the CIGSe PV cells to evaluate performance and impact in the scope of the circular economy and green deal paradigms.